DAMAGE AND MICROSTRUCTURAL CHANGE IN LABORATORY GROWN ICE UNDER HIGH PRESSURE ZONE CONDITIONS

PAUL M. MELANSON

Damage and Microstructural Change in Laboratory Grown Ice Under High Pressure Zone Conditions

by:

© Paul M. Melanson
C.A.S. (Acadia), B.Eng. (TUNS)

A thesis submitted to the School of Graduate Studies
in partial fulfilment of the requirements for
the degree of Master of Engineering

Faculty of Engineering and Applied Science
Memorial University of Newfoundland
April, 1998

St. John's Newfoundland Canada

And now there came both mist and snow,
And it grew wondrous cold:
And ice, mast-high, came floating by,
As green as emerald.

And through the drifts the snowy clifts
Did send a dismal sheen:
Nor shapes of men nor beasts we ken--
The ice was all between.

The ice was here, the ice was there,
The ice was all around:
It cracked and growled,
and roared and howled,
Like noises in a swound!

The Rime of the Ancient Mariner
by Samuel Taylor Coleridge (1772-1834)

Originally in:
The Poetical Works of S.T. Coleridge
(London : W. Pickering, 1834).

Abstract

Ice-structure interactions, where crushing is the predominant mode of failure, are characterised by zones of intense high pressure within the ice feature. This work investigates the mechanical and microstructural behaviour within these zones by using triaxial testing on laboratory grown freshwater granular ice. The latest interpretation of the behaviour of ice in high pressure zones during ice-structure interactions is presented, based on previous work at Memorial University of Newfoundland. A review of triaxial testing on ice is also presented.

Results of triaxial testing on ice indicate the existence of two separate but overlapping deformation mechanism regimes at high and low confining pressures. High microcrack densities followed by a reduction in grain size by recrystallisation and restructuring were observed in low hydrostatic pressure tests ($p < 30$ MPa). At higher pressures ($p > 40$ MPa) this was replaced by more intense recrystallisation and possible pressure melting at grain boundaries and triple points.

Triaxial tests were used in the calibration of a pressure-dependent constitutive model for granular ice. The constitutive model is based on continuum damage mechanics and uses the reduction of the standard Burgers body to a single non-linear dashpot to model the response of ice under high stress and high strain conditions. Results show moderate agreement with test data collected from ice damaged triaxially at constant deformation rate and loaded axially at high confining pressures,. More work is needed to improve the calibration of the model further over a wider range of confining pressures.

Acknowledgements and Dedication

At this point I would like to thank my supervisor, Dr. Ian Jordaan, for all his support and guidance during the course of my studies at Memorial University. I would also like to acknowledge the Faculty of Engineering and Applied Science and the School of Graduate Studies for the many ways in which the they have helped me in completing this work. Thanks are also directed to the National Research Council's Institute for Marine Dynamics, in particular Dr. Robert Gagnon and Dr. Stephen Jones, for support in the generous use of their cold room facilities. I would also like to thank Irene Meglis, who acted as my unofficial supervisor on many occasions, for the countless hours that were put into performing the tests with me and the many discussions surrounding the results. Other people to whom I would like to express thanks include Barry Stone who offered much sound advice regarding the operation of the laboratory, Peter Finlay for his work with the testing and preparation of ice, as well as the laboratory technicians who kept the testing equipment in fine form.

Finally, I would like to dedicate this work to the memory of my grandfather, J. Stanislaus Saulnier, who passed away on September 13th, 1996, while I was studying at Memorial. I will miss him very much. I would also like to dedicate this work to my parents, Bernard and Diane, and the rest of my family and thank them for their support, not only during my studies at Memorial but throughout all of my university education. And finally, to Jane Sodero, thank you for all your help and inspiration.

Paul M. Melanson
January 4th, 1998

Table of Contents

Abstract iii
Acknowledgements and Dedication iv
Table of Contents v
List of Figures viii
List of Tables xii
Nomenclature xiii

Introduction and Focus 1
1.1 Introduction 1
1.2 Focus 3

The Behaviour of Ice 5
2.1 Ice as a Material 5
2.1.1 The Microstructure of Ice 5
2.1.2 The Natural Formation of Ice 7
2.2 The Mechanics of an Ice-Structure Interaction and High Pressure Zones 8
2.3 The Small Scale Behaviour of Ice 13
2.3.1 The Creep of Ice 13
2.3.1.1 Pressure 16
2.3.1.2 Grain size and Orientation 17
2.3.2 Constant Strain Rate Deformation of Ice 17
2.3.2.1 Pressure 20
2.3.2.2 Temperature 21
2.3.2.3 Grain Size 22
2.3.3 Damaged Ice 22
2.3.4 Describing the Creep of Ice 24
2.4 Damage and Constitutive Modelling 30
2.4.1 The Effects of Damage 30
2.4.2 Modelling and Describing Damage: An Introduction to Damage Mechanics 31

Experimental Program and Procedure 36
3.1 Test Matrix 36
3.1.1 Constant Deformation Rate Tests 37
3.1.2 Constant Load (or Creep) Tests 37

3.1.3 Constant Load Tests on Damaged Ice 39
3.2 Sample Preparation 39
3.3 Testing Apparatus and Procedure 41
3.4 Corrections to Collected Data 44
3.5 Post Test Analysis 45

Results of Triaxial Testing 48

4.1 Characterisation of Virgin Ice Samples 48
4.2 Constant Deformation Rate Tests 50
4.2.1 Stress versus Strain Curves and Peak Stress 50
4.2.2 Grain Size, Distribution, and C-axis Orientation 52
4.2.3 Microcracking and Recrystallisation 60
4.3 Review of Constant Load Tests 62
4.3.1 Microcracking and Recrystallisation 63
4.3.2 Grain Size, Distribution, and C-axis Orientation 68
4.3.3 Creep Curves and Mechanical Behaviour 70
4.4 Constant Load Tests on Damaged Ice 75
4.4.1 Stress Curves and Mechanical Behaviour 75
4.4.2 Grain Size, Distribution, and C-axis Orientation 79
4.4.3 Microcracking and Recrystallisation 83
4.5 Testing Summary and Discussion 85

Applications to Modelling 88

5.1 The Pressure-dependent Constitutive Model 88
5.1.1 Derivation of the Pressure-dependent Constitutive Model 92
5.2 Model Calibration 95
5.2.1 Data Analysis 95
5.2.2 Stress and Strain Rate Corrections 97
5.2.3 First Calibration of the Model with Data Corrected for Stress 104
5.2.3.1 Calibrating for the Slope (ϕ) 104
5.2.3.2 Temperature Effects 108
5.2.4 Second Calibration of the Model with Corrected Data 109
5.2.4.1 Recalibrating for the Slope (ϕ) 109
5.2.4.2 Calibrating the Intercept (I) 113
5.3 The Calibrated Model 115
5.4 Results of Modelling 116

Concluding Remarks and Recommendations **122**
6.1 Concluding Remarks 122
6.2 Recommendations 123
References **125**
Appendix A **130**
Appendix B **155**
Appendix C **158**

List of Figures

Figure 2.1 Melting temperature versus pressure for ice Ih from Nordell (1990) and Hobbs (1974) 7

Figure 2.2 Diagram of ice-structure interaction event showing a high pressure zone situation 10

Figure 2.3 Constant stress test strain history showing the three strain components used to describe creep 15

Figure 2.4 Stress versus strain for a typical constant strain rate test showing the peak stress of the material 18

Figure 2.5 Constant stress test strain history showing the three creep regimes 25

Figure 2.6 Burgers body showing individual Kelvin and Maxwell units and their associated springs and dashpots 29

Figure 2.7 Spring and dashpot systems representing canonical forms of viscoelastic models 29

Figure 3.1 Schematic of the vacuum system used in preparing seed ice and distilled water for moulding 40

Figure 3.2 Schematic of MTS test frame, pressure intensifying unit, and computer interface 42

Figure 3.3 Plot of calculated and actual diameters versus reduction in length of ice specimen 45

Figure 4.1 Thin section photographs of virgin granular ice sample viewed between crossed polarising filters, with side lighting, and close up 49

Figure 4.2 Stress-strain curve for tests at a strain rate of 10^{-2} s^{-1}.
a) from 0 to 4% strain 50
b) from 0 to 30% strain 51

Figure 4.3 Stress-strain curve for tests at a strain rate of 10^{-4} s^{-1}.
a) from 0 to 4% strain 52
b) from 0 to 30% strain 53

Figure 4.4 Thin section photographs of samples tested at a strain rate of 10^{-2} s^{-1} viewed between crossed polarising filters and with either side light added or with side light only.
a) thin section photographs of test to 0.4% strain @ 10^{-2} s^{-1}.
b) thin section photographs of test to 1.0% strain @ 10^{-2} s^{-1}.
c) thin section photographs of test to 2.0% strain @ 10^{-2} s^{-1} 54

d) thin section photographs of test to 4.1% strain @ 10^{-2} s^{-1}.
e) thin section photographs of test to 12.8% strain @ 10^{-2} s^{-1}.
f) thin section photographs of test to 28.8% strain @ 10^{-2} s^{-1} 55

Figure 4.5 Thin section photographs of samples tested at a strain rate of 10^{-4} s^{-1} viewed between crossed polarising filters and with either side light added or with side light only.
a) thin section photographs of test to 0.4% strain @ 10^{-4} s^{-1}.
b) thin section photographs of test to 1.0% strain @ 10^{-4} s^{-1}.
c) thin section photographs of test to 2.0% strain @ 10^{-4} s^{-1} 57
d) thin section photographs of test to 4.1% strain @ 10^{-4} s^{-1}.
e) thin section photographs of test to 12.8% strain @ 10^{-4} s^{-1}.
f) thin section photographs of test to 28.8% strain @ 10^{-4} s^{-1} 58

Figure 4.6 Grain size plotted versus total strain for all tests performed at constant deformation rate 59

Figure 4.7 Thin section photographs of samples tested at a constant stress of 15 MPa and 5 MPa confinement viewed between crossed polarising filters and with side lighting (from Meglis and others, 1998).
a) thin section photographs of test to 4% strain.
b) thin section photographs of test to 10% strain.
c) thin section photographs of test to 44% strain 64

Figure 4.8 Thin section photographs of samples tested at a constant stress of 15 MPa and 50 MPa confinement viewed between crossed polarising filters and with side lighting (from Meglis and others, 1998).
a) thin section photographs of test to 4% strain.
b) thin section photographs of test to 10% strain.
c) thin section photographs of test to 44% strain 66

Figure 4.9 Thin section photographs of sample tested at a constant stress of 15 MPa and 30 MPa confinement viewed between crossed polarising filters and with side lighting 67

Figure 4.10 Thin section photographs of sample tested at a constant stress of 15 MPa and 40 MPa confinement viewed between crossed polarising filters and with side lighting 67

Figure 4.11 Grain size plotted versus total strain for all tests performed at constant stress 68

Figure 4.12 Strain plotted versus time and stress versus strain for constant stress tests at s =15 MPa and p_c = 5 MPa 71

Figure 4.13 Strain plotted versus time and uncorrected stress plotted versus strain for creep tests at s =15 MPa and p_c = 50 MPa 72

Figure 4.14 Strain plotted versus time and uncorrected stress plotted versus strain for creep tests at s =15 MPa and all other confining pressures 73

Figure 4.15 Pressure plotted versus strain for each of the three pressure histories used in the constant stress tests of the damaged ice 76

Figure 4.16 Strain plotted versus time for damage step and creep step showing both damage strain rates and undamaged test for p_c = 50 MPa during creep tests.....77

Figure 4.17 Strain plotted versus time for the creep step on damaged ice showing the response of undamaged ice and ice damaged at both 10^{-2} and 10^{-4} s^{-1}, and uncorrected stress plotted versus strain for p_c = 15 MPa during creep tests.....78

Figure 4.18 Strain plotted versus time for the creep step on damaged ice showing the response of undamaged ice and ice damaged at both 10^{-2} and 10^{-4} s^{-1}, and uncorrected stress plotted versus strain for p_c = 30 MPa during creep tests.....79

Figure 4.19 Strain plotted versus time for the creep step on damaged ice showing the response of undamaged ice and ice damaged at both 10^{-2} and 10^{-4} s^{-1}, and uncorrected stress plotted versus strain for p_c = 50 MPa during creep tests.....80

Figure 4.20 Grain size plotted versus total strain for all tests creep performed on damaged ice.....81

Figure 4.21 Thin section photographs of damaged ice samples tested at a constant stress of 15 MPa viewed between crossed polarising filters and with side lighting. The damage deformation rate was 10^{-2} s^{-1}.
a) for p_c = 15 MPa during creep tests.
b) for p_c = 30 MPa during creep tests.
c) for p_c = 50 MPa during creep tests.....82

Figure 4.22 Thin section photographs of damaged ice samples tested at a constant stress of 15 MPa viewed between crossed polarising filters and with side lighting. The damage deformation rate was 10^{-4} s^{-1}.
a) for p_c = 15 MPa during creep tests.
b) for p_c = 30 MPa during creep tests.
c) for p_c = 50 MPa during creep tests.....84

Figure 4.23 Grain size plotted versus total strain for all tests in test matrix.....87

Figure 5.1 The reduction of the Burgers body to a single dashpot.....91

Figure 5.2 Plot of the logarithm of strain rate versus time for constant stress tests performed at p_c = 5 MPa.....95

Figure 5.3 Plot of the logarithm of strain rate versus time for constant stress tests performed at p_c = 50 MPa.....96

Figure 5.4 Plot of the logarithm of strain rate versus time for constant stress tests performed at all other confining pressures.....97

Figure 5.5 Plot of the logarithm of true strain rate versus the logarithm of true stress for all tests.....99

Figure 5.6 Plot of the logarithm of corrected strain rate versus time for constant stress tests performed at p_c = 5 MPa (corrected with r = 4.2).....101

Figure 5.7 Plot of the logarithm of corrected strain rate versus time for constant stress tests performed at p_c = 50 MPa (corrected with r = 4.2) 102

Figure 5.8 Plot of the logarithm of corrected strain rate versus time for constant stress tests performed at all other confining pressures. (corrected with r = 4.2) .103

Figure 5.9 Phi (ϕ) plotted against hydrostatic pressure (p) for uncorrected data (using r = 4.2) 105

Figure 5.10 The two pressure dependent terms of the damage function, $f_1(p)$ and $f_2(p)$, plotted and summed to show the resultant function $f(p)$ 107

Figure 5.11 Phi (ϕ) plotted against hydrostatic pressure (p) with temperature data shown for reference (corrected with r = 4.2) 108

Figure 5.12 Plot of the logarithm of corrected strain rate versus time for constant stress tests performed at p_c = 5 MPa (corrected with damage function and r = 4.2) 110

Figure 5.13 Plot of the logarithm of corrected strain rate versus time for constant stress tests performed at p_c = 50 MPa (corrected with damage function and r = 4.2) 111

Figure 5.14 Plot of the logarithm of corrected strain rate versus time for constant stress tests performed at all other confining pressures (corrected with damage function and r = 4.2) 112

Figure 5.15 Slope (phi, ϕ) plotted versus hydrostatic pressure (p) for data corrected with the damage function and r = 4.2 113

Figure 5.16 Intercept (I) plotted versus hydrostatic pressure (p) for data corrected with the damage function and r = 4.2 114

Figure 5.17 Model compared to actual creep test data at p_c = 5 MPa 117

Figure 5.18 Model compared to actual creep test data at p_c = 30 MPa 118

Figure 5.19 Model compared to actual creep test data at p_c = 50 MPa 119

Figure 5.20 Model results compared to constant load tests on damaged ice with different pressures during the creep step The e represents experimental and the m model predictions, while the number in the labels indicates the damage rate (2 is 10^{-2} s^{-1} and 4 is 10^{-4} s^{-1}) 121

List of Tables

Table 3.1 Constant deformation rate test and damage test matrix. 38
Table 3.2 Constant load (creep) test matrix. 38
Table 3.3 Constant load on damaged ice test matrix 38

Table 4.1 Final grain size of constant deformation rate specimens. 56
Table 4.2 Final grain size of ice specimens tested at constant load. 69
Table 4.3 Final grain size of damaged ice specimens following creep step 80

Table 5.1 Strain rates for at various strains s = 15 MPa based on different relations and experimental results for polycrystalline ice. 89
Table 5.2 Model parameters for the pressure-dependent constitutive model 115

Nomenclature

a_1	damage function constant
a_2	damage function constant
A	area (m^2)
A_0	initial area (m^2)
b	exponent (delayed elastic term of Sinha's equation)
c_1	damage constant (delayed elastic term of Sinha's equation)
d	grain size (m)
d_1	reference grain size (m)
dT_m	change in melting point per unit pressure (°C/MPa)
$D(t)$	creep compliance function
D_0, D_1, D_2	creep compliance function constant
e	axial strain (m/m or %)
$\dot{e}$	axial strain rate (s^{-1})
$\dot{e}_{cs}$	strain rate for constant stress (s^{-1})
$\dot{e}_e$	experimental strain rate (s^{-1})
$\dot{e}_{ij}$	strain rate tensor (s^{-1})
E	elastic modulus (MPa)
$E(t)$	relaxation modulus function
E_0	undamaged elastic modulus (MPa)
E_1, E_i	elastic modulus (material property, MPa)
$f(p), f_1(p), f_2(p)$	pressure dependent damage function
$g(S)$	enhancement factor based on damage
I	intercept of $\ln(\dot{e})$ versus time
k, k'	constants
k_k	Kelvin unit elastic stiffness
k_m	Maxwell unit elastic stiffness
l_0	initial length or gauge length of specimen (m)
l_f	final length of specimen (m)
m	damage function exponent
n	damage function exponent
p	hydrostatic pressure (MPa)
p_1	damage function reference pressure (MPa)
p_2	damage function reference pressure (MPa)

p_c	confining pressure (MPa)
p_{tr}	damage function transition pressure (MPa)
P	load (kN)
q	damage function exponent
r	power law exponent
s	deviatoric or differential stress as noted (MPa)
s_0	reference stress (MPa)
s_c	corrected stress (MPa)
s_{ij}	stress tensor (MPa)
s_u	uncorrected stress (MPa)
S	damage
t	time (s)
T	temperature (°C)
α	constant (delayed elastic term of Sinha's equation)
β	creep enhancement factor
ε	axial strain (m/m)
ε_d	delayed elastic strain (m/m)
ε_e	elastic strain (m/m)
ε_t	total strain (m/m)
ε_v	viscous strain (m/m)
ε_E	engineering strain (m/m)
ε_T	true strain (m/m)
ϕ	slope of $\ln(\dot{e})$ versus time
η	viscosity (MPa•s)
η_k	Kelvin unit viscosity (MPa•s)
η_m	Maxwell unit viscosity (MPa•s)
μ_1, μ_i	viscosity (material property, MPa•s)
σ	axial stress (MPa)
σ_e	equivalent stress (MPa)
σ_{ii}	principle axis stress tensor (MPa)
σ_{ij}	stress tensor (MPa)
σ_o	initial stress, reference stress (MPa)
$\frac{dS}{dt}$	change in damage per unit time (s^{-1})

Chapter 1

Introduction and Focus

1.1 Introduction

Ocean-going vessels and structures navigating the waters of the arctic and sub-arctic are designed to be substantially stronger than vessels and structures for use in other parts of the world. This difference is related to the environment in which these structures operate and the hazards that are associated with it. Ice is a threat to vessels operating in arctic waters and is often present in several forms: as pack ice, large ice floes, or icebergs of varying sizes from very large tabular bergs to bergy bits. In these situations ice loads on these structures become an important factor in the development and design of efficient and economical structures for work, exploration, and research in ice covered waters. Until a few years ago, designers of offshore structures and vessels for ice environments were left to determine ice loads based on both a limited knowledge of the interaction process and a limited database of measured ice loads. For this reason, serious experimental and field programs were required to shed some much needed light on the subject of ice structure interaction.

Ice mechanics has been used to fill the void of knowledge in this field of materials science. Research at full scale with instrumented structures and vessels, at medium scale with indentation tests in both sea and glacial ice, and laboratory work on the properties of ice under various conditions have all been performed. In general, these have shown that ice behaves in a complex manner depending on the type and microstructure of the ice encountered, the loading conditions, the temperature of the ice, and scale effects. Ice failure in the field has been observed to be a dynamic process where ice failure at the ice-structure interface is characterised by a crushed layer of pulverised ice being extruded as the interaction takes place. Within the crushed layer, a large percentage of the total load is transmitted through dynamic zones of high pressure which appear and disappear at random in fractions of a second.

In the laboratory, work has focused on establishing and confirming constitutive models for ice, essentially equations that will predict the response of ice when it is subjected to specific stress and strain conditions. As theoretical models are conceived, laboratory testing and field data help to define parameters and coefficients for the models as well as to check their validity over large ranges of conditions. An important aspect of ice-structure interaction that is currently being investigated and will be reviewed in this work is the behaviour of high pressure zones. It is believed that understanding the mechanical behaviour of ice within the high pressure zone and the associated layer of highly damaged crushed ice that accompanies this deformation is essential in the development of the next generation of constitutive models for ice. For this reason a test program was established to investigate the effects of higher strain rates and large amounts of strain (or damage) on laboratory grown polycrystalline ice tested under conditions believed to be present in ice in the field.

1.2 Focus

The focus of this thesis specifically is to investigate the effects strain rate, total strain, creep load, and confining pressure on the deformation, microstructural change, and damage of granular freshwater ice under several triaxial stress states and histories. The goal is to reproduce conditions encountered within high pressure zones in the laboratory using triaxial testing, simulating some of the localised effects of ice-structure interactions on a small scale. From data and observations obtained in this study a clearer understanding of the ice-structure interaction process will be achieved as well as obtaining information that will lead to the calibration and verification of constitutive relations for ice presently being developed. In particular, a constitutive model developed at Memorial University of Newfoundland which takes into account the effect of hydrostatic pressure on the ice will be investigated.

The work covered in this document is summarised below:

1. A literature review of the damage process, creep response, and constant strain rate response of freshwater granular ice under triaxial conditions with an emphasis on high pressure zones and their role in ice-structure interactions was done.
2. A review of damage mechanics and constitutive relations for ice, leading to the latest model is presented.
3. Test matrix, its goals, and the motivation for these tests with respect to previous testing are discussed.
4. The experimental procedure and apparatus used in this study is presented.
5. A discussion of the results of the triaxial testing and the application of the collected data to the calibration of the model is presented.
6. The pressure-dependent constitutive model and the methods and corrections used in the calibration followed by model predictions are derived and discussed.

7. Concluding remarks and recommendations for further investigation into this subject are given.

Chapter 2

The Behaviour of Ice

In order to develop models for the interaction of ice with structures, a proper understanding of the mechanics of ice is necessary. In this chapter the state of the art of ice mechanics will be described, relating theories for large scale ice structure interaction to laboratory work as well as describing the behaviour of ice on a microscopic level within the ice-structure interaction zone. Beginning with the microscopic make-up of ice, ice-structure interaction mechanics will be reviewed. Other topics covered will include the role and characterisation of damage in the failure of ice as well as related modelling issues.

2.1 Ice as a Material

2.1.1 The Microstructure of Ice

Natural ice of interest to this study is from two general sources: sea ice, with its origins on the oceans, and glacial ice calved from glaciers and ice fields, the result of the accumulation of snow and atmospheric precipitation. These two, although from completely different sources, are made up of the same type of ice, ice 1h. The 'h' refers

to the hexagonal microstructure of the material. This form of ice is the only type that exists naturally on earth at normal pressures and temperatures. Other forms can exist at high pressures (above 200 MPa) and low temperatures (below -110°C) but these are almost never observed outside of the laboratory and are usually studied by those interested in ice in other parts of the solar system and on other planets.

The hexagonal crystal formation of ice is composed of oxygen atoms at the vertices of a tetrahedron. Each oxygen atom within the crystal has four bonds to hydrogen atoms, three in the plane of the hexagon and one in the adjacent plane either above or below it. This plane is referred to as the basal plane and is the preferred plane of deformation within the crystal. The direction perpendicular to the basal plane is called the c-axis or optic axis of the crystal. The c-axis is such that optical methods can determine its orientation by using polarised light, as light incident parallel to the c-axis will pass through the crystal normally while birefringence will take place with light at an oblique angle of incidence. This phenomenon allows the crystallographic analysis of ice sections with a simple white light source and a set of crossed polarising filters, a relatively easy task compared to other materials.

Ice expands on freezing, reaching its maximum density as water at about 4°C. In nature the homologous temperature of ice is usually very near 1.0, and because of this ice is very much susceptible to pressure melting. The theoretical relation for this effect at 0°C for small pressure changes is (Hobbs, 1974):

$$dT_m = -0.0738°C/MPa \qquad (2.1)$$

where T_m is the melting temperature. At larger pressures, the relation between the melting point and pressure is no longer linear. It has been shown that 54 and 110 MPa of pressure are required to melt ice initially at -5 and -10°C, respectively (Nordell, 1990). Both of these relationships are shown in Figure 2.1.

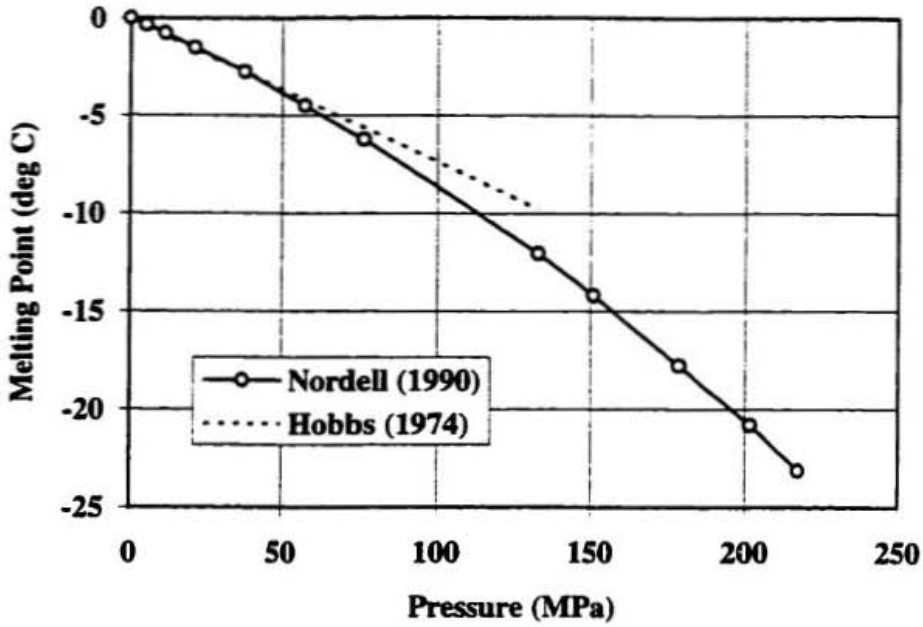

Figure 2.1 Melting temperature versus pressure for ice Ih from Nordell (1990) and Hobbs (1974).

2.1.2 The Natural Formation of Ice

Ice growth in nature is divided into two stages called primary and secondary ice growth. Primary ice growth includes the transition beginning with the nucleation from dust, snow, or other precipitation up to a thin continuous sheet of ice on a lake or expanse of salt water. Secondary growth is the growth of ice downwards from an established ice sheet. Primary growth in ice is affected by atmospheric conditions and precipitation, surface conditions such as waves and wind, and impurities such as salt. Each of these factors affect both the nucleation rate, the shape of ice crystals, and the speed and direction of growth in the ice sheet. Secondary ice growth is mainly controlled by the salt content of the water and the temperature gradient in the ice sheet.

Once an ice crystal has nucleated, its growth is primarily in the basal plane if there are no other restrictions, although growth can occur in any direction under the right conditions. For more on this subject the reader is referred to Cammeart and Muggeridge (1988) and Sanderson (1988). Secondary ice growth can only take place where there already exists an ice cover over the water surface. It is at this point in which a distinction between salt water ice and freshwater ice is made. As the ice sheet grows downwards in salt water, brine pockets will be trapped between columnar ice crystals growing from the bottom of the ice sheet. These pockets are the reason salt water ice, at least in its first year, is typically weaker than freshwater ice. In multi-year ice, the brine pockets can drain leaving empty brine channels to flood and freeze with fresh melt water, producing the stronger multi-year ice often encountered in the arctic. See Michel and Ramseier (1971) and Nadreau and Michel (1984) for more on ice sheet formation, growth, and classification.

Ice deformation at the large scale is apparent in many ice floes. The phenomena of rafting, fingering, and ridging are all part of the growth and life of a natural ice sheet. This last formation, the ice ridge, is often the strongest part of an ice sheet, especially when made up of ridged ice that has survived more than one year. It is these multi-year ice ridges that often cause the greatest threat to ice breaking vessels and other structures in arctic waters, however all ice induces some sort of loading on structures during an interaction. The description of such an interaction follows in Section 2.2.

2.2 The Mechanics of an Ice-Structure Interaction and High Pressure Zones

In this work emphasis will be placed on the local effects of ice-structure interactions on the microstructure of the ice, its deformation, and locally transmitted loads and

pressures. The problem of determining global ice loads will not be addressed. Also, due to the large number of failure mechanisms that are possible and have been observed in the field, this investigation will be limited to the crushing failure of ice, ignoring other failure modes such as: radial cracking, buckling, circumferencial cracking, flexure, and large scale spalling. Pure creep is not listed with these failure mechanisms as it can be considered a special case of crushing failure where there is no spalling, extrusion of crushed ice, and high frequency oscillations in the load.

The area of a structure that makes contact with the ice during the interaction defines the interaction zone. It is the description of this area and the activity in and around it that researchers are striving to achieve. The ice in this area will behave differently depending on several characteristics: the deformation rate, the scale of the ice with respect to the structure, the temperature of the ice, and its microstructure. For example, a relatively high temperature will lead to a visco-elastic deformation while lower temperatures and high strain rates will result in a brittle type of fracture. In the present case a typical temperature of about -10°C and a deformation rate on the order of 0.1 m/s will be assumed.

Initially as the ice makes contact with the structure any high points on the ice will be spalled off or crushed as the structure begins to indent the ice surface. Once an interaction area of sufficient size is reached the ice starts to take on the full load of the interaction. Since we are assuming the ice will fail by crushing and not by simple creep (ductile) or brittle failure, a complex interaction begins at the ice-structure interface. It is this steady state deformation beyond the initial transient contact that is of interest here.

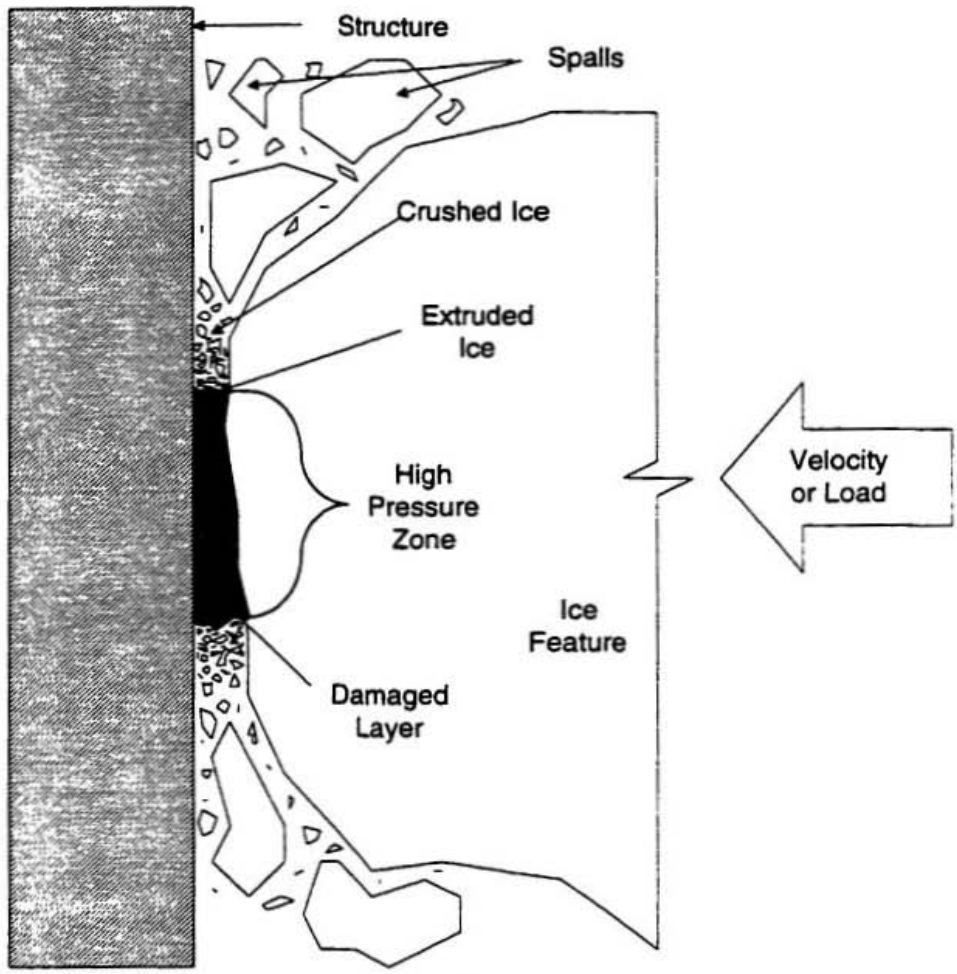

Figure 2.2 Diagram of ice-structure interaction event showing a high pressure zone situation.

The ice nearest the indentor will be formed into a crushed layer as shown in Figure 2.2. This layer of ice adjacent to the structure consists of parent ice that has undergone significant microstructural change in the form of microcracking, recrystallisation, pressure melting, and sintering (Jordaan and McKenna, 1989). The ice within the pulverised layer is what has been observed to be extruded from the interaction zone as fine granular ice in indentation tests. The layer has been reported to vary from a few

millimetres to 170 mm or more in thickness (Meaney and others, 1991), but is typically about 40 mm thick. This ice layer is believed to be responsible for oscillations in load (Jordaan and Singh, 1994, Jordaan and McKenna, 1989) often associated with ice-structure interaction of this nature. This argument is supported by studies on crushed ice between parallel plates by Spencer and others (1992) and Singh and others (1993).

Within this crushed layer, once a steady state deformation regime is reached (not necessarily a constant deformation rate) and often before, high pressure zones are present. These are zones of local high pressure within the crushed layer that are responsible for transmitting a large fraction of the load, well beyond half the total load (Johnston and others, 1995), to the structure from the ice. High pressure zones have been observed to be about 20 to 50 cm in diameter (0.03 to 0.2 m^2 in area) in both field tests and vessel ramming trials (Jordaan and others, 1991). Zones observed against instrumented hull plating on the C.C.G.S. Louis S. St. Laurent and reported by Glen and Blount (1984) during ice ramming against ridges and regular icebreaking had a duration of between 0.01 and 0.1 s, a maximum peak pressure of 53 MPa, and an average magnitude of 23 MPa for all peaks recorded. Sensors embedded in the ship's forward plating were 7.94 mm in diameter. Other tests at Hobson's Choice Ice Island showed a maximum peak pressure of 70 MPa during pressure pulses about 0.5 s in duration during constant speed indentation tests. Pressure sensors in the indentor face were 12.7 mm in diameter (Frederking and others, 1990; Johnston and others, 1995).

High pressure zones are random in nature both temporally and spatially (Jordaan and others, 1997). Their shape is also random and dynamic, changing as the ice is deformed. The distribution of the zones has been estimated to be about one per square meter (Jordaan and others, 1997), but the characterisation of the distribution in time and space is not pursued here so that we may concentrate on the mechanics of the zones themselves.

As indicated above, the zones are short lived phenomenon that appear and then disappear just as another zone is materialising. The zones tend to propagate themselves in this way so that there is always at least one zone transmitting the load to the structure (Jordaan and others, 1997).

Microcracking is at work in high pressure zones and in areas behind the crushed layer, but crack propagation is suppressed by the confinement of the surrounding material and inhibits spalling in the immediate area of the zone. In other areas where there is less confinement, cracks can coalesce to form spalls. These spalls actually help continue the process allowing critical zones to appear in other parts of the interaction area (Jordaan and Singh, 1994, Jordaan and others, 1991). As the load is transmitted to these other and often smaller areas, the same large load and deformation causes high stresses and the development of new high pressure zones.

Field indentation tests have shown what appear to be two types of ice in the crushed layer at the surface of the indentor. The first is crushed, highly damaged, and simply disintegrates to the touch. It does not appear as if it could support any sort of load without confinement and is often associated with the lower pressure areas of the interaction (Meaney and others, 1991). It is white in colour, suggesting that air has been entrained within the ice in the form of bubbles during the grinding and extrusion process. A second bluish zone of ice is also present in some cases. Although this ice appears intact it has actually undergone significant microstructural change as can be attested by thin sections of the area which show evidence of recrystallisation and sintering (Meaney and others, 1991). Thin sections of the ice beyond the crushed layer have also shown little or no damage to the parent ice a relatively short distance (100 mm) from the indentor surface.

The change in structure of the ice from undamaged parent ice to highly damaged and deformed ice is the focus of this work. Tests described later and performed under triaxial conditions were developed to increase the understanding of this microstructural change and how it relates to the transmission of large loads during ice-structure interactions. In order to understand this one must first start at the beginning with the small scale behaviour of ice.

2.3 The Small Scale Behaviour of Ice

If an attempt is to be made to understand the mechanics of the ice within high pressure zones the mechanics of ice in general must first be understood. The following section will deal with laboratory test programs and will go on to explain how ice is represented in constitutive relations using viscoelastic theory. From this point forward any references to ice should be taken to refer to granular fresh water ice unless otherwise indicated. Of course ice in the field, especially salt water ice, will vary from sample to sample with respect to both its structure and properties. Brine pockets, age, granular structure, and temperature all affect the physical properties of ice. In the laboratory, however, a uniform ice is used so that results can be compared and evaluated.

The mechanical properties of ice, as described by Sanderson (1988), can be classified into two areas: continuum behaviour and fracture behaviour. The first represents the elastic and ductile deformation of ice, while the second is related to the development of large amounts of cracking and brittle failure. Although much of this work is related to continuum behaviour, both will be discussed below.

2.3.1 The Creep of Ice

A large number of studies based on experimental work under uniaxial and biaxial stress conditions have been undertaken (Sinha, 1979; Mellor and Cole, 1983; Cole, 1983;

Jacka and Maccagnan, 1984; Smith and Schulson, 1993, to name a few). However, relatively fewer studies have looked at the deformation and failure of ice Ih under triaxial confinement (Jones, 1982; Jones and Chew, 1983; Jones and Johari, 1987; Stone and others, 1989; Kalifa and others, 1992; Rist and Murrell, 1994; Rist and others, 1994; Gagnon and Gammon, 1995; Stone and others, 1997).

Let us now consider what happens to an ice sample as it is suddenly loaded by a constant stress, also known as a creep test. It should be noted that references to creep tests in this work represent a constant stress or constant load test, and not a constant strain rate test, as others working in ice may previously have defined it. Initially, the ice deforms elastically with the application of the load, similar to other solids. This is followed immediately by a delayed elastic deformation that grows asymptotically to a finite level over time, superimposing its deformation on the elastic strain. A third component, viscous creep, is also present. All three responses can be added to yield the total response of the ice and are shown graphically in Figure 2.3. This figure describes the idealised response of the ice during a creep test as well as the response of the ice after the load has been removed. Note how the delayed elastic strain is recovered along with the elastic strain. The viscous strain is not recovered after the load is removed so that the permanent deformation after unloading is due to viscous creep in the ice.

Of the three strain components introduced above, the elastic strain is the deformation associated with the displacement of the atoms and their bonds and is completely recoverable. It is represented by the following equation:

$$\varepsilon_e = \frac{\sigma}{E} \tag{2.2}$$

where σ is the stress and E is the Young's modulus of the ice. The delayed elastic strain

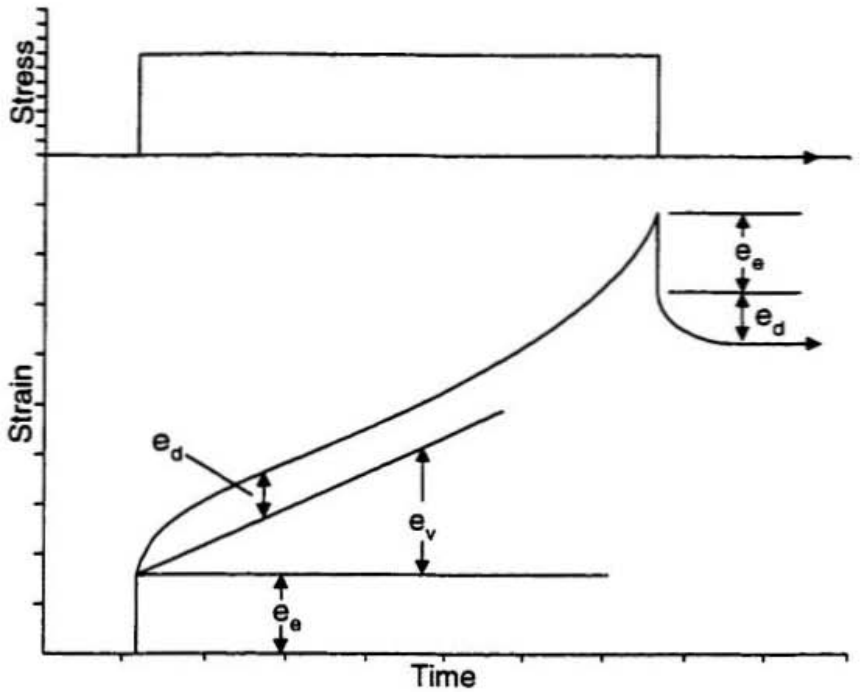

Figure 2.3 Constant stress test strain history showing the three strain components used to describe creep.

is asymptotic in nature and contributes a limited amount of strain to the total. The viscous strain in the ice is due to microstructural change in the ice from different sources that will be discussed later as deformation mechanism are introduced.

Many constant stress tests in the past have been performed uniaxially with no confinement on the sample. These were, for the most part, performed at relatively low stress over long periods of time. In most cases the goal of the work was not the development of constitutive relations for ice but simply understanding the mechanics and micromechanics of the response. It should be understood that ideally the deformation and failure of ice is independent of the type of loading, whether it is constant stress, constant strain rate, or constant stress rate. The actual mechanisms acting on the ice will be the same, their relative effects depending solely on the state of stress and previous stress and

strain history. The distinction between constant stress and constant strain rate tests is based simply on the fact that some variable must be controlled while performing a test and that these variables in particular, stress and strain rate, are both relatively simple to manage.

2.3.1.1 Pressure

Confinement is an important issue in the testing of ice, since in a true interaction ice is certainly not subject to purely uniaxial loads. Pressures develop and act on the material both parallel to the axis of loading as well as perpendicular to it, applying a confinement that tends to hold the ice together. The end result is a material that can be significantly stronger than in its uniaxial state.

Jones and Chew (1982) have shown that low levels of confinement lower the secondary or minimum creep rate of polycrystalline ice. However, the creep rate then passed through a minimum between 15 and 30 MPa of confinement, increasing with added pressure. The tests were performed at -9.6°C and a low differential stress of 0.47 MPa. Pressure melting at grain boundaries, where stress concentrations arise, is suggested as the cause of the softening of the ice in the high pressure regime (this point will be revisited several times).

The effect of confining pressure on ice is also related to crack motion and sliding along the crack interface. Confinement tends to increase the forces that close cracks and therefore limits the general effect of cracking on the ice as far as the strength and deformation are concerned. The result is to make ice that appears moderately damaged by cracks behave much like undamaged ice (Stone and others, 1997).

2.3.1.2 Grain size and Orientation

Jacka and Maccagnan (1984) have reported on uniaxial compression tests on polycrystalline ice at -3°C with a low constant differential stress of 0.2 MPa. The purpose was to investigate the microstructural change within the sample with respect to the grain size and crystal orientation, taking thin sections of samples at various strain levels. Grain size was found to increase with strain up to the maximum total strain of 32.5%, changing from 2.2 mm initially to 4.8 mm at the end of the test. Grain orientation was described as developing from purely random to a circle girdle fabric, with the c-axis at an angle of about 27° from the horizontal plane distributed randomly about the axis of differential loading.

Grain size also decreases with increased deformation in higher stress and higher strain tests (Stone and others, 1989). This is believed to be related to the effects of grain boundary area. However, the area will have an effect on the recrystallisation versus microcracking mechanism within the ice only so long as loading and temperature conditions are not preferential to one or the other. The magnitude of the strain rate or stress applied along with both the time (duration of the loading) and confining pressure work in establishing the relative amounts of recrystallisation and microcracking in the ice. High pressures and temperatures inhibit microcracking and enhance recrystallisation. Otherwise recrystallisation and grain boundary migration tend to thrive where large grain boundary areas (small grain sizes) are present while microcracking is more predominant in ice with larger grains.

2.3.2 Constant Strain Rate Deformation of Ice

A second way, and possibly the most widely used method, of studying the deformation of ice in the laboratory is the constant strain rate test. An idealised curve for a constant strain rate test is shown in Figure 2.4 as stress versus strain, and clearly shows

the peak stress often used to describe the strength of ice under specific conditions of temperature, grain size, or pressure (Mellor and Cole, 1982). In constant strain rate deformations at low strain rates a second peak is often visible in the curve slightly ahead of the major peak. This secondary peak, or initial yield point as it has been referred to in the literature (Mellor and Cole, 1982; Schulson and others, 1984) marks the onset of microcracking in the ice. More on the peak stress and its relation to the deformation behaviour is discussed with respect to results in Chapter 4.

Often the difference between constant strain rate tests and constant deformation rate tests is not clearly defined. This difference is related to the calculation of true and engineering strain. The engineering strain is simply defined as the change in the length of

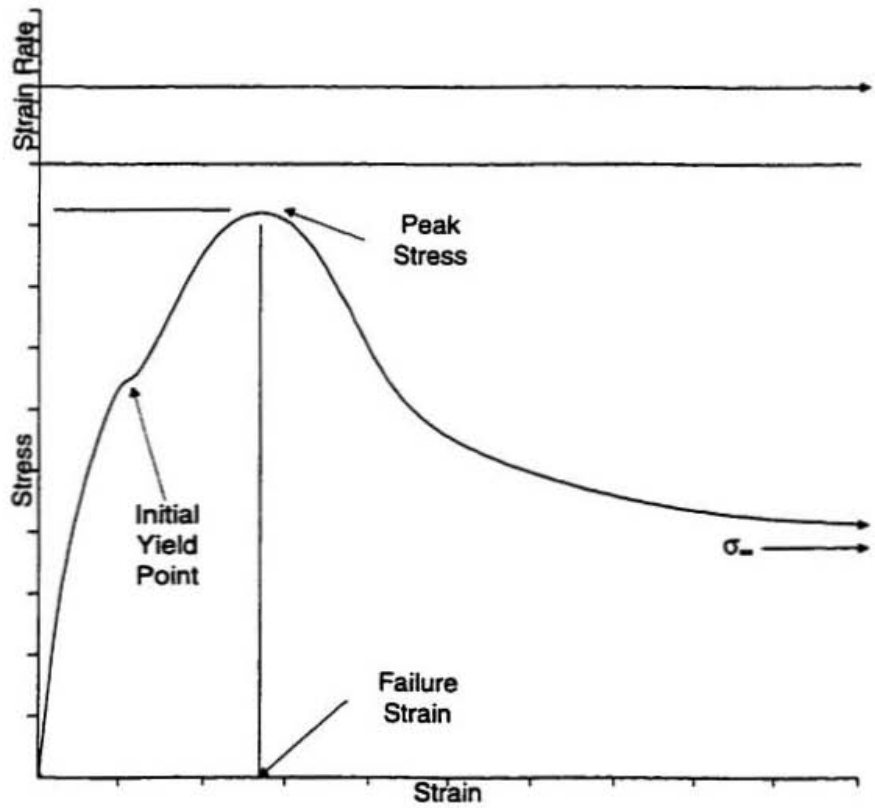

Figure 2.4 Stress versus strain for a typical constant strain rate test showing the peak stress of the material.

a specimen, $l_f - l_0$, divided by the gauge length, l_0:

$$\varepsilon_E = \frac{l_f - l_0}{l_0} \tag{2.3}$$

True strain is defined as the change in length of a specimen divided by its new length at each interval of measurement. As the intervals become very small, this can be expressed as an integral where a small change in strain ($d\varepsilon = \frac{dl}{l}$) is integrated over the change in length from l_0 to l_f:

$$\varepsilon_T = \int_{l_0}^{l_f} \frac{dl}{l} = \ln(l)\Big|_{l_0}^{l_f} = \ln(l_f) - \ln(l_0) \tag{2.4a}$$

When Equation 2.3 is solved as $l_f = l_0(1+\varepsilon_E)$ and substituted for l_f into Equation 2.4a the result is:

$$\varepsilon_T = \ln(l_f) - \ln(l_0) = \ln(l_0(1+\varepsilon_E)) - \ln(l_0) = \ln(l_0) + \ln(1+\varepsilon_E) - \ln(l_0) \tag{2.4b}$$

where the expression reduces to a simple function for the true strain:

$$\varepsilon_T = \ln(1+\varepsilon_E) \tag{2.4c}$$

All strains in this work are represented as true strain unless otherwise indicated.

In a constant strain rate test one of the feedback or control channels is usually the strain, calculated from the amount of stroke or deformation at some point and the gauge length. By controlling the strain rate, calculated from this signal, a constant strain rate test is achieved. If the test is performed without the use of this feedback then a constant deformation rate is used to control the test. This results in a test where the strain rate is changing as the deformation progresses. This can be seen if one considers the same deformation or advance rate on a sample while it is at its initial length and then considering the same deformation rate once the sample reaches a smaller fraction of its original length. The difference in strain is insignificant for small deformations (engineering strain and true strain are essentially the same), but when strains greater than

about 4% are reached the difference between the two begins to become significant and should be taken into consideration.

Another problem in testing to high strain levels, specifically in compression, is the barrelling effect of the specimen on stress and strain. The lateral strain which causes barrelling typically increases the cross section of the specimen at the midpoint and therefore reduces the stress. If the system is not set up to correct for this when calculating stress in the sample, significant errors (up to 35% for the sample sizes and strains in this study) may result. More about this and other issues dealing with corrections to data and triaxial testing of ice will be discussed in Chapter 3.

Experimental work on constant strain rate testing of ice is widespread as the tests are relatively easy to perform and interpret. Deformation at constant strain rate has been characterised in the past by many researchers. The following touches on a few reports by some of these to give an overview of the work done on ice at constant strain rate both uniaxially and triaxially.

2.3.2.1 Pressure

Pressure affects the constant strain rate test in much the same way as the constant stress test. The strength of the material under confinement is increased when compared to the unconfined strength at strain rates greater than 10^{-5} s^{-1} (Jones, 1982; Kalifa and others, 1992). The work by Jones is thorough, covering strain rates from 10^{-7} to 10^{-1} s^{-1} up to a maximum pressure of 85 MPa. The testing was performed at a temperature of about -11°C. Jones (1982) showed that the most dramatic effect of the confinement in strengthening the ice is at high strain rates (10^{-2} to 10^{-1} s^{-1}). Strengths twice the magnitude of the unconfined strengths were reported at these strain rates. If the pressure alone is considered the strength showed a decreasing trend as pressures go past the 30 to

40 MPa mark. This was attributed to pressure melting as the combination of stress and pressure reduce the overall melting point at grain boundaries.

Kalifa and others (1992) reported results that were similar for a temperature of -10°C and pressures up to 10 MPa. The main focus of this research was microcracking and fracture, similar to reports by Rist and Murrell (1994) and Rist and others (1994) on triaxial tests with ice where the ductile to brittle transition zone was investigated.

In triaxial testing a confining pressure can be applied by using an actuator for each primary axis or by using a confining medium such as nitrogen or silicone oil. In the case of the latter the medium must be kept from making direct contact with the specimen to avoid interaction with cracks. This effect was dramatically represented in a test by Rist and others (1988) when a jacket was suspected of leaking during a triaxial test. The result of the leak was a specimen which experienced rapid softening after the peak stress. A similar sample with a jacket that was not compromised showed less softening. Both tests were performed at about the same pressure, near 11 MPa, and the same strain rate and temperature. It is believed that the introduction of the confining medium to the ice resulted in pressure between crack faces. This, instead of closing cracks, reduced friction between the two surfaces causing a softening of the material.

2.3.2.2 Temperature

Tests by Rist and Murrell (1994) described the temperature effect to be very much as expected with ductile behaviour at high temperatures and brittle behaviour at low temperatures. Tests at temperatures of -20 and -40°C are also presented in the context of studying the brittle behaviour and fracture of ice at varying strain rates. For the most part the testing was performed in temperature ranges beyond the range of interest of the present study.

2.3.2.3 *Grain Size*

Grain size plays a large role in ice behaviour both at constant strain rate and constant stress. Tests by Schulson and Cannon (1984), and Cole (1987) suggested that the peak stress increases with decreasing grain size for most strain rates up to 10^{-3} s^{-1}, however, there was a discrepancy in the results of these two studies at low strain rates (lower than 10^{-6} s^{-1}).

It is hard to isolate the effect of grain size in some cases, especially at high strain levels as the grain size is continually changing as the test goes on. By recrystallising grains, the ice can either develop a larger average grain size (in very slow tests) or a smaller average grain size (in faster tests). Recrystallisation tends to take place more readily on smaller grained specimens, allowing large ductile deformations. This has been linked to the large grain boundary area available for recrystallisation and grain boundary migration, as well as the ability of the larger grained ice to develop higher stress concentrations than ice with a smaller grain size (Cole, 1986, 1987). The effect of grain size on microcracking with respect to strain rate response reflects the opposite, where limited numbers of grain boundaries use cracking to dispose of accumulated strain energy and dislocations. This microcracking in turn can aid the recrystallisation process by increasing the number of grain boundaries.

2.3.3 Damaged Ice

Constant strain rate tests have been the most widely used means of applying known amounts of 'damage' to ice. Kuehn and others (1988) and Stone and others (1989; 1997) have presented work on this subject. The former investigated the effects of damage on the ductile to brittle transition zone. The work by Stone and others (1989; 1997) involved subjecting ice to known amounts of strain at either a constant deformation rate or a constant or monotonically increasing load in order to quantify damage to the ice based on

a damage formulation. More on damage functions will be presented in Section 2.4 once constitutive models have been discussed.

The most common types of damage tests are constant strain rate tests to fixed levels of strain and are often followed by a creep or second constant strain rate test, possibly with a period of recovery between the two. The constant strain rate tests are often easier to control and can be programmed to stop at specific strain levels easier than other types of tests. Constant stress tests have a tendency to develop runaway creep once the tertiary creep phase is reached and can be less than ideal when precise control is required.

In Stone and others (1989) tests were performed by applying a constant strain rate deformation followed by a second constant strain rate deformation of either higher or lower strain rate. The results showed that the ice responded by producing a second slightly higher peak when the strain rate was greater, and no peak at all for strain rates that were less than the initial rate. The paper also suggested a simple damage model based on the reduction in area of the specimen due to cracking.

Kuehn (1988) reported on the strength of columnar saline ice following a constant strain rate test, similar to the work discussed above. These tests were performed uniaxially at -10°C both parallel and perpendicular to the columns in the ice. Results showed that the strength of the ice decreased on the second loading when compared to intact ice strengths.

In general, laboratory experiments indicate that ice will become softer following an initial damage test either by showing a decreased peak stress (for subsequent constant strain rate tests) or a higher minimum strain rate (within a subsequent creep test). In the past this was mainly associated with the damage caused by extensive microcracking throughout the ice, as papers by Stone and others (1989), Jordaan and others (1992), and Jordaan and Xiao (1992) indicate. However, in a later report, Stone and others (1997)

suggest that microcracking, although a significant part of damage at low strains, is not the only aspect to be considered, citing recrystallisation and pressure melting as sources of damage.

2.3.4 Describing the Creep of Ice

Continuum behaviour in ice has been modelled in the past by using phenomenological models to describe the rheology of ice. These are discussed below, along with more rigorous formulations based on viscoelastic theory.

As ice deforms during a creep test it undergoes three stages of deformation. As the load is applied primary creep begins and continues through to the end of the delayed elastic strain. This leads to a minimum creep rate at the point of inflection of the creep curve. The minimum creep rate and the associated plateau in the strain rate are called secondary creep. Secondary creep is followed by tertiary creep as a result of viscous deformation, and the strain at this point can quickly run away with rapidly accelerating creep. A sample creep curve in Figure 2.5, similar to that in Figure 2.3, shows each of the stages of creep defined above.

Primary creep is associated with the elastic strain mentioned earlier, along with the decelerating delayed elastic strain. As for secondary creep, there is some debate as to whether it truly exists or is simply a minimum creep rate separating the two other forms of creep. This is left for others to debate as the creep response certainly does not depend on its classification. Tertiary creep has been attributed to both the existence of extensive microcracking (Sanderson, 1988) and recrystallisation at grain boundaries (Frost and Ashby, 1982), both brought on by the accumulation of dislocations at the grain boundaries. It is likely that both recrystallisation and microcracking are playing a part in the deformation, their relative contributions depending on other conditions within the ice, including pressure and temperature. Many scenarios are possible, including strictly

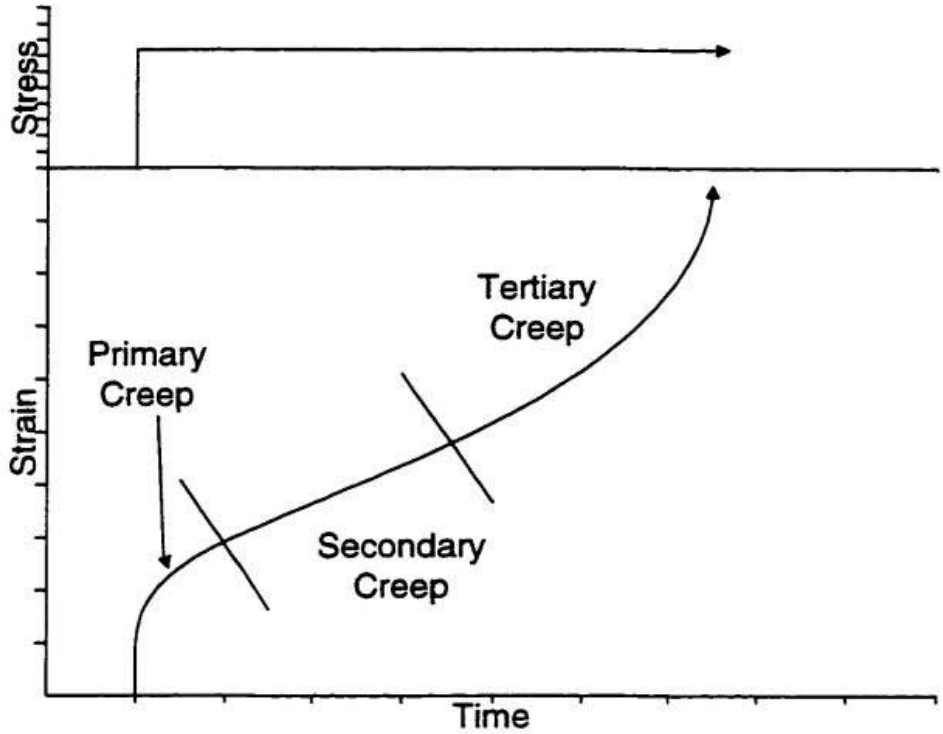

Figure 2.5 Constant stress test strain history showing the three creep regimes.

recrystallisation or microcracking producing tertiary creep. Recrystallisation is seen as being a regenerative type of deformation since once ice has been recrystallised it is dislocation and crack free and can undergo primary creep once again, contributing to the overall increase in the strain rate associated with tertiary creep.

An interesting paper by Glen and Ives (1988) shows the effects of inhibiting recrystallisation and grain boundary migration in ice subjected to creep loads. Using fish antifreeze proteins (antifreeze glycopeptides), the creep rate during constant stress tests using treated ice was found to be reduced when compared to constant stress tests on regular granular ice. It was explained that the ice aggregate could no longer deform using recrystallisation and grain boundary migration due to the effects of the antifreeze proteins.

This strengthens the argument that recrystallisation plays a large role in the tertiary creep deformation of ice but is not solely responsible for it.

Sinha (1978; 1983) developed a phenomenological relation based on viscoelasticity which describes the creep response of ice under constant and monotonic uniaxial loading conditions and constant temperature. The expression is divided into three terms which represent the instantaneous elastic, delayed elastic, and viscous parts of the response and are summed to give the total response as follows:

$$\varepsilon = \varepsilon_e + \varepsilon_d + \varepsilon_v \tag{2.5}$$

The elastic term ε_e, is simply the ratio of the stress to the elastic modulus of the ice, as before:

$$\varepsilon_e = \frac{\sigma}{E} \tag{2.2}$$

The second term, or delayed elastic term ε_d, takes into account the temperature of the ice as well as the initial grain size:

$$\varepsilon_d = \left(\frac{d_1}{d}\right)\left(\frac{\sigma}{E}\right)^s (1 - \exp[-(\alpha t]^b) \tag{2.6}$$

where d_1 is the grain size, d is the reference grain size, σ is the stress, E is the elastic modulus, c_1 and α are constants, s is equal to 1, and b is 0.34 ($\approx 1/n$, where n is 3). The third term is similar to the power law developed by Glen (1955) and represents the viscous creep of the ice:

$$\varepsilon_v = \varepsilon_t \left(\frac{\sigma}{\sigma_0}\right)^n \tag{2.7}$$

where $n = 3$, σ is the stress, σ_0 is the reference stress, and ε_t is the reference strain rate.

In cases where stresses are sufficiently high or where ice is allowed to creep for large periods of time, power law breakdown may develop. This is the breakdown of Glen's

Law, where the equation fails to predict the observed strains. Tertiary creep is often mentioned in the context of power law breakdown where the material in question develops a form of runaway creep. In this situation the exponent, n, has to increase to keep up with the accelerating creep. Sinha's equation, although useful for many engineering applications, does not describe tertiary creep (i.e. cannot handle power law breakdown) and for this reason will not be investigated any further. For a more rigorous method the classic formulation of viscoelastic theory will be used.

The classic formulation of viscoelastic theory begins with the generalisation that the creep strain can be expressed as a function of stress, σ, temperature, T, and time, t, as $\varepsilon = F(\sigma, T, t)$. Boltzman's superposition principle can be used to describe creep expressions for uniaxial strain ε and stress σ for linear viscoelastic materials:

$$\varepsilon(t) = \int_0^t D(t-\tau)\frac{d\sigma(\tau)}{d\tau}d\tau \tag{2.8}$$

$$\sigma(t) = \int_0^t E(t-\tau)\frac{d\varepsilon(\tau)}{d\tau}d\tau \tag{2.9}$$

where τ is a given time in $[0, t]$ and $E(t)$ and $D(t)$ are the relaxation modulus and creep compliance functions, respectively, which describe the time history of stress and strain. A simple example is a function of the form:

$D(t) = D_0+D_1t+D_2t^b$

which can be defined by a set of constants: D_0, D_1, D_2, and b $(0 < b < 1)$ and describes the history of a material over time, for any time t.

A second form of this function, developed by Biot (1954), is based on the thermodynamics of irreversible processes and is expressed as an equation of state with respect to time of the form:

$$D(t) = \frac{1}{E_1} + \frac{t}{\mu_1} + \sum_{i=2}^{n} \frac{1}{E_i}\left\{1 - \exp\left(-\frac{E_i}{\mu_i}t\right)\right\} \tag{2.10}$$

and:

$$E(t) = E_1 + \sum_{i=2}^{n} E_i' \exp\left(-\frac{\mu_i'}{E_i'}t\right) \tag{2.11}$$

where E_i, μ_i, E_i', and μ_i' are material constants. This formulation uses the present state of stress in the material along with a set of state variables to describe the strain response explicitly. The same is done using the present state of strain to describe the stress response. Schapery (1981) has also developed a modified superposition principle which uses non-linear F(t) and G(t) to define the material model.

A Burgers body can be used to describe these and most other viscoelastic models. This mechanism is the combination of two sets of non-linear dashpots and springs, one set used in parallel to form a Kelvin unit, and the other in series forming a Maxwell unit as shown in Figure 2.6. It has been found in practice that other forms (Figure 2.7) can also be used to represent the mechanical properties of a material. The discussion presented here will be limited to the model body described in Figure 2.6. It should be noted that the use of the Burgers body is a generalised case of the formulation described above. The spring in the Maxwell unit, k_m, describes the elastic response of the ice. The non-linear dashpot in the Maxwell unit then represents the viscous deformation of the ice, where η_m is the viscosity. The Kelvin unit as a whole is left to represent the delayed elastic deformation with parameters of elasticity k_k and viscosity η_k.

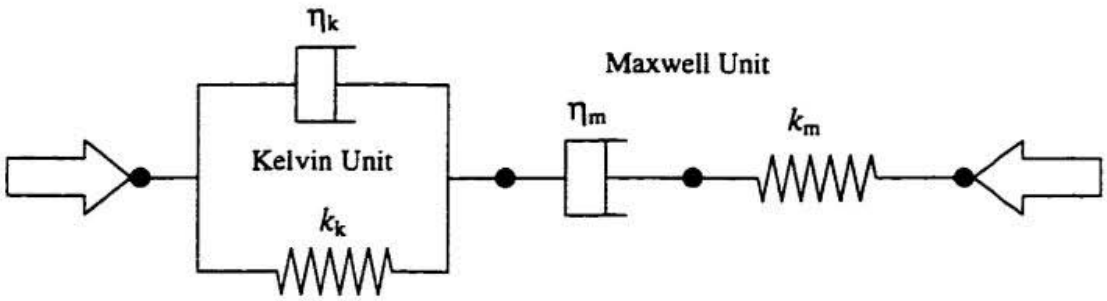

Figure 2.6 Burgers body showing individual Kelvin and Maxwell units and their associated springs and dashpots.

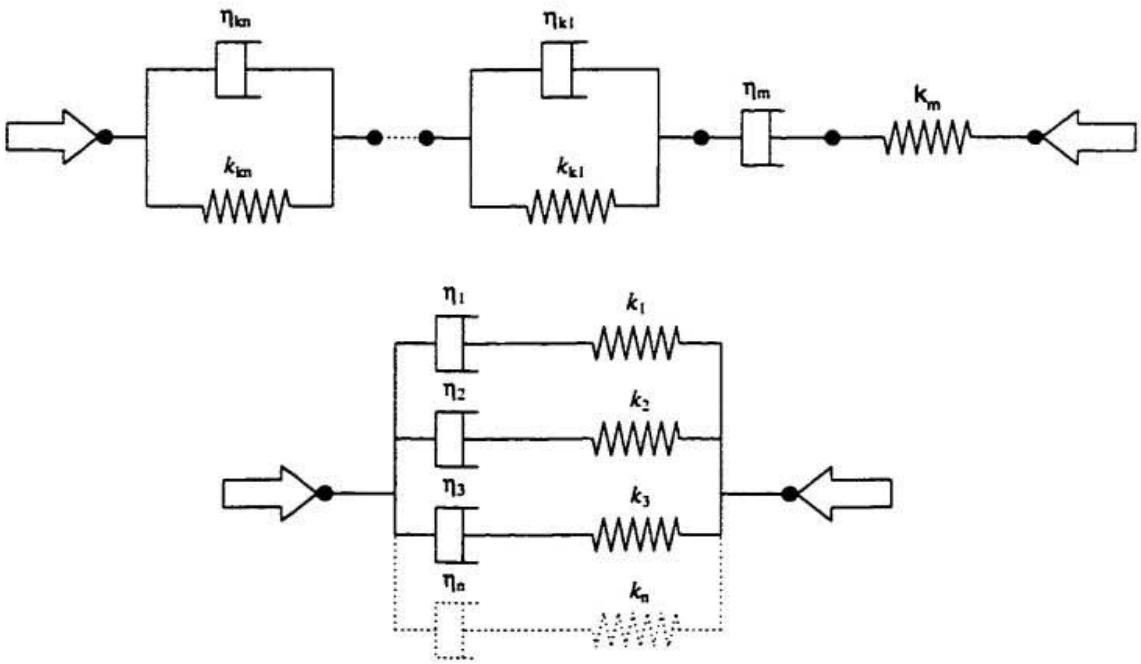

Figure 2.7 Spring and dashpot systems representing canonical forms of viscoelastic models.

2.4 Damage and Constitutive Modelling

2.4.1 The Effects of Damage

The laboratory testing of ice at Memorial University over the past several years has been mostly kept to small strain levels over various levels of confinement and temperature, at moderate strain rates. Similarly, constitutive relations for damaged and undamaged ice developed in the past have mostly been valid for limited stress and strain conditions under low confinement. In order to develop a full scale constitutive relation for ice-structure interactions, the mechanics of ice must be understood for both large strains and a wide range of strain rates and confining pressures.

It has been shown that the effect of damage on the ice is to reduce the elastic modulus of the material as well as to enhance the creep rate. Confinement also plays a role in controlling the creep rate, due to its effects on microcracking. At low confining pressures (< 5 MPa), prior damage enhances the creep rate when compared to simple uniaxial tests, while higher confinement (> 20 MPa) limits the effects of prior damage on the creep rate (Stone and others, 1997). At even higher confining pressures (> 50 MPa), the creep rate may also be affected by pressure melting if the right combination of pressure and temperature are present (Jordaan and others, 1997).

A state variable approach has been used in the past for the constitutive modelling of the damage in and near high pressure zones. Both Xiao and Jordaan (1996) and Singh and Jordaan (1996a, 1996b) have developed models based on this approach, the former for initially intact granular ice, the latter for crushed and sintered ice where extrusion has already occurred. These two models are both based on work by Schapery (Xiao and Jordaan, 1996, Singh and Jordaan, 1996a, 1996b, and references therein) and use this damage formulation to model the development of damage in ice. More recent work by

Jordaan and others (1997) expands on these models and isolates the pressure dependence of the response of ice to creep loads for intact ice. These models will be reviewed below, with the latest model by Jordaan and others (1997) being investigated later in Chapter 5 with respect to its calibration and the effects of damage on the relation.

2.4.2 Modelling and Describing Damage: An Introduction to Damage Mechanics

The field of damage mechanics is a branch of mechanics used by materials science and engineering to describe the reduction in strength of materials subjected to unfavourable mechanical and environmental conditions. Unfavourable conditions can include fatigue or cyclic loading, plastic deformation, creep, relatively high temperatures, and aggressive or inhospitable media. In all cases the end result is often fracture accelerated by the unfavourable conditions or environment.

The changes in the material that result in the loss of strength are of a microstructural nature and are typically, but not always, irreversible. Forms of microstructural change include, but are not limited to: void formation, cracking, dislocation pile ups, and changes in grain size. The mechanisms that make these changes possible are different in various types of materials and depend on the conditions present.

Damage is the general term used to describe this change and is generally quantified using state variables. These can range from simple scalar relations to more complex derivations based on the principles of irreversible thermodynamics. In the simplest case the damage value is a scalar which represents the ratio of a given area of damaged material within a cross section with respect to the total initial area. The density of microcracks and voids is also used instead of the area of damaged material. The damage measure is limited to a range of [0,1] where a value of 0 represents the material in an undamaged state and 1 is a completely fractured material. The formulation for this scalar

damage measure is as follows (based on Kachanov, 1958), where the stress in the material, σ, can be expressed as:

$$\sigma = \frac{P}{A_0} \tag{2.12}$$

where P is the load and A_0 is the initial cross sectional area of the material. The scalar damage measure, S, is then defined as:

$$S = \frac{A}{A_0};\ 0 \le S \le 1 \tag{2.13}$$

where A is the damaged area. The effective stress σ_e acting on the material is then:

$$\sigma_e = \frac{P}{A_0 - A} = \frac{P}{A_0(1-S)} = \frac{\sigma}{1-S} \tag{2.14}$$

and so the elastic modulus of the damaged material, E, is derived from Hooke's law as follows:

$$\varepsilon = \frac{\sigma_e}{E_0} = \frac{\sigma}{E_0(1-S)} = \frac{\sigma}{E} \tag{2.15}$$

and solved as:

$$E = E_0(1-S) \tag{2.16}$$

In this way the scalar measure of damage is used to reduce the elastic (or shear) modulus of the material.

Much work has been done in this field since the early work by Kachanov (1958). Budiansky and O'Connell (1976) have discussed and solved for the effect of microcracking on the elastic modulus in three-dimensions. Horii and Nemat-Naser (1983) have developed a formulation for a two-dimensional, plane strain, compressive stress state. Kachanov (1993) has proposed a three dimensional isotropic solution with random non-interacting cracks. Damage mechanics has been applied to the deformation of polycrystalline ice by Jordaan and McKenna (1988; 1989), and Karr and Choi (1989),

as well as others, and several projects at the Memorial University of Newfoundland's Ocean Engineering Research Centre have been focused on ice and damage over the last decade.

Schapery (1981; 1984; 1988; 1989) developed a continuum damage theory using a generalised J-integral that has been in use at Memorial University for several years (see Singh and Jordaan, 1996a; 1996b; Xiao and Jordaan, 1996). The formulation for the damage measure, S, is of the form:

$$S = \int_0^t f\left(\frac{s}{s_0}\right)^q d\tau \tag{2.17}$$

where s is the differential stress, s_0 is the reference stress, and f is a state variable that initially described the properties of the material at cracks as a function of stress. Thus, S represents the history of the stress state of the material at a given point in time.

This damage formulation was used along with the introduction of the Burgers rheological model by McKenna and others (1989) to describe the mechanical behaviour of freshwater ice. In this work all four components of the model were influenced by the scalar damage measure as defined in Equation 2.18:

$$S = \int_0^t \frac{l}{p}\left(\frac{s}{s_0}\right)^q d\tau \tag{2.18}$$

where p is the hydrostatic pressure, s is the von Mises stress, l and q are constants, and s_0 is the reference stress.

To describe the creep enhancement due to damage, an exponential form was used by Jordaan and McKenna (1989):

$$\dot{e}_{ij}^{c,d} = \frac{s_{ij} e^{(\beta_{c,d} S)}}{\eta_{c,d}(s)} \tag{2.19}$$

where e_{ij} is a component of the strain rate deviator tensor; the effective viscosity, $\eta_{c,d}(s)$,

is a non-linear function of von Mises stress ($\eta_{c,d} = \dot{e}_0^{c,d} / s^{(n^{c,d}-1)}$); indexes c and d denote the permanent viscous component of shear deformation (Maxwell dashpot) and recoverable primary creep component (Kelvin dashpot), respectively; and $\beta_{c,d}$ is a constant, termed the creep enhancement factor.

The approach developed by Singh and Jordaan (1996a, 1996b) was used to describe the constitutive behaviour of crushed ice with a known initial porosity. The model was also based on the Burgers model. This approach was following work by Schapery (1989) on a non-linear generalisation of viscoelastic constitutive equations in integral form

$$e = \int_{0^-}^{t} D(t-\tau)\frac{dF}{d\tau}d\tau \tag{2.20}$$

where D defines the structure of the rheological model, and F is a non-linear function of both stress, σ, and damage, S. This last model, Equation 2.19, requires that each component in the Burgers body be non-linear in the same manner (i.e., η_c must be identical to η_d), while others before it, such as Equation 2.15 did not require this condition.

Other work by the group at Memorial University went on to show the importance of pressure in the model (Xiao, 1991; Stone and others, 1997) and incorporate it into the formulation. Xiao and Jordaan's (1996) formulation proposed two damage measures similar to Equation 2.13 representing the two bodies in the Burgers model. A term, S_c, represented damage in the Maxwell unit while a second term, S_d, represented the damage in the Kelvin unit. The f term in each of these was developed into a function of pressure. The model was calibrated against laboratory tests on ice samples and demonstrated very good agreement with experimental data. It was implemented as a user subroutine in the finite element program ABAQUS. Using this program with user defined material properties, medium-scale indentation tests conducted at Hobson's Choice Ice Island in

1989 were simulated numerically. The numerical simulations of the tests were reported to have fit the experimental data very well (Xiao and others, 1991).

The latest model developed at Memorial University for the response of polycrystalline ice to damage will be reviewed in Section 5.1. The model is also described further in Jordaan and others (1997) and is based on viscoelastic theory. It uses the pressure dependence of the ice to develop a double state variable function for quantifying and incorporating damage. The formulation and calibration of this model will also be discussed further in Chapter 5 where it will be compared with collected data.

Chapter 3

Experimental Program and Procedure

The experimental program outlined below was developed to examine granular ice under conditions that, to the author's knowledge, have not been previously explored in any laboratory. The testing is focused on modelling specific conditions that have been observed and recorded in the field related to high pressure zone conditions, where ice is subjected to both large deformations and large confining pressures. In order to understand and model this behaviour, data will be used to calibrate a constitutive model for the ice and further the general understanding of the ice structure interaction phenomena. A better understanding of the microstructural deformation mechanisms at work in the ice will also be obtained.

3.1 Test Matrix

The triaxial testing for this study was of three types: constant deformation rate tests used to damage ice, constant load tests on undamaged ice, and constant load tests on damaged ice. The second of these, the constant load tests, were performed as part of another study and used to compare results and to calibrate a constitutive model in the past

(Jordaan and others, 1997). The motivation and goals for each set of tests will be summarised and an outline on the testing performed to calibrate the model under investigation will be presented.

3.1.1 Constant Deformation Rate Tests

Initially, in order to add to work initiated by Stone and others (1997), two sets of tests (Tests #1 through 14 in Table 3.1) were performed to investigate and characterise damage in ice from a microstructural point of view. High levels of strain (to 28.8%) and relatively high strain rates (to 10^{-2} s^{-1}) were used. The tests were concentrated in the low strain area as this area was observed as being the zone of highest microstructural change; large strains were also investigated.

3.1.2 Constant Load (or Creep) Tests

A suite of tests performed by the author with other researchers and presented with respect to microstructural change (Meglis and others, 1997), creep response, and modelling (Jordaan and others, 1997) was also used in this study. The tests were creep tests (strictly constant load tests) on polycrystalline ice specimens of the same nature and dimensions as the ice used in the present study. The testing was performed with a constant differential load of 57.7 kN producing an initial stress of 15 MPa on the ice. Confining pressure was varied from 5 to 60 MPa in order to investigate the response of the ice with respect to pressure. Testing was concentrated in the high pressure range as the results seemed to have a fairly large scatter. These tests are shown in Table 3.2 and are designated #15 through 21.

Table 3.1 Constant deformation rate test matrix.

Test #	Damage @ 10^{-4} strain/s	
	Strain	Confinement
1	0.4%†	20 MPa
2	0.8%	20 MPa
3	1.4%	20 MPa
4	2.0%	20 MPa
5	4.0%	20 MPa
6	12.8%†	20 MPa
7	28.8%‡	20 MPa

Test #	Damage @ 10^{-2} strain/s	
	Strain	Confinement
8	0.4%‡	20 MPa
9	0.7%	20 MPa
10	1.0%	20 MPa
11	2.0%†	20 MPa
12	4.0%†	20 MPa
13	12.8%†	20 MPa
14	28.8%‡	20 MPa

† Tests performed twice.
‡ Tests performed several times.

Table 3.2 Constant load (or creep) test matrix.

Test #	Differential Stress	Confining Pressure	Strain End Levels (%)
15	15 MPa	5 MPa	4†,10,22,44
16	15 MPa	15 MPa	8
17	15 MPa	30 MPa	44†
18	15 MPa	40 MPa	44
19	15 MPa	45 MPa	48
20	15 MPa	50 MPa	10, 16, 30, 44, 50†, 48
21	15 MPa	60 MPa	44

† Tests performed twice.

Table 3.3 Constant load on damaged ice test matrix.

Test #	Damage @ 10^{-2} strain/s		Creep Step		
	Strain	Confinement	Differential	Confinement	End level
22	12.8%	20 MPa	15 MPa	15 MPa	44.0%
23	12.8%	20 MPa	15 MPa	30 MPa	44.0%
24	12.8%	20 MPa	15 MPa	50 MPa	44.0%

	Damage @ 10^{-4} strain/s		Creep Step		
	Strain	Confinement	Differential	Confinement	End level
25	12.8%	20 MPa	15 MPa	15 MPa	44.0%
26	12.8%	20 MPa	15 MPa	30 MPa	44.0%
27	12.8%	20 MPa	15 MPa	50 MPa	44.0%

3.1.3 Constant Load Tests on Damaged Ice

The third set of tests was performed to quantify the creep response of ice previously subjected to high strain levels and high strain rates and to more closely model conditions within high pressure zones. It is explained by Stone and others (1997) that the nature of the ice damaged to 2 and 4% strain is such that the ice behaves similarly when reloaded under moderate confinement after damage, however highly damaged ice and its response to load was not addressed.

In these tests (Tests #22 through 27 in Table 3.3) the confining pressure was changed after the damage step to 12.8% strain in order to achieve a more realistic creep test on damaged ice at pressure levels expected within and around high pressure zones. The confining pressure levels were set at 15, 30, and 50 MPa, and are compared with undamaged specimens previously tested at these same levels (Jordaan and others, 1997, NEB, 1997). The 12.8% damage level was selected arbitrarily and does not represent any specific damage level (as possibly described and quantified by subsequent damage formulations). This was part of the ongoing efforts to investigate the pressure dependence of the strain rate in the ice and to verify the validity of coefficients obtained for the constitutive relation of the proposed model in Jordaan and others (1997).

3.2 Sample Preparation

Large blocks of mostly monocrystalline freshwater ice were moulded from templates using distilled and deaerated water. The blocks were cut into manageable sizes, crushed, and the ice sieved between 2.00 mm and 3.36 mm sized mesh. Templates were cut from the tops of the monocrystalline blocks and retained for the next batch. The resulting crushed and sieved ice was placed into a cylindrical acrylic mould, 300 mm tall by 240 mm in diameter closed at the top using a thin latex membrane sealed with silicone grease

and held in place with several large rubber bands. The seal between the latex and the acrylic mould was ensured with silicon high vacuum grease. The base of the mould was constructed from aluminium to enhance the heat transfer of the mould from the bottom and to help induce unidirectional freezing. The mould was evacuated with a vacuum system for over an hour and flooded with distilled and deaerated water at a temperature of 0°C while still under vacuum. The ice-water mixture was then placed into a cold room at -10°C and allowed to freeze slowly and unidirectionally upward over several days. A schematic of the vacuum system is shown in Figure 3.1.

The unidirectional freezing of the mould was accomplished by covering the mould with an insulated jacket which left the aluminium bottom of the mould exposed to the air in the cold room. The unidirectional freezing served the purpose of allowing trapped air that was not removed in the deaerators to be pushed ahead of the ice-water interface, allowing a relatively clear bubble free ice block from which samples were cut.

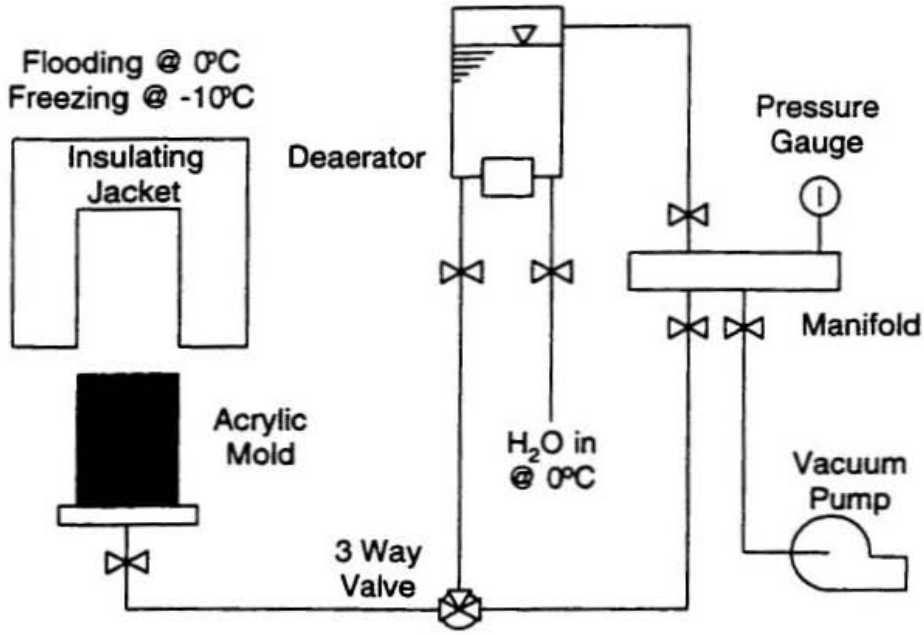

Figure 3.1 Schematic of the vacuum system used in preparing seed ice and distilled water for moulding.

Once the block was completely frozen, it was removed from the mould by warming the surface slightly in an anteroom at 0°C. The warming caused a slight amount of melting at the outer surface, releasing the block from the mould. The blocks typically had bubbles frozen into the top surface. These were avoided when the specimens were cut and machined.

Specimens were cut from the cylinder by quartering the block once both the top and bottom of the cylinder had been cut clean of bubbles (if any were present). Four cylindrical samples of 155±0.2 mm length and 70±0.05 mm diameter were machined from each granular ice block using a lathe. Blocks of ice directly adjacent to the ends of the cylinders were saved for later thin section analysis of the virgin material. Samples were stored at a temperature of -15°C or lower, wrapped in towels and in air tight freezer bags until ready for use.

3.3 Testing Apparatus and Procedure

Prepared samples were allowed to equilibrate for several hours at -10°C prior to being tested with a Materials Testing Systems (MTS) test frame located in a cold room (Figure 3.2). Testing has shown that the sample required only several hours to equilibrate from storage temperatures of below -20°C. For each test the samples were mounted on hardened steel end platens, 70 mm in diameter, and enclosed in a latex jacket to exclude the silicone oil confining fluid. Specimens were then placed inside the triaxial confining cell and, in some cases, two linear variable differential transformers (LVDT's) were mounted to the specimen using collars. For tests to high end-levels of strain, the LVDT's were not used as lateral strain within the specimens would distort the LVDT readings. The confining cell was then closed and filled with silicone oil using a pneumatic pump system incorporated into the pressure intensifier system.

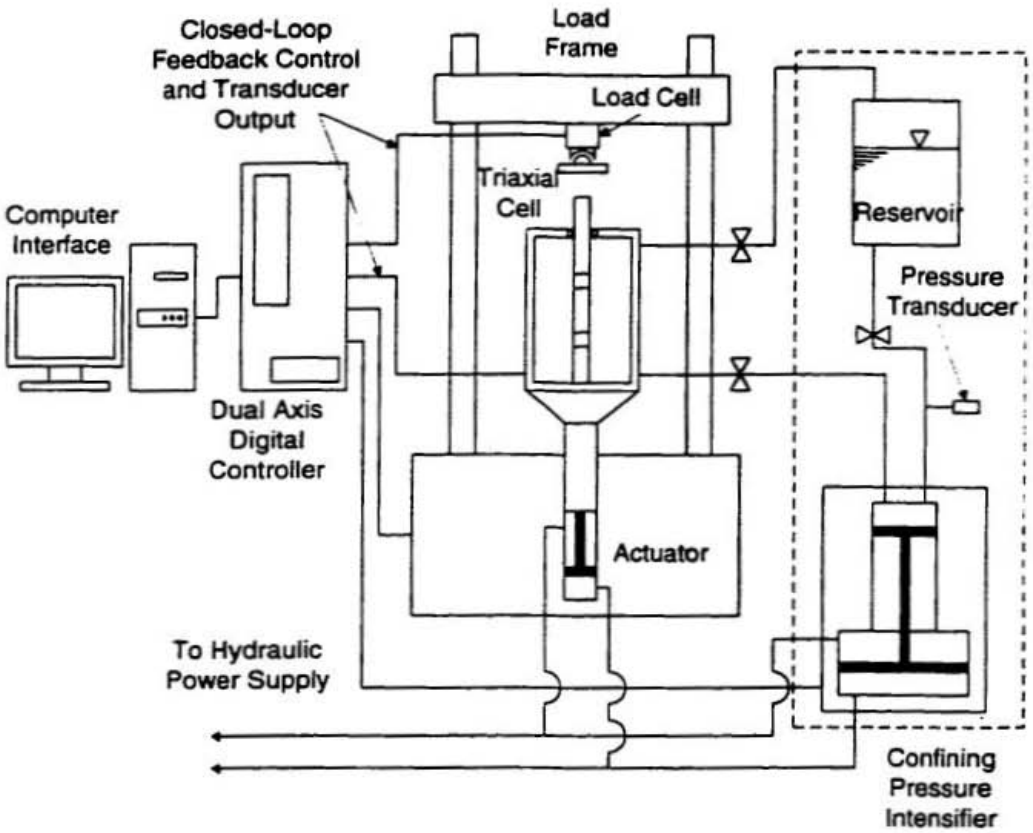

Figure 3.2 Schematic of MTS test frame, pressure intensifying unit, and computer interface.

The MTS test system consisted of two servo-controlled hydraulic rams which applied axial load and confining pressure independently. The rams were controlled using MTS's Test Star II software, run on an OS/2-based 486 computer. The software also performed the data acquisition for each test. In general, between seven and nine test parameters were monitored, including axial load, confining pressure, displacement and temperature. Later in the test program, with the use of calculated feedback in the system, stress and strain were monitored instantly and could be observed as the test progressed.

Once the cell was closed and sealed, a small axial load was applied to the sample at ambient pressure to ensure contact between the specimen and piston. This was done in

order to prevent a problem encountered in earlier test series in which the system would search for loads in the wrong direction. The small applied load was believed not to have had a significant effect on the samples as the control mode was changed from load to stroke as soon as contact was made, holding the stroke of the ram constant instead of the small applied load. The load was typically about 0.3 kN, a small fraction of the load applied during testing.

With the sample in place, the confining pressure was then increased slowly to the prescribed level. All damage (constant strain rate) steps were performed at a confining pressure of 20 MPa and a cold room temperature of about -10°C. Later in the creep part of the tests the confining pressure was varied for the duration of the creep load. In the samples subjected to low strains, LVDT's were used to monitor axial displacement and control the strain rate. In the tests without LVDT's, the displacement of the ram was used to compute strain and control the strain rate.

The tests conducted were strictly constant stroke rate tests. This came as a result of controlling the stroke rate rather than the actual strain rate. As a result of this the strain rate increases as the specimens are deformed and larger amounts of strain are applied for the same amount of stroke. This difference increases the strain rate by 33% in a test to 28.8% strain (at both strain rates) and a proportional amount of strain rate throughout other tests at lower strain levels. This effect is discussed in greater detail in the next section.

At the end of each test the axial load was quickly removed (but not so quickly as to cause cracking due to a rapid drop in pressure) and the confining pressure reduced to ambient pressure. The sample was removed from the cell immediately after testing and inspected for evidence of jacket leaks and fracture. When immediate thin sectioning was not possible the sample was stored at -30°C until thin sections could be prepared.

3.4 Corrections to Collected Data

In this work the true corrected stress will be simply referred to as the 'stress' while uncorrected stress (or stress from raw data) will be identified as such. This point is explained below as the reasons for the corrections are introduced.

Lateral strain was observed in all tests to high strain levels. The effect of this strain on the true stress in the sample was taken into account when plotting and analysing the data as the cross sectional area of the sample increased with shortening. A correction was performed on the data based on the assumption that the volume of the specimen remained constant and that the small amount of lateral strain in the sample was uniform in order to simplify the calculation of true stress. The initial volume of the specimen was used to calculate the cross sectional area at the centre of the sample throughout the duration of the test using stroke data. The areas used in the calculation correlate well to diameters measured from thin sections after testing.

Initially, the samples measured 70 mm in diameter and 155 mm in length. The simplified assumption is made that no change in volume occurred during the test (i.e. no voids are formed and cracks remain essentially closed). Also the samples were idealised as expanding uniformly in cross section over the entire length. This means that the diameter can be calculated at any time as long as the length is known. In fact the lateral strain was not uniform and samples ended up with a slight 'barrelled' shape, especially near the platens, while a relatively uniform section made up the middle of the sample. The samples also extruded beyond the platens leading to slight errors in the constant volume assumption.

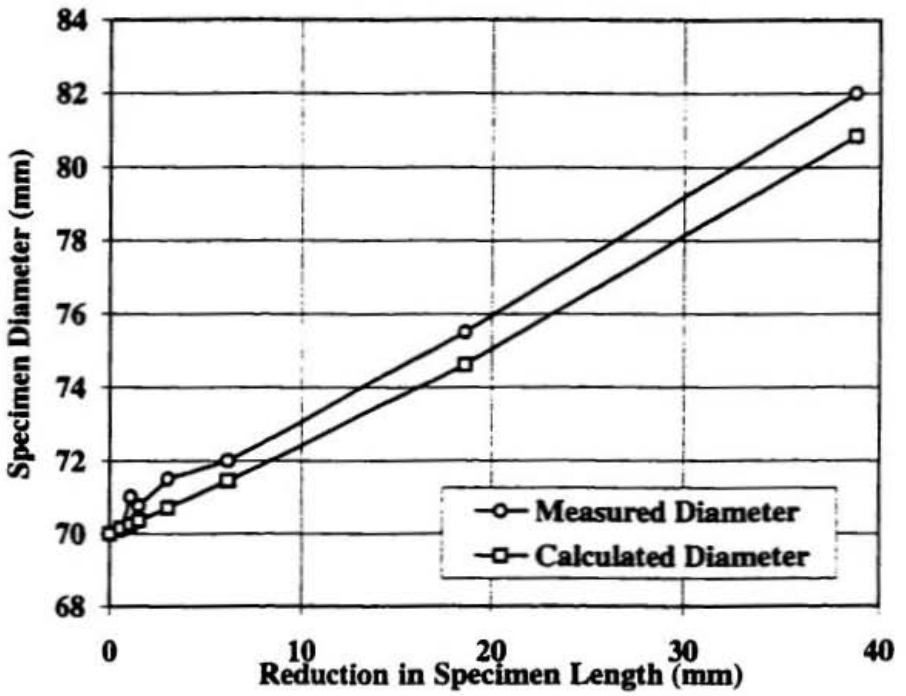

Figure 3.3 Plot of calculated and actual diameters versus reduction in length of ice specimen.

Assumptions and calculations for the diameter agree very well with values obtained from measurements on samples following tests. For this reason the constant volume correction was used through out the testing. The relation of the constant volume assumption and actual data is compared in Figure 3.3 which plots calculated and measured diameters for different strain levels.

3.5 Post Test Analysis

Thin sections were generally prepared within 24 hours of testing. Sections were made both parallel and perpendicular to the cylinder axis, depending on specific tests and areas of interest. To preserve the microstructure sections were not melted onto a glass plate but

were welded to the plate using a thin bead of distilled water around the perimeter of the specimen. This had only minimal effect on the grain structure, sacrificing the outer 2 mm of the section.

Thin sections were prepared by cutting a thin slice from the sample using a band saw. The disk was mounted on a glass slide with the side to be observed facing upwards. A microtome was then used to polish the top surface of the ice. This surface was then mounted on a clean scratch free glass plate and welded into place. The two plates, forming a sandwich with the ice, were cut apart using the band saw leaving most of the ice on the first plate and a few millimetres of ice on the plate with the polished surface. The ice on the second plate could then be microtomed down to a thickness of 0.5±0.05 mm.

Thin sections were photographed several times at different magnifications as well as under different lighting conditions. The different lighting conditions were: a) under crossed polarised light without side lighting, b) under cross polarised light with side lighting, and c) with side lighting only. The three modes of lighting were used to highlight individual microstructural characteristics of each individual thin section. Viewed simply through crossed polarising filters, a clear picture of the grains, their boundaries, and their colour (indicating the orientation of the c-axis), are clearly visible. With only regular (unpolarised) white light used to illuminate the thin sections, cracks, bubbles, and voids can be observed without reference to the grain structure. If side lighting is used along with the crossed polarising filters, any cracks and voids can be viewed together with an image of the grains and their boundaries, showing how the two may be related. This technique of photography was being developed as the testing progressed, so not all tests were photographed in all three modes.

Analysis of the amount of cracking being qualitative at this point, no measurements of crack density were performed on the sections. It should be noted that a few long parallel crack several centimetres long can be seen in some thin sections, however these are due to the thin sectioning process and can easily be discerned from cracks related to testing.

Average grain size was determined from photographs of thin sections using the mean intercept length method outlined in Deiter (1976). In this method the number of grains intercepted by a test line is counted and then divided by the total length of the line. This method generally underestimates the true diameter of equiaxed grains. It is, however, a straightforward method for determining relative differences in average grain size. Grain size measurements were made using thin sections cut normal to the sample axis. An average of three measurements was taken for each thin section photograph.

Data from the tests was plotted and analysed using Matlab 4.2a. Matlab proved convenient as data sets were often very large with multiple columns of data depending on the type of test. Typically, several plots were prepared from each test and placed into a database along with other vital information from each test.

Chapter 4

Results of Triaxial Testing

The results of all triaxial testing associated with the study are presented in this chapter. Thin section photographs from tested ice samples are shown and represent the microstructure of the deformed ice. An extensive set of curves showing stress and strain responses of the ice are also shown.

The testing, as described in Section 3.1, can be divided into three types of testing. These are: constant deformation rate (or damage) tests, constant load (or creep) tests, and constant load tests on ice damaged at constant deformation rate. In all cases the damage was performed under 20 MPa of confinement. All testing was done at a temperature of about -10°C, however there were slight fluctuations which will be discussed.

4.1 Characterisation of Virgin Ice Samples

Photographs of thin sections from several untested (virgin) ice specimen were taken for comparison with the damaged ice. The average grain size for virgin specimens of the granular ice tested was 2.38 mm. No obvious preferred c-axis orientation was visible in the grain matrix, and only a few small air bubbles were observed. The undamaged ice

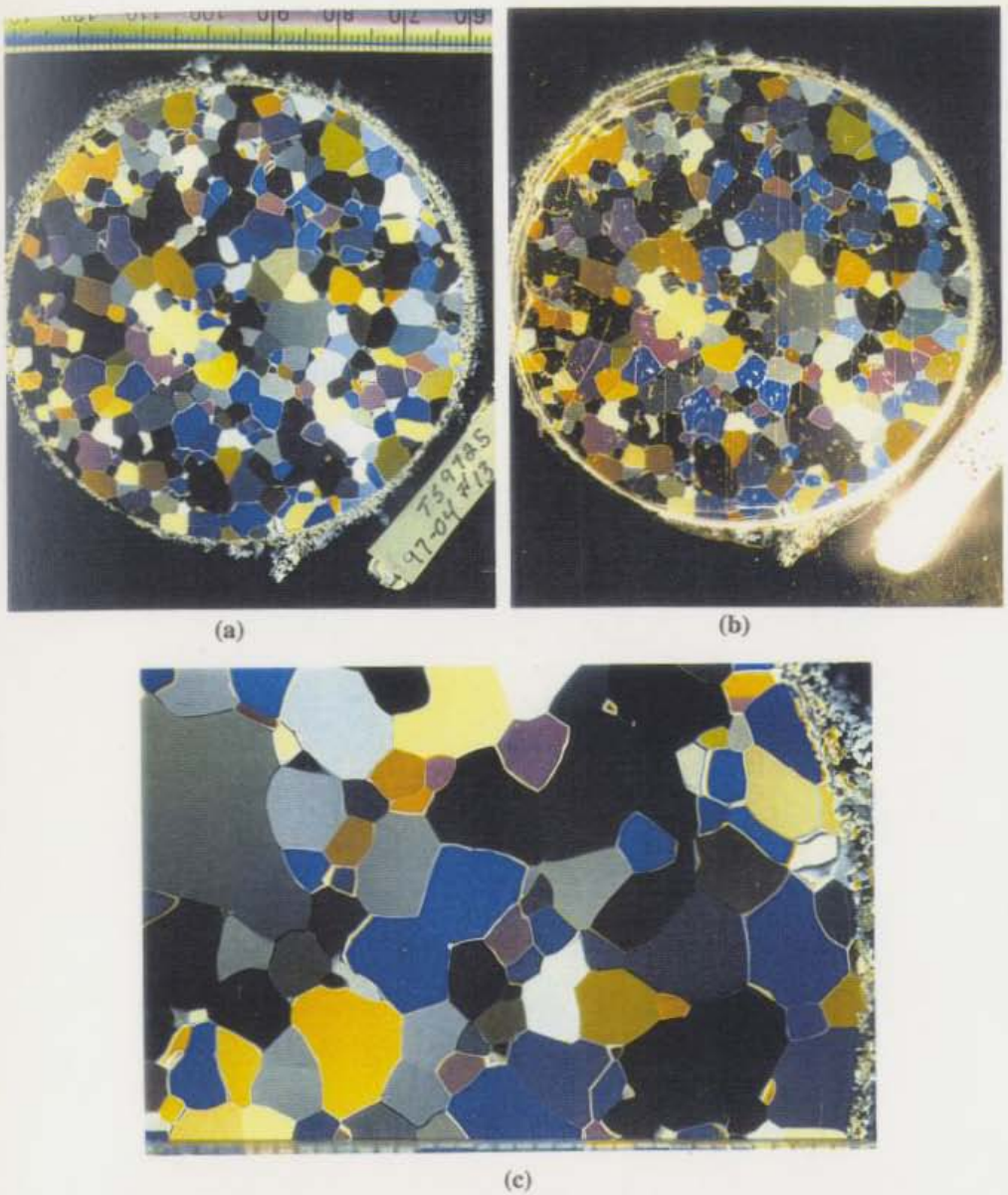

Figure 4.1 Thin section photographs of virgin granular ice sample viewed between crossed polarising filters, with side lighting, and close up.

showed no microfracturing as a result of grain growth, thermal effects, or the thin sectioning process. Figure 4.1 shows a thin section taken from a typical undeformed sample of the freshwater granular ice used in this study. Note that all scales in the thin section photographs are in millimetres.

4.2 Constant Deformation Rate Tests

4.2.1 Stress versus Strain Curves and Peak Stress

Stress-strain curves for several tests performed at a nominal strain rate of 10^{-2} s^{-1} and a confining pressure of 20 MPa are shown in Figure 4.2. A similar set of curves is shown in Figure 4.3 for tests at the lower strain rate of 10^{-4} s^{-1}. These curves show a

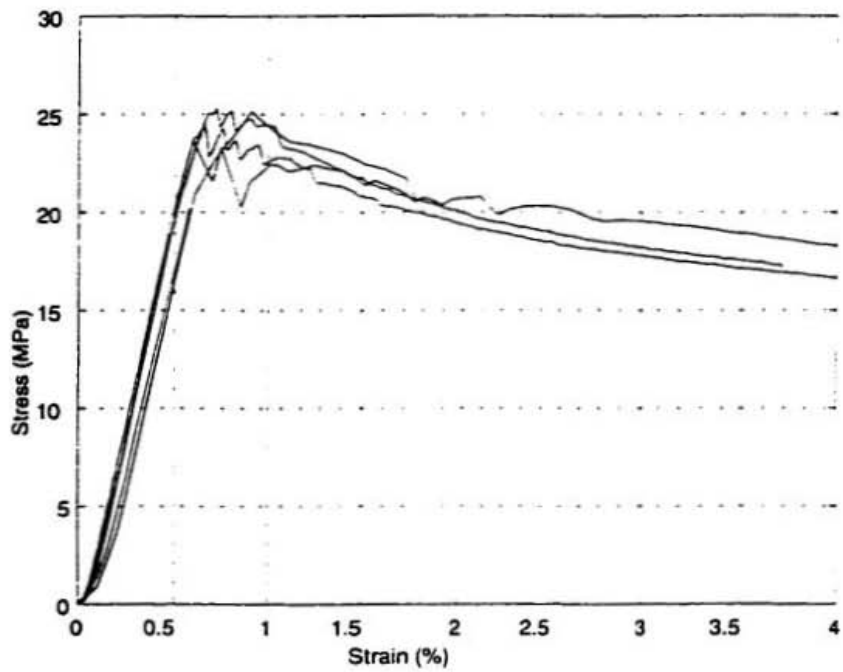

Figure 4.2a Stress-strain curve for tests at a strain rate of 10^{-2} s^{-1} from 0 to 4% strain.

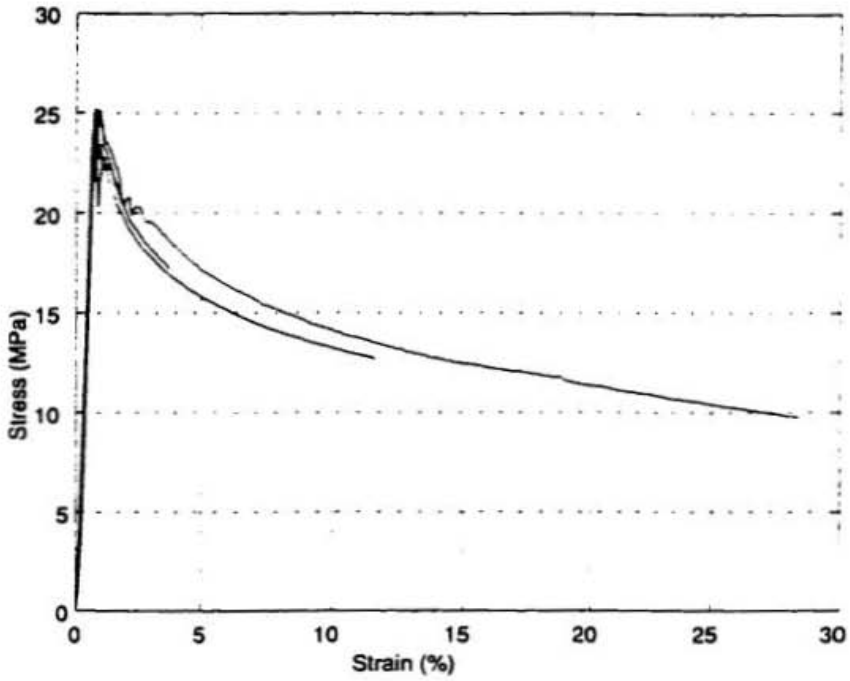

Figure 4.2b Stress-strain curve for tests at a strain rate of 10^{-2} s^{-1} from 0 to 30% strain.

representative selection of results. The stress-strain curves for the remaining tests at these strain rates were similar in both shape and peak stress. The similarities between the curves indicates the reproducibility of the tests.

At the lower strain rate (10^{-4} s^{-1}) the average peak stress was 9.3 MPa. The stress in the samples tested at the higher strain rate (10^{-2} s^{-1}) peaked at a much higher level, 23.4 MPa on average. In the low strain rate tests the curve was smooth with very little noise. In the higher strain rate tests a jagged curve was observed (Figure 4.2). The peak stresses were consistent with results from other researchers (Jones, 1982) and occurred between 0.8 and 1.2 % strain in all tests.

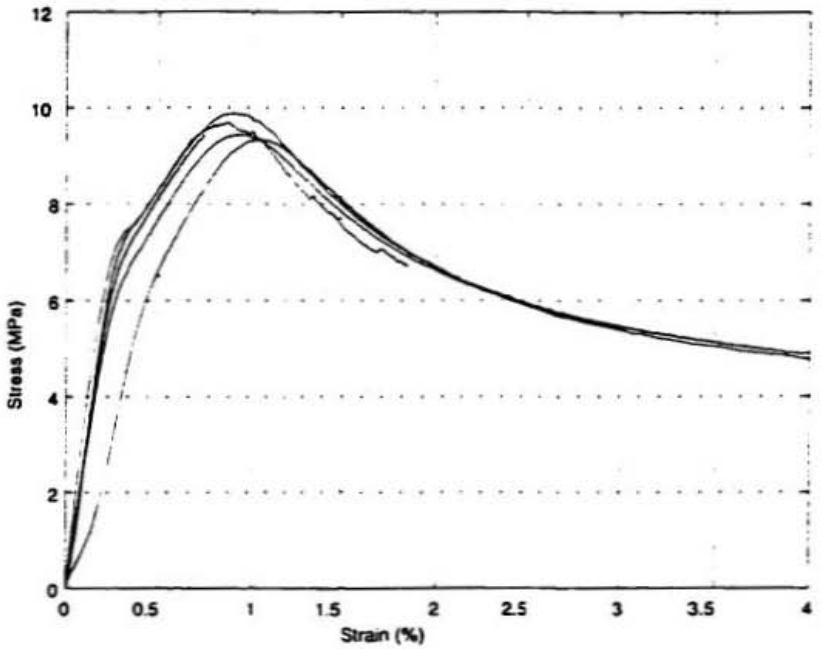

Figure 4.3a Stress-strain curve for tests at a strain rate of 10^{-4} s^{-1} from 0 to 4% strain.

4.2.2 Grain Size, Distribution, and C-axis Orientation

Thin sections of test specimens in Figures 4.4 and 4.5 show both a photograph of the section between crossed polarising filters (left side) and a photograph with side lighting to highlight cracks and voids (right side). The photographs show the microstructure within the samples at several different strain levels, up to the maximum strain of 28.8%.

Grain size measurements of the thin sections show a general decrease in the average grain size with increasing strain for both high and low strain rate tests. At a strain of 4% the average grain size dropped significantly to less than 1 mm. The grain size then continued to decrease to values of 0.72 mm for 10^{-2} s^{-1} and 0.89 mm for 10^{-4} s^{-1} at 28.8% strain. The grain size values measured from the thin sections are shown in Table 4.1 It

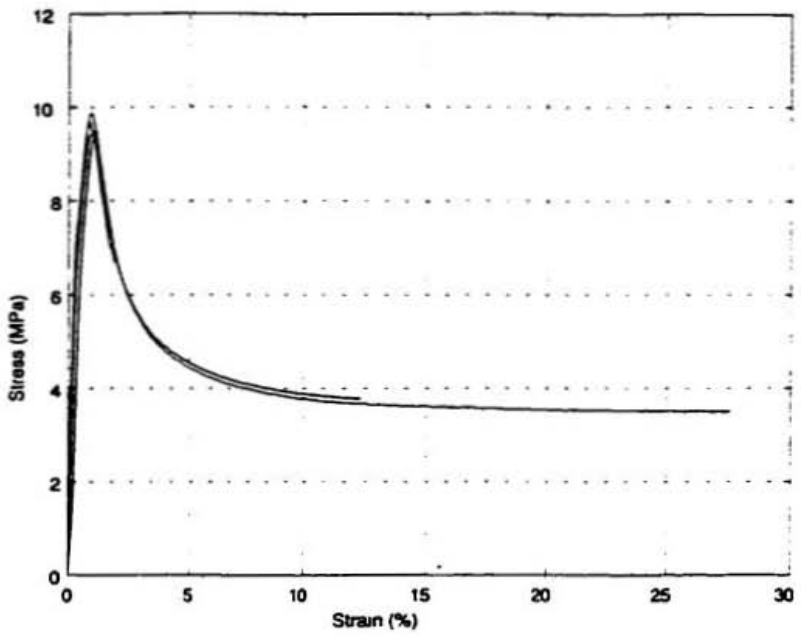

Figure 4.3b Stress-strain curve for tests at a strain rate of 10^{-4} s^{-1} from 0 to 30% strain.

should be noted that numbers from the table are based on only a limited number of tests in some cases. The tests that were repeated show the standard deviation to be typically within 0.28 mm/gr. This value leads to some overlapping in the results of the grain size measurements at the higher strains. In general grain size reduction seemed more apparent in the 10^{-2} s^{-1} strain rate tests than in tests at 10^{-4} s^{-1}. This can be seen in the thin section photographs, Figures 4.4 and 4.5. All grain size values are plotted against the total strain in Figure 4.6.

Figure 4.4 **(On following two pages)** Thin section photographs of samples tested at a strain rate of 10^{-2} s^{-1} viewed between crossed polarising filters and with either side light added or with side light only.

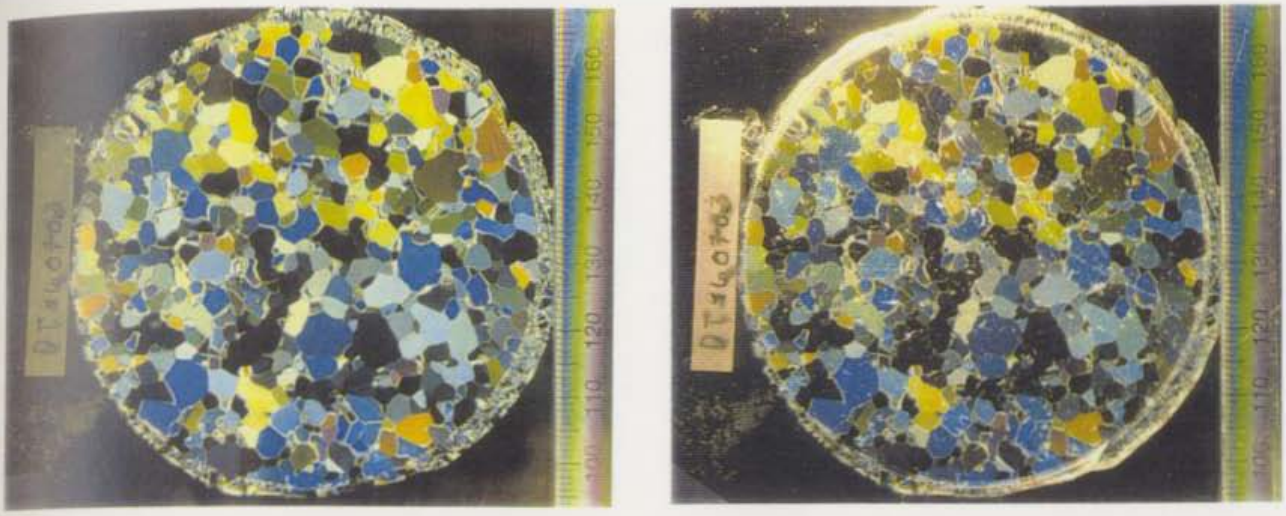

(a) 0.4% @ 10^{-2} s^{-1}

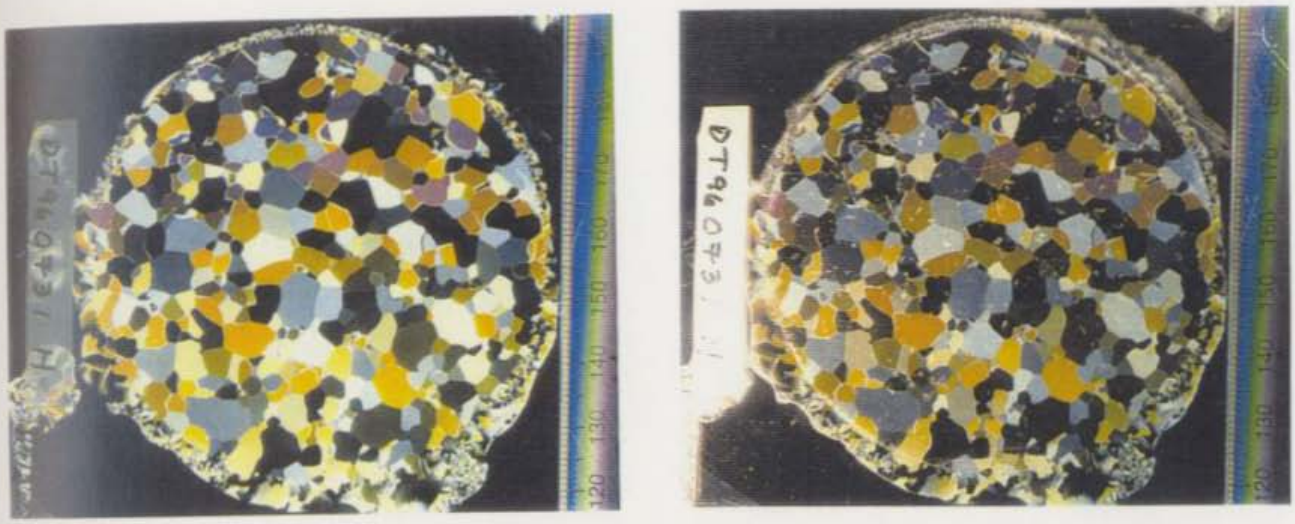

(b) 1.0% @ 10^{-2} s^{-1}

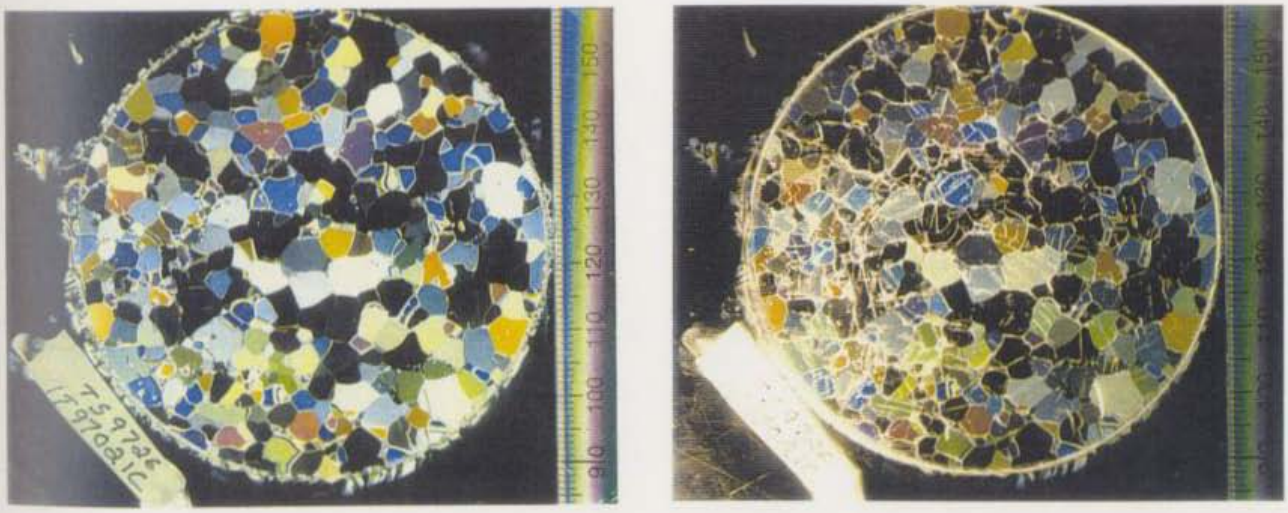

(c) 2.0% @ 10^{-2} s^{-1}

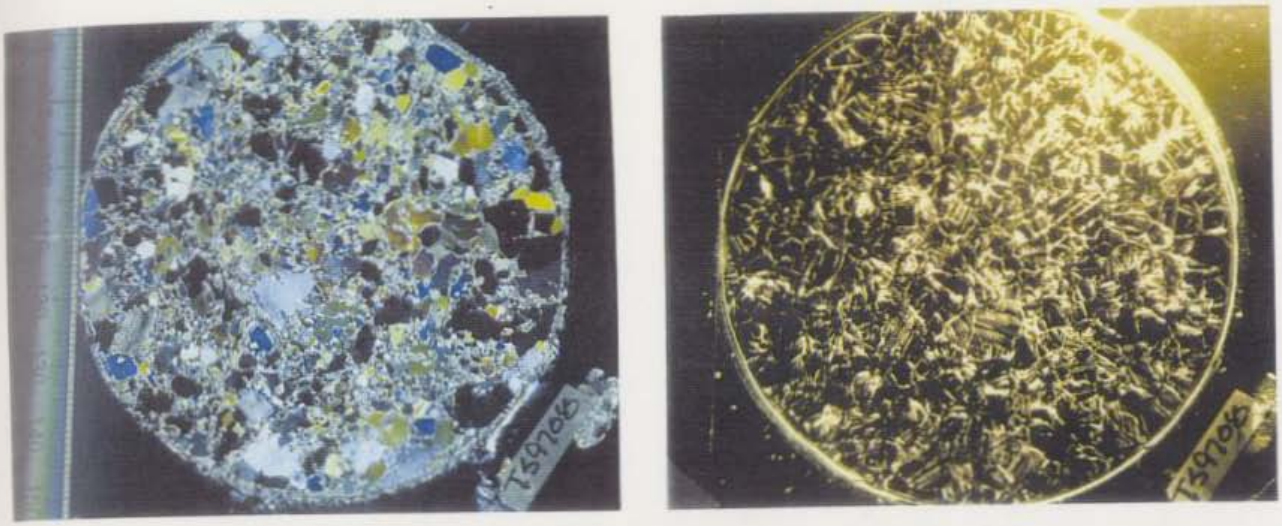

(d) 4.0% @ 10^{-2} s^{-1}

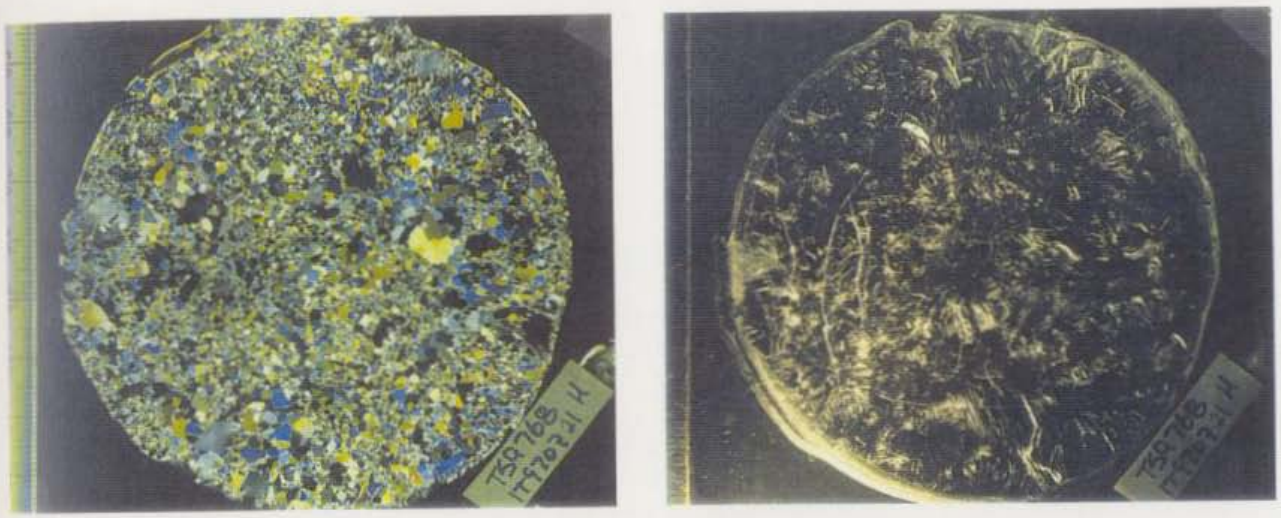

(e) 12.8% @ 10^{-2} s^{-1}

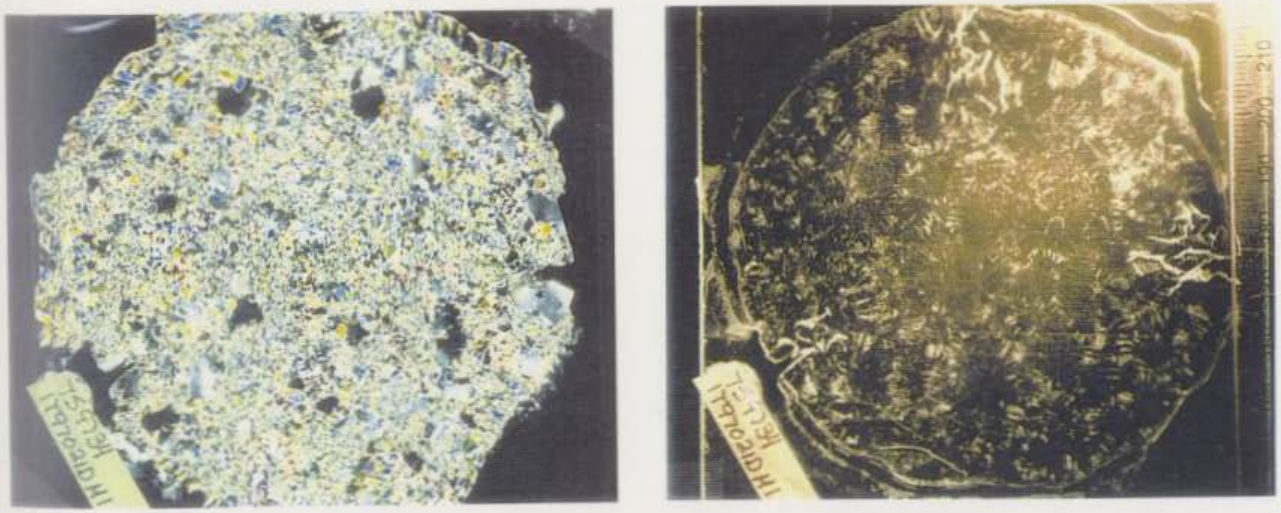

(f) 28.8% @ 10^{-2} s^{-1}

Table 4.1 Final grain size of constant deformation rate specimens.

Grain Size (mm/gr.)		Total Strain (%)								
		0.4	0.7	0.8	1.0	1.4	2.0	4.1	12.8	28.8
Deformation Rate	10^{-2} s^{-1}	2.70	2.43	--	2.44	--	3.04	0.82	0.70	0.72
	10^{-4} s^{-1}	2.54	--	2.53	2.62	1.98	1.50	1.08	1.05	0.89

There has been work presented by Jacka and Li (1994) which describes a steady state crystal size in ice that is dependent on an equilibrium between stress or deformation and temperature. This work does not readily apply to the present study as deformation rates are significantly higher than those considered by Jacka and Li (1994). The fact that grain size was dropping towards a steady value in both sets of tests may indicate that there is a stress dependence, since stress also appeared to be approaching a steady value. In this case the dependence on stress can also be related to deformation rate as stress in the sample was a function of applied deformation rate.

In the specimens subjected to strains greater than 1%, the grain size distribution appeared to become bi-modal, with a few relatively large grains (greater than 5 mm diameter) surviving as remnants within a matrix of very fine grains (less than 1 mm diameter). Figures 4.4d, e, and f, and 4.5d, e, and f show examples of this texture within the ice. Quantitative analysis of grain size distribution has not been undertaken at this point, but some observations regarding general grain orientation will be discussed.

Figure 4.5 **(On following two pages)** Thin section photographs of samples tested at a strain rate of 10^{-4} s^{-1} viewed between crossed polarising filters and with either side light added or with side light only.

(a) 0.4% @ 10^{-4} s^{-1}

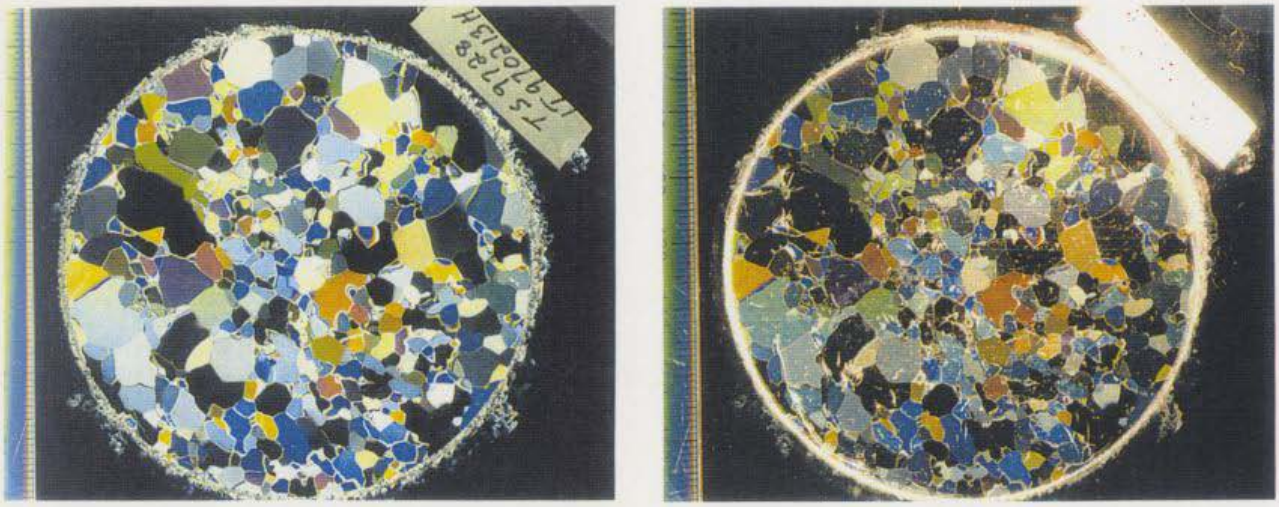

(b) 1.0% @ 10^{-4} s^{-1}

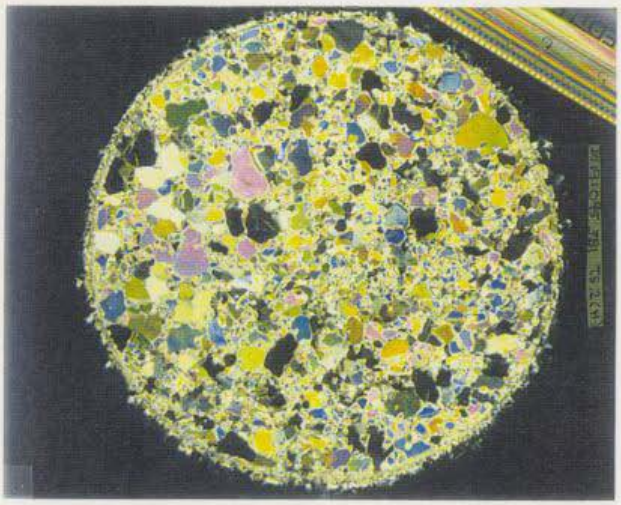

(c) 2.0% @ 10^{-4} s^{-1}

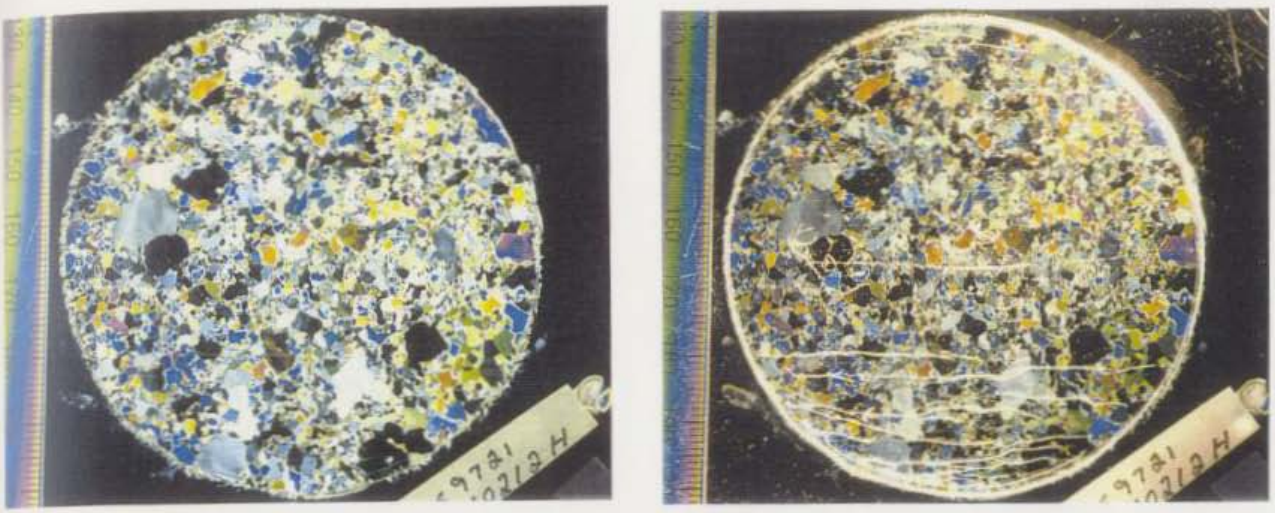

(d) 4.0% @ 10^{-4} s^{-1}

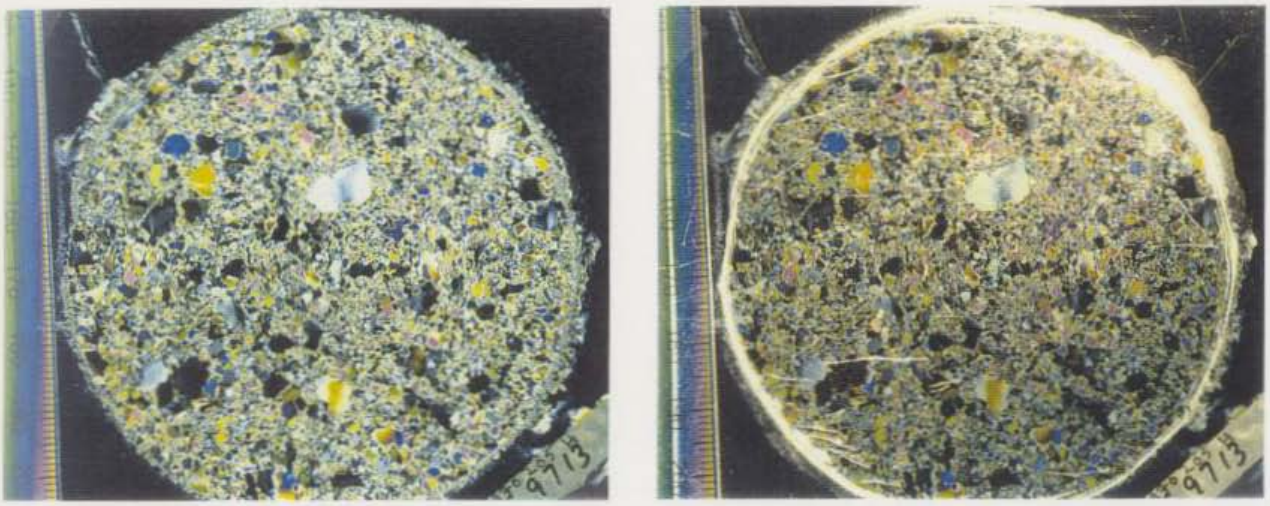

(e) 12.8% @ 10^{-4} s^{-1}

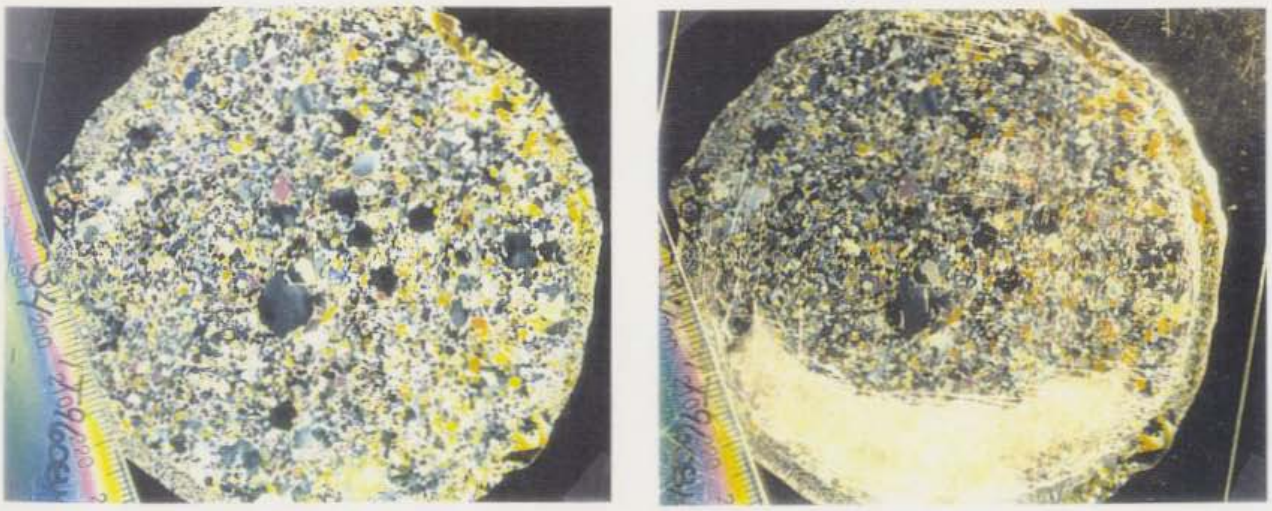

(f) 28.8% @ 10^{-4} s^{-1}

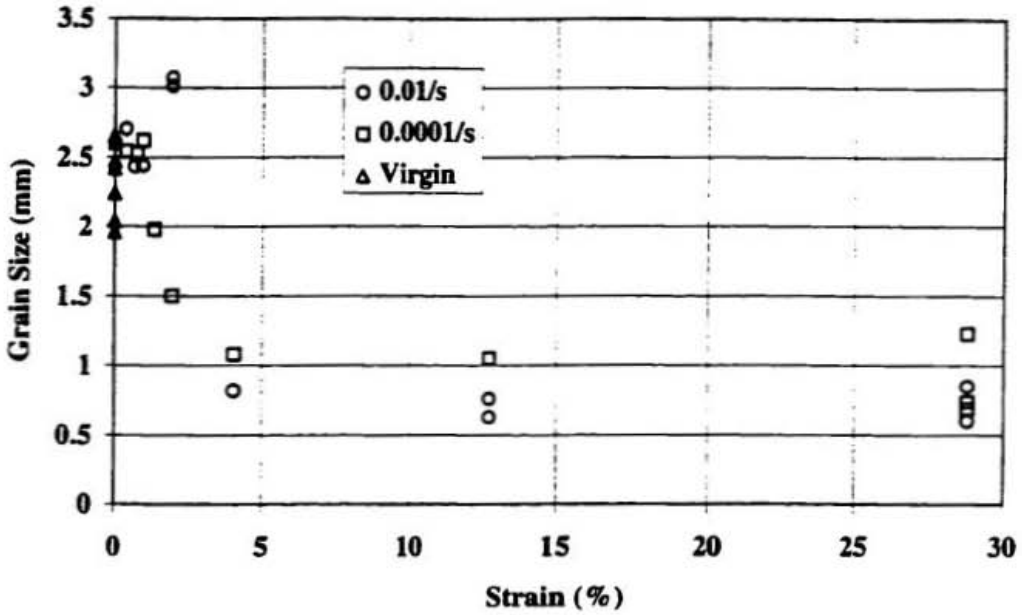

Figure 4.6 Grain size plotted versus total strain for all tests performed at constant deformation rate.

The large remnant grains in the damaged ice had a c-axis orientation that was very near parallel to the axis of deformation. This was determined by rotating thin sections while viewing them between crossed polarising filters. As grains were rotated, those with a c-axis orientation in the direction perpendicular to the plane of the thin section (i.e., vertical and parallel to the axis of deformation) remained black or dark. The remnant grains in the thin sections had little change in colour from black and dark grey. The orientation of the crystals in the preferred orientation grains is believed to be such that they were resistant to shear stresses within the material, especially at lower strains. Defined another way, the c-axis was oriented parallel to the major principle stress. This would allow other grains within the sample with a c-axis orientation nearer the principle shear direction to accommodate the deformations. Once this process began, it seems logical that large amounts of strain energy would have been dissipated in the rest of the

sample in the form of recrystallisation and microcracks, especially in planes of shear stress. This would have allowed these preferred orientation grains to maintain their general size and orientation, even though adjacent grains were being deformed and consumed by microcracking and recrystallisation.

It is also possible that grains with a c-axis orientation perpendicular to the axis of deformation would also have survived. A few cases were observed where the thin sections showed grains with a c-axis that was parallel to the horizontal and perpendicular to the axial of deformation. This was indicated by the colour of the grains changing from white to black at 90 degree intervals as the thin section was rotated (Barrette, 1997). These grains would also have survived by being oriented with the principle stress state.

4.2.3 Microcracking and Recrystallisation

Extensive grain boundary cracking occurred in the samples tested at the high strain rate up to 4.0% strain (Figure 4.4d). Fewer cracks were seen in samples tested at the lower strain rate, but there was still some cracking visible, as the thin section photographs of the test to 1.0% strain show (Figure 4.5b). These microcracks were primarily along grain boundaries and generally occurred during the first few percent of shortening. While most of the grain boundary cracks probably formed as a result of loading the ice, some may also have formed in response to the release of the confining pressure at the end of the test. This is discussed further in Meglis and others (1998) with respect to pressure reduction tests. A pressure reduction test is typically a constant load test where the applied confining pressure is dropped while maintaining the axial load. This is an alternative way of applying a load to a sample and has been shown to cause a large increases in deformation rate for a relatively small increase in differential stress (Stone and others, 1997).

Grain boundary cracks were also visible at low strains but were not observed as deformations continued to higher strains. The samples deformed to 28.8% (Figure 4.4f) showed that the grain boundary cracks were no longer visible. Parallel sets of intragranular cracks could be seen in the thin section photographs and associated with specific regions of microstructural damage in both views.

Almost no cracking and little recrystallisation or restructuring of the microstructure was observed in the samples before the peak stress, as shown in Figures 4.4b and c. For strains greater than about 2% at 10^{-2} s^{-1}, microcracks began to appear within individual grains as clusters of densely spaced parallel cracks or crack banding. These cracks, although typically parallel to each other within individual grains, did not have any obvious preferred orientation in the horizontal plane (Figure 4.4). The cracks may have been an indication the orientation of the basal plane within grains. The intragranular cracks did not appear in tests deformed at the lower strain rate.

The larger remnant grains showed little internal cracking in samples deformed at both strain rates. In the high strain rate tests, the fine grained material viewed between crossed polarising filters corresponds with the areas of dense fractures and restructuring visible in the side lit photographs (Figure 4.4e and f). In contrast, the fine-grained material in the low strain rate tests was significantly less fractured (Figure 4.5e and f) and showed much less cracking beyond 4% strain.

Recrystallisation appears to have been evident in the thin sections of the high strain level tests. The distribution of the grains in the thin section, with few large grains remaining in a matrix of small grains is indicative what has been characterised as recrystallisation in ice (Stone and others, 1997). This restructuring mechanism seems to begin at the peak stress, as there is no observable grain size reduction before this point (from test start to about 1%). The recrystallisation also seems to be acting in conjunction

with the intragranular microcracking occurring within grains, consuming the cracks and forming new smaller grains. This is similar to a mechanism described in Poirier (1985) as rotation recrystallisation where the progressive misorientation of subgrain results in the formation of new, smaller grains. The fragmenting mechanism in Poirier (1985) is creep polygonization, whereas in the ice it seems to be microfracture and crack banding as described above.

In general the constant strain rate testing showed a change from brittle to ductile behaviour as strains increased. Thin section photographs of ice samples show a progression from grain boundary cracking to intragranular cracking to dynamic recrystallisation. Low strain rate tests (10^{-4} s^{-1}) do not show extensive intragranular cracking although the end result, a decrease in grain size, is apparent in all tests at both strain rates. In summary it can be said that the effects of damage is to induce cracking at low strains and to reduce the grain size at high strains.

4.3 Review of Constant Load Tests

A series of constant load creep tests were used in this study for comparison with constant load tests on damaged ice. The tests were part of a study presented by Meglis and others (1998) in which the author took part. A review of microstructural and mechanical results from this set of testing is presented, drawing comparisons between it and the previous set of constant strain rate tests. The test set is composed of constant load tests performed on granular ice subjected to an applied confining pressure. The confining pressure in these tests was varied from 5 to 60 MPa while the deviatoric stress was maintained at a constant s = 15 MPa.

4.3.1 Microcracking and Recrystallisation

Similarly to tests at constant strain rate, microcracking in the samples was of two types, namely intragranular and intergranular. The development of the microstructural change is shown in Figure 4.7 and Figure 4.8 for pressures p_c = 5 and 50 MPa, respectively. More thin section photographs are shown in Figures 4.9 and 4.10 for tests performed at 30 and 40 MPa confinement.

In triaxial testing under low confinement (p_c = 5 MPa) the ice developed a high density of microcracks in the first few percent of shortening (Figure 4.7a). The grain boundary cracking was distributed throughout the samples and outlined grains where intragranular cracking had taken place. Generally most grains remained complete over the first interval of strain (up to 4%), with the exception of internal cracking. Some small localised areas on grain boundaries were severely damaged and showed early signs of recrystallisation. These areas were composed of fine grained ice that could be associated with high crack densities in the thin section photographs illuminated with side lighting. The intragranular cracking was composed of sets of parallel cracks similar to those observed in the constant strain rate tests. Vertical thin sections from Meglis and others (1998) showed that the intragranular cracking did not have a preferred orientation in the vertical axis. In all cases, as shortening progressed, the cracks tended to be healed or consumed. At the maximum deformation of about 44% strain very few original grains remained intact and thin sections of the samples were composed mostly of small grains with little cracking.

Figure 4.7 **(On following page)** Thin section photographs of samples tested at a constant stress of 15 MPa and 5 MPa confinement viewed between crossed polarising filters and with side lighting (from Meglis and others, 1998).

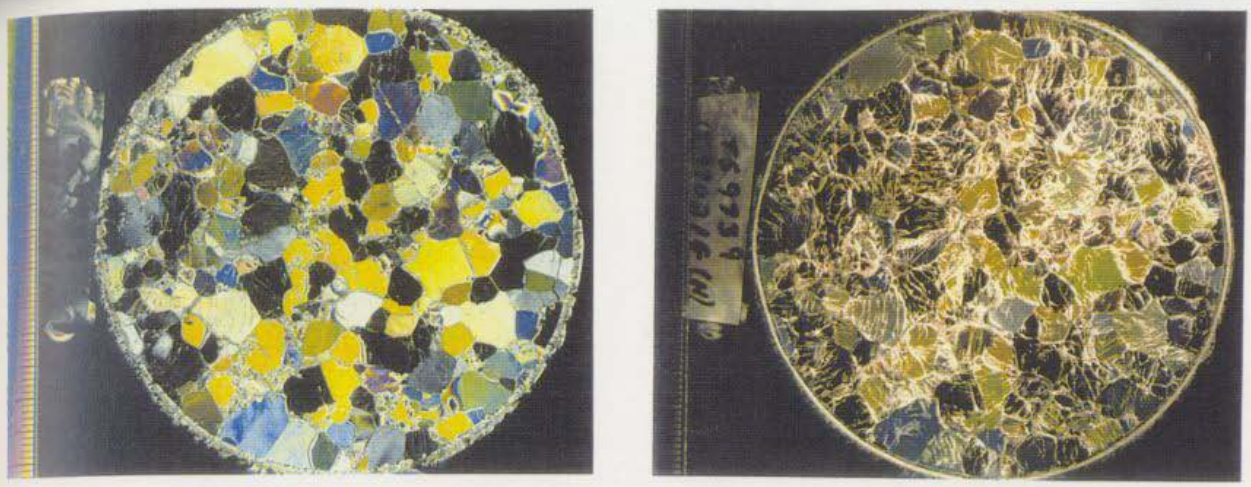

(a) $P_c = 5$ MPa $s = 15$ MPa $\varepsilon = 4\%$

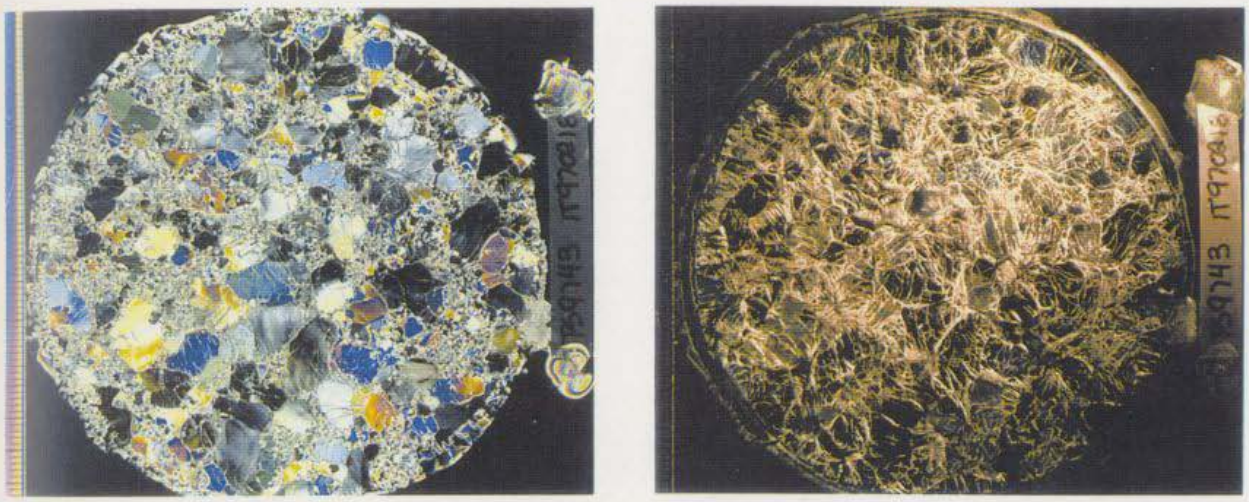

(b) $P_c = 5$ MPa $s = 15$ MPa $\varepsilon = 10\%$

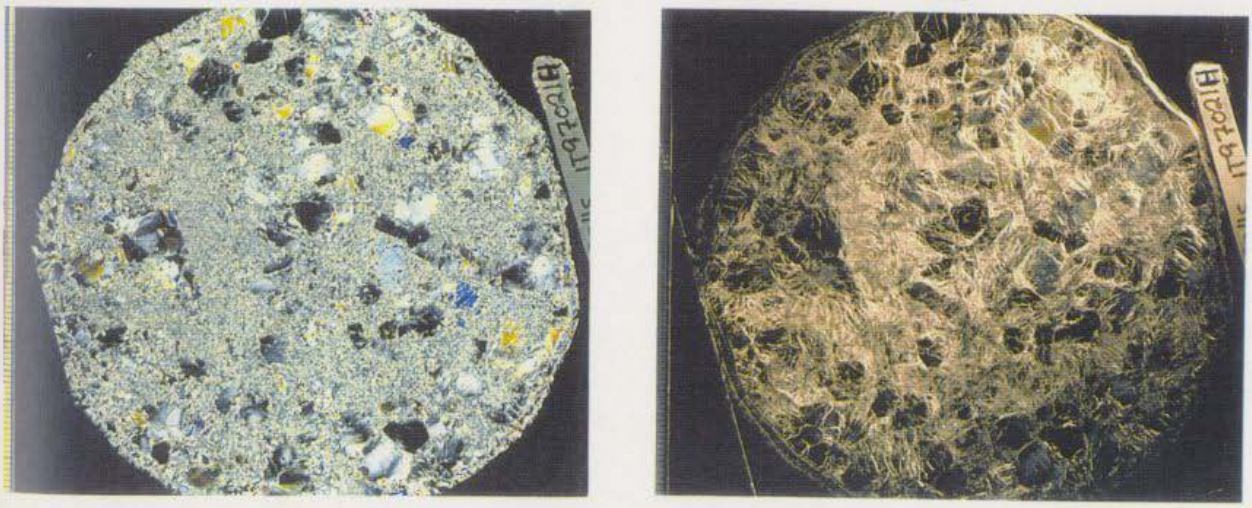

(c) $P_c = 5$ MPa $s = 15$ MPa $\varepsilon = 44\%$

Only one end level of strain was available for creep tests at the midrange confining pressures (Figure 4.9 and 4.10). These photographs show that the samples tested at these pressures had a slightly larger average grain size than those samples tested at the extremes of the pressure range (i.e. p_c = 5 and 50 MPa). There was also less cracking in those samples tested above the 20 MPa confinement level (not all tests are shown), due to the suppressing effect of the higher confining pressure.

The test performed at the higher confining pressure of 50 MPa also showed the suppression of microcracking in the ice. Microcracks were still visible in the thin section photographs, but the density tended to be lower in the high pressure samples than in the low pressure tests. Microstructurally it is believed that the ice was being subjected to separate deformation mechanisms at each of the high, moderate, and low confining pressure zones. This conclusion was strengthened when thin sections of the ice samples tested at these levels showed different fabrics had developed in the microstructure of each set of samples. Recrystallisation and pressure melting are thought to be the dominant mechanisms at work where high pressures and stress concentrations resulted in melting at the triple points of grain boundaries. Microcracking was initially responsible for some microstructural change in the low pressure tests, before dynamic recrystallisation could take advantage of the large grain boundary area to heal and consume cracks. In the moderate confinement zone the character of the ice may have been such that there is not enough confinement to induce large scale dynamic recrystallisation and pressure melting, while the confinement still reduces microcracking. This overall effect results in the ice being stronger and less prone to creep than ice at the extreme high and low pressures.

Figure 4.8 **(On following page)** Thin section photographs of samples tested at a constant stress of 15 MPa and 50 MPa confinement viewed between crossed polarising filters and with side lighting (from Meglis and others, 1998).

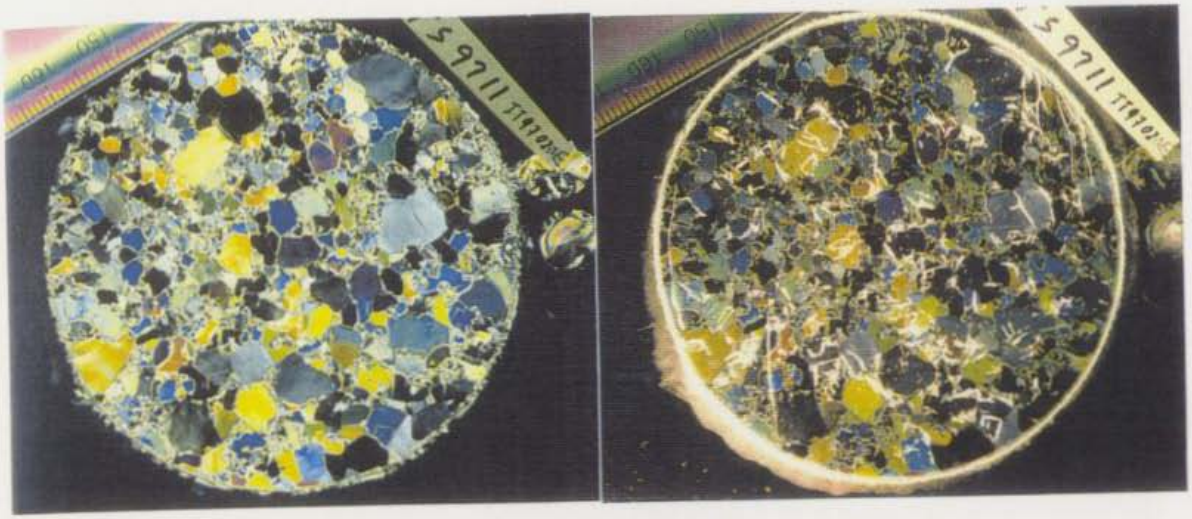

(a) $P_c = 50$ MPa $s = 15$ MPa $\varepsilon = 4\%$

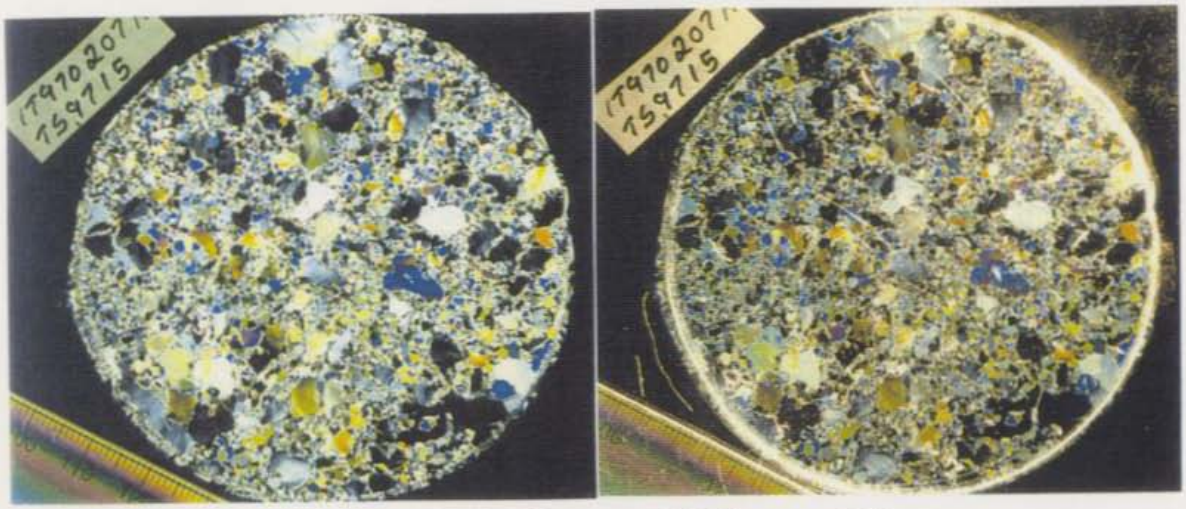

(b) $P_c = 50$ MPa $s = 15$ MPa $\varepsilon = 10\%$

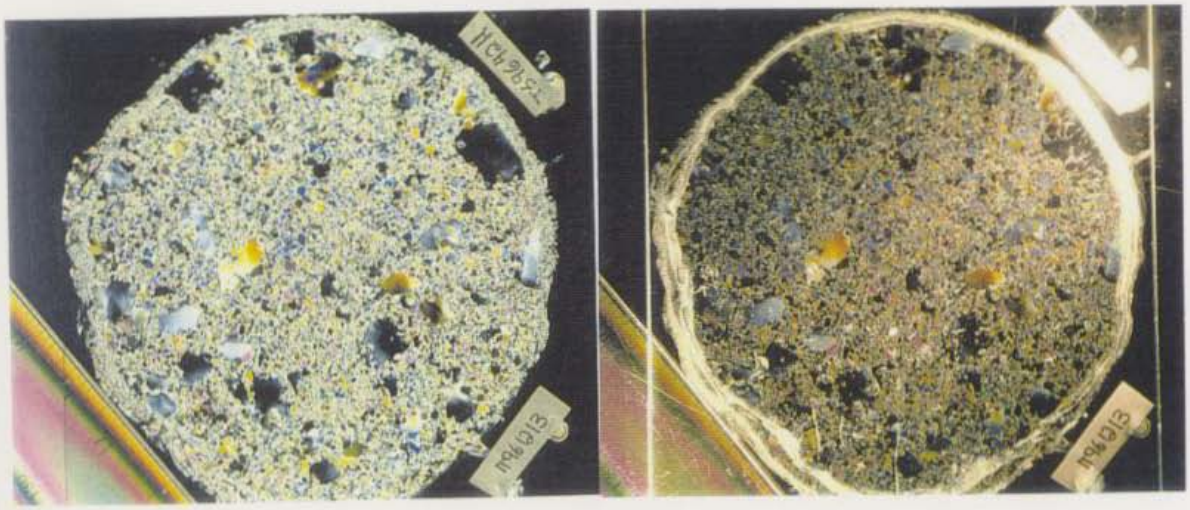

(c) $P_c = 50$ MPa $s = 15$ MPa $\varepsilon = 44\%$

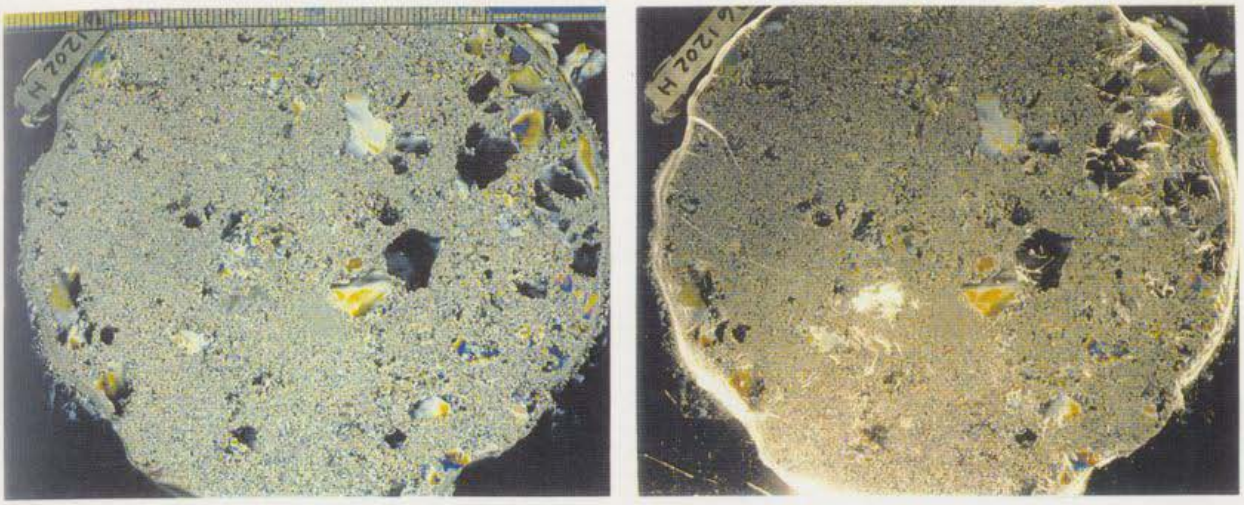

Figure 4.9 Thin section photographs of sample tested at a constant stress of 15 MPa and 30 MPa confinement viewed between crossed polarising filters and with side lighting.

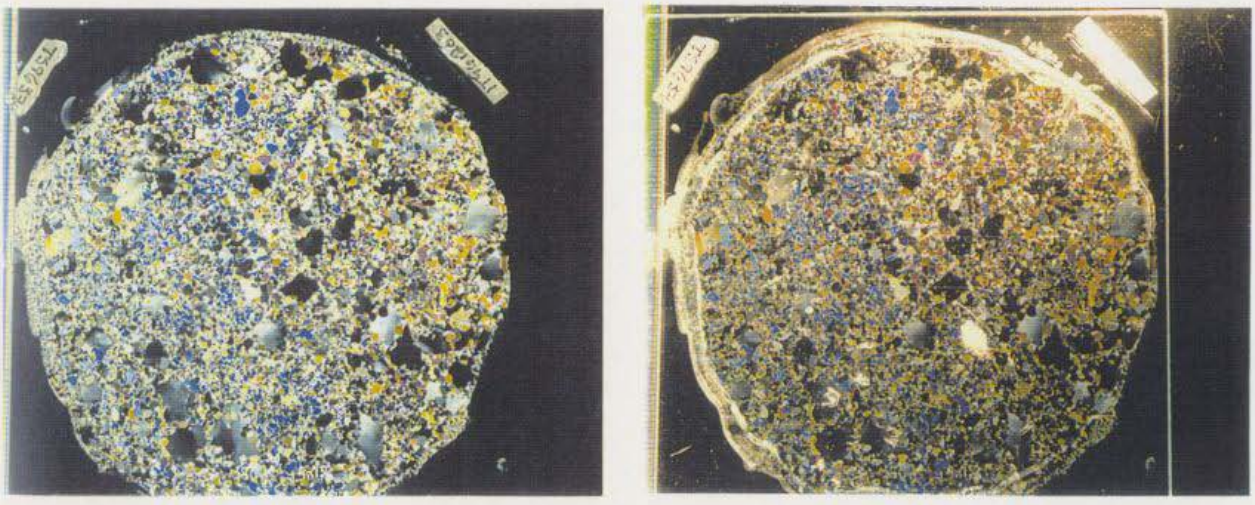

Figure 4.10 Thin section photographs of sample tested at a constant stress of 15 MPa and 40 MPa confinement viewed between crossed polarising filters and with side lighting.

4.3.2 Grain Size, Distribution, and C-axis Orientation

Grain size analysis performed by Meglis and others (1998) is shown graphically in Figure 4.11 and summarised in Table 4.2. The data reveals much the same trend with respect to strain as the plot of grain size versus strain presented in Section 4.2.2 (Figure 4.6), where both sets of grain size measurements were based on the method outlined in Dieter (1976). The plot represent all tests over a range of confining pressures with a constant deviatoric stress of 15 MPa. Grain size was found to decrease significantly in the first few percent of strain in all testing, and tended to settle out to an approximately steady state grain size beyond 10% strain. No statistical representation of the standard deviation was available for the values represented in Table 4.2 as few tests were repeated to exactly the same end condition.

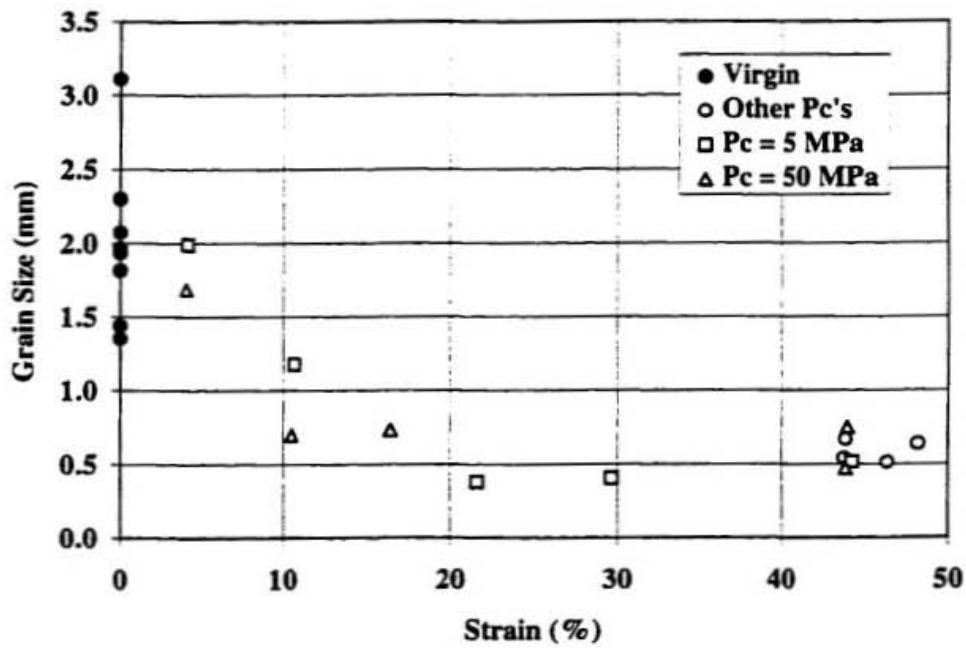

Figure 4.11 Grain size plotted versus total strain for all tests performed at constant stress.

Table 4.2 Final grain size of ice specimens tested at constant load.

Confinement (MPa)	Total Strain (%)	Grain Size (mm/gr.)
--	0	2.00†
5	4.2	1.99
5	10.7	1.18
5	21.6	0.38
5	29.6	0.40
5	44.4	0.52
30	43.9	0.54
40	44.0	0.67
45	48.3	0.64
50	4.1	1.69
50	10.5	0.70
50	16.4	0.73
50	44.0	0.47
50	44.1	0.75
60	46.5	0.51

† Virgin ice grain size based on the average of all untested ice samples examined for this set of tests (standard deviation = 0.55 mm/gr.).

The analysis of the grain size distribution within the thin sections of the constant load tests remains qualitative at this point, but was similar to constant strain rate tests on granular ice with random c-axis orientation. The ice, once deformed past a few percent strain, tended towards a grain distribution that was composed of a few relatively large remnant grain within a matrix of smaller grains. The remnant grain tended to be preferentially oriented with their c-axis parallel (or nearly parallel) with the axis of deformation. This, as mentioned in Section 4.2.2, resulted in grains that survived the initial intra- and intergranular microcracking in the first few percent of strain and went on to remain relatively intact throughout the shortening of the specimen. Meanwhile, the remaining grains underwent microcracking and recrystallisation forming a new

distribution of smaller grains and resulting in a softer granular material during the deformation, possibly acting as a lubricated granular material and easing deformations.

4.3.3 Creep Curves and Mechanical Behaviour

A few words of caution are in order before proceeding to present the creep curves from the constant load tests. Care must be taken when interpreting data from constant load tests when the end result of the sample is unknown or in question. For example, in the tests presented below some samples may appear to have supported load up to end of the creep step. When the curves of uncorrected stress (or load) versus strain are considered, it becomes clear all samples did not support the load for the duration of the test. This means that in some cases strains and large strain rates may have been a result of the hydraulic ram advancing in an attempt find load and not being able to keep up with the rapidly failing sample. This was observed in Meglis and others (1998), when plots of load versus strain indicated that substantial drops in the true load supported by the samples occurred, in particular during tests which eventually failed. Failure is defined as the inability of a sample to support load while rupture is used to refer to large macrocracking in the sample without a clear zone of shear failure. This may bring into question some of the test data that will be used to calibrate constitutive relations.

A second issue of concern is the effect of temperature on the creep rate of ice. In all tests presented in this study the cold room temperature, and therefore the apparatus temperature, was monitored but not controlled. In Meglis and others (1998) it was reported that rupture was more likely to occur in tests where the temperature was a few degrees higher (-7°C versus -9°C) due to the warming effects of the confinement (see also Appendix A). This effect is observed as a result of the ice samples being subjected to relatively large stresses relatively near the melting point.

Data from constant load tests are shown in Figures 4.12, 4.13, and 4.14. The figures represent plots of strain versus time and show the rapid creep experienced by most of the samples in this test set. Figure 4.12 represents constant load tests where the confining pressure was 5 MPa, while Figure 4.13 shows all tests performed at a confining pressure of 50 MPa. The last figure in the series, Figure 4.14, represents all other tests from 20 to 60 MPa of confinement excluding the tests already presented. All the figures also include a second plot of the uncorrected stress supported by the sample during the test plotted versus strain. For most tests the plots are relatively uniform, indicating that the applied

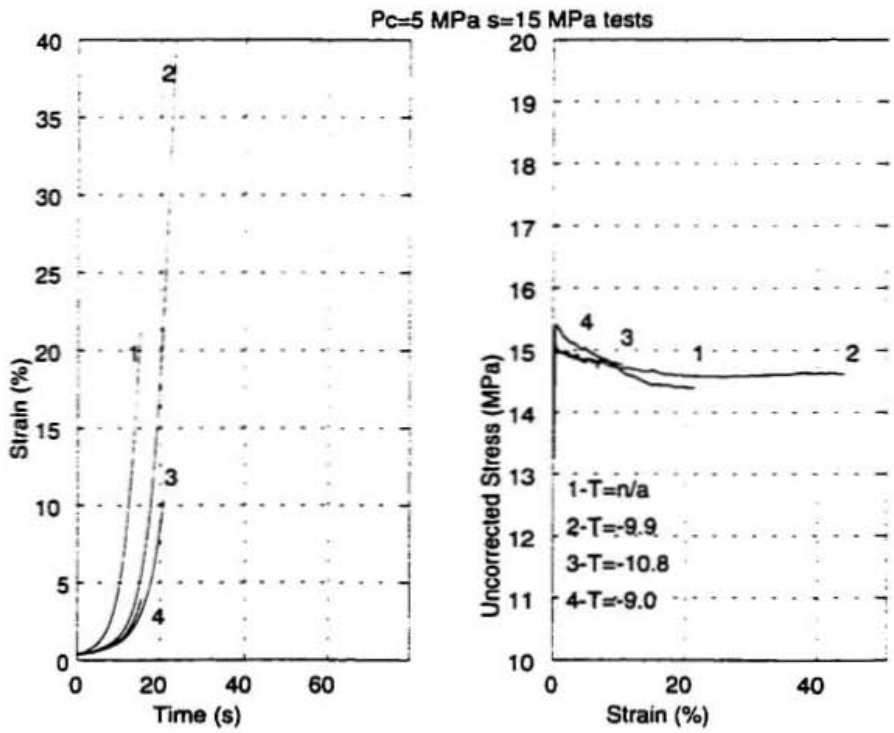

Figure 4.12 Strain plotted versus time and stress versus strain for constant stress tests at s =15 MPa and p_c = 5 MPa.

load was maintained throughout the test. In a few tests a deviation from the constant load is observed. This represents the loss of integrity of the samples, where either rupture or full scale failure of the specimen occurred.

These tests must be examined carefully before using the data to explain the mechanical behaviour and to calibrate constitutive relations. The results can be generally interpreted in two ways. It can be reasoned that the drop in uncorrected stress observed represents the macroscopic failure of the ice where two separate parts of the specimen are sliding across a shear fault plane. The resulting resistance would have been a function of the friction between the two surfaces with sliding occurring as the ram advanced. This

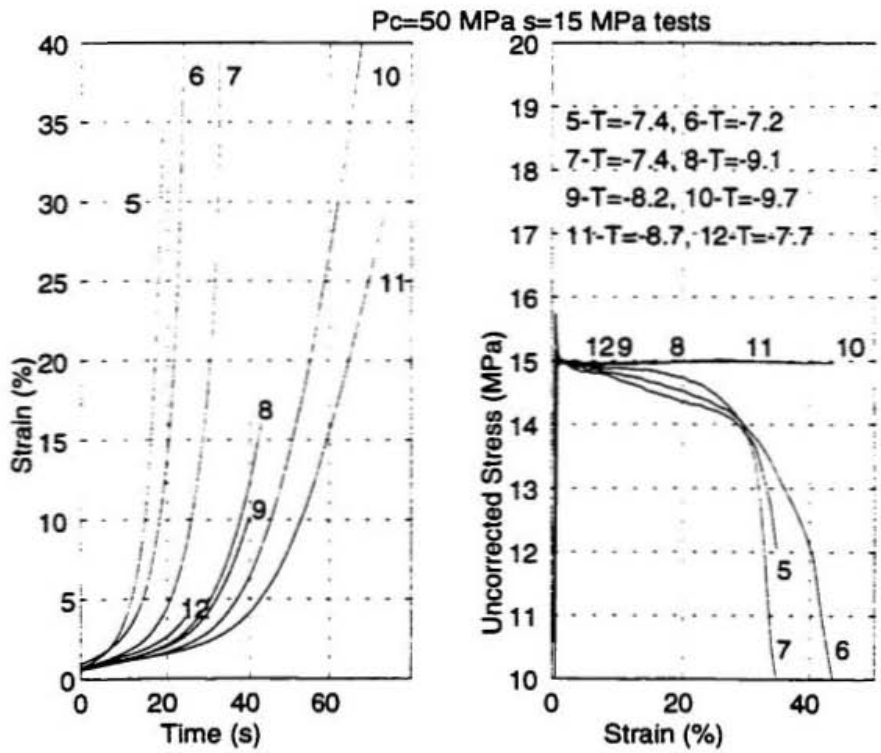

Figure 4.13 Strain plotted versus time and uncorrected stress plotted versus strain for creep tests at s =15 MPa and p_c = 50 MPa.

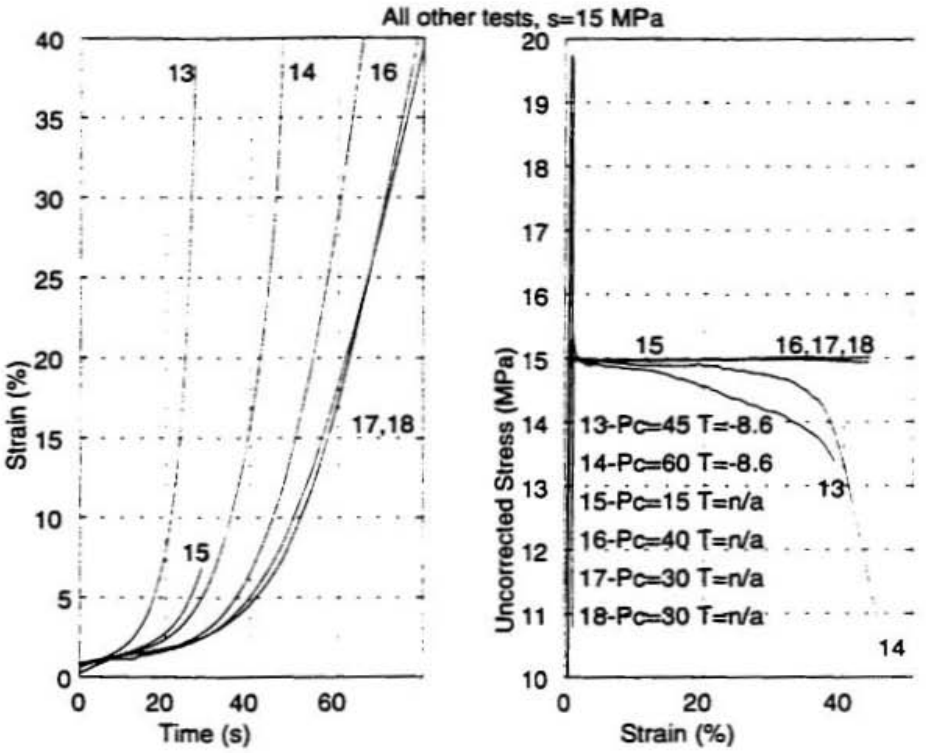

Figure 4.14 Strain plotted versus time and uncorrected stress plotted versus strain for creep tests at s =15 MPa and all other confining pressures.

evaluation leads to interpretation of the high strain rates associated with the end of the tests as largely due to the acceleration of the ram as it attempted to re-establish load. Of course, given that the sample would have practically completely failed, this load could never have been completely re-established. The ice in this case may have been subject to some localised heating which could have cause melting between the two surfaces as sliding occurred.

The other side of the interpretation suggests that the ram, although still advancing in search of the load applied at the beginning of the test, was still applying a load to the ice sample. The load was associated with a localised shear deformation zone within the

sample, where the ice was still deforming and not completely failed as the previous interpretation suggested. In either case the true strain in the material is difficult to evaluate due to the extreme localisation occurring within the ice specimen. As the deformation got larger the specimen eventually failed completely, but not necessarily before accommodating a large amount of local strain.

Microstructurally there does not seem to be a clear case for either interpretation. Thin sections have only shown the existence of a complete fracture in samples where the method of failure was not in question (see Meglis and others, 1998, regarding tests at 30 MPa confinement and 30 MPa differential stress). One of the most obvious problems with identifying the failure mode is that all samples tended to have a fine grained microstructure when they were thin sectioned whether they had failed or not. A simple solution would be to simply observe the samples as they are being deformed, however, this proves difficult as no triaxial confining cell equipped with viewing ports which can accommodate the high pressures used in the study is readily available.

In general the strain curves for the constant load tests show a rapid progression from secondary to tertiary creep. In all cases the samples have reached tertiary creep and were rapidly accelerating by the 45 second mark. Initial parts of the curves, namely the elastic and delayed elastic deformations, were overshadowed by the rapid deformation and were barely visible on the curves shown. This will be discussed in more detail in the next chapter with respect to modelling issues.

Figure 4.12, representing the tests at low confinement, shows how quickly these tests reach tertiary creep. In contrast, tests performed under higher confinement (Figure 4.13) showed more variation, some taking over 30 seconds to reach the tertiary creep phase. This variation may be a function of the temperature and stress at which the samples were tested. Meglis and others (1998) reported on the tendency of the samples at the lower

temperature to survive longer than samples at slightly higher temperatures. It was also indicated that failure was more prevalent in samples tested at a temperature only a few degrees higher than the usual -10°C. More discussion on strain rates observed during testing will be presented in Chapter 5 as strain rates are analysed for calibration with the constitutive model.

4.4 Constant Load Tests on Damaged Ice

4.4.1 Stress Curves and Mechanical Behaviour

For the six tests used in this part of the study, the confining pressure was as shown in Figure 4.15, with 20 MPa of confinement applied for the initial damage step to 12.8% strain, followed by a drop in pressure to 15 MPa or an increase to 30 or 50 MPa for the constant load step. In this section emphasis will be placed on the creep portion of the tests, as the characterisation of the damage step has already been addressed in Section 4.2. Stress versus strain curves for the tests on damaged ice were divided into two sections, the damage step at constant strain rate and the constant load step. The initial damage step was very similar to curves shown previously in Section 4.2 (Figures 4.2 and 4.3). These constant deformation rate curves showed the typical peak stress near 1% strain and the drop to a approximately steady state stress by about 10% strain.

The use of an arbitrary 12.8% strain level in this portion of the test matrix was purely based on qualitative the results and observations obtained in the constant strain rate testing presented in Section 4.2. As the damage at this level had been characterised and represented a relatively damaged but not completely restructured material it was seen as a good benchmark for the damaged ice tests. A quantification of damage, based on damage formulations to follow, was not used to determine the end level of the damage step.

The set of curves in Figure 4.16 represents typical plots of strain versus time for both the damaged ice tests and the corresponding undamaged tests from Section 4.3. These curves indicate the time scale involved in this set of tests with regard to the damage steps. Tests with a strain rate of 10^{-4} s^{-1} for the damage step typically lasted about 1400 seconds while 10^{-2} s^{-1} tests only lasted 200 seconds. The major portion of the slower strain rates tests was the damage step which took over 20 minutes to complete. From the slope of the curves the relative difference in strain rates for both the damage steps and the creep steps can also be observed.

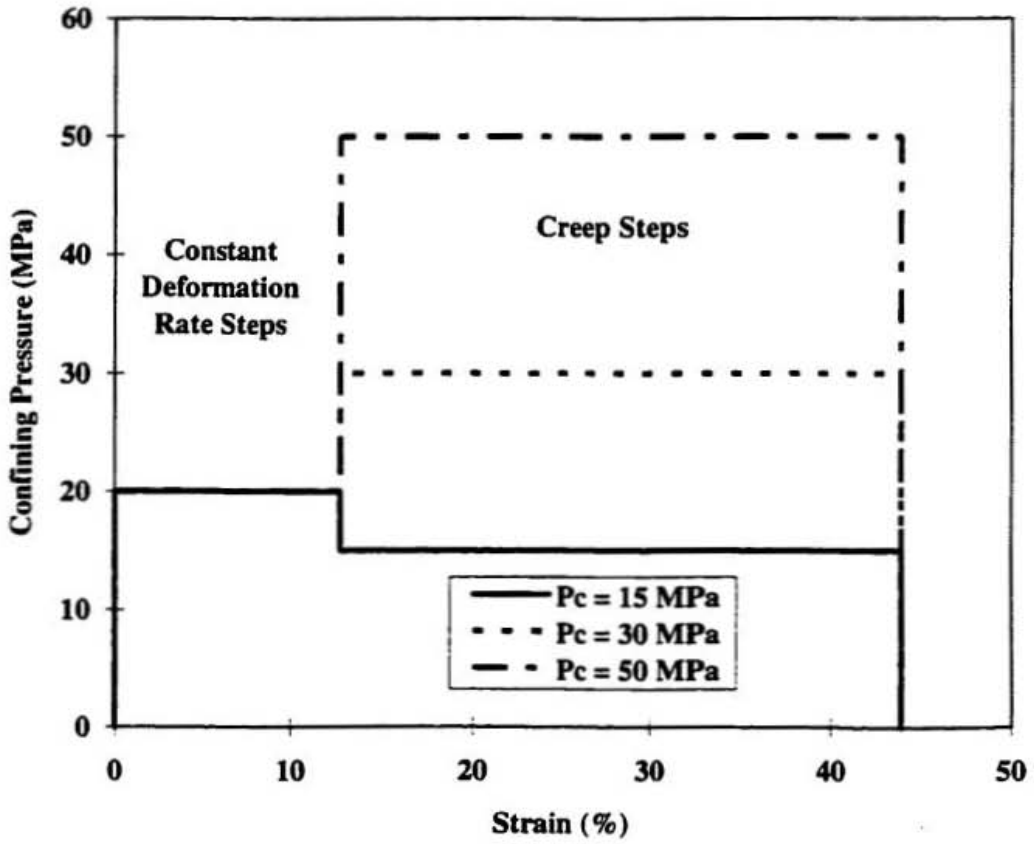

Figure 4.15 Pressure plotted versus strain for each of the three pressure histories used in the constant stress tests of the damaged ice.

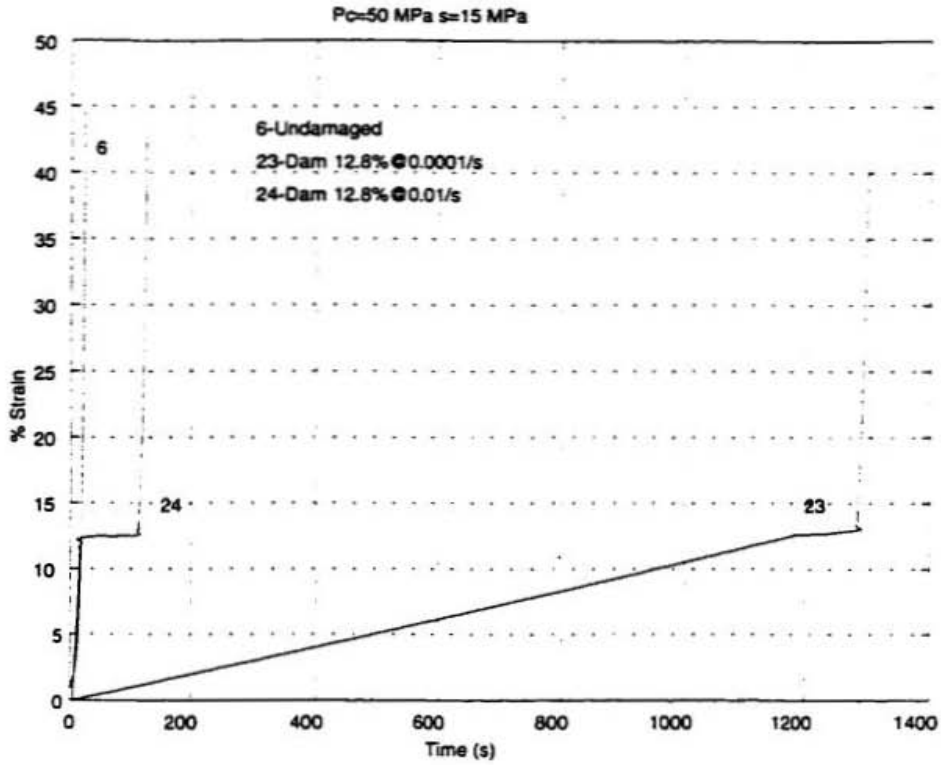

Figure 4.16 Strain plotted versus time for damage step and creep step showing both damage strain rates and undamaged test for p_c = 50 MPa during creep tests.

Isolating the creep portion of the curves (Figure 4.17, 4.18, and 4.19) showed an enhancement of the strain rate in all tests when compared to the response of the undamaged sample under identical conditions. In the high and low pressure tests, the ice damaged at 10^{-2} s^{-1} accelerated to surpass the ice damaged at the slower rate. At the moderate confining pressure of 30 MPa the strain responses of the two damaged ice samples were nearly parallel. This indicates that the response of the ice is very much pressure dependent. It also reinforces the idea that there are two different regimes at work in the ice at high and low pressures, even once the ice has been damaged. The tests

presented show that the pressure is still a major factor in determining the response of damaged ice. The damage mechanisms do have a role in the creep response, especially within the high and low pressure regimes, but do little more than accelerate the runaway or tertiary creep of the curves. In all cases the damage increased the minimum creep rate value attained during the initial seconds of the test.

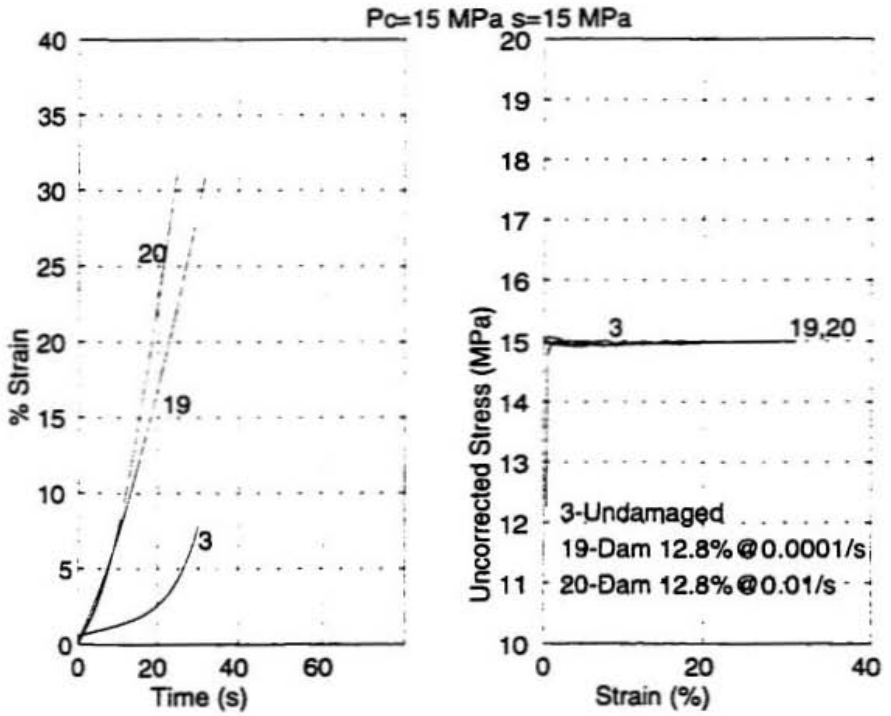

Figure 4.17 Strain plotted versus time for the creep step on damaged ice showing the response of undamaged ice and ice damaged at both 10^{-2} and 10^{-4} s^{-1}, and uncorrected stress plotted versus strain for p_c = 15 MPa during creep tests.

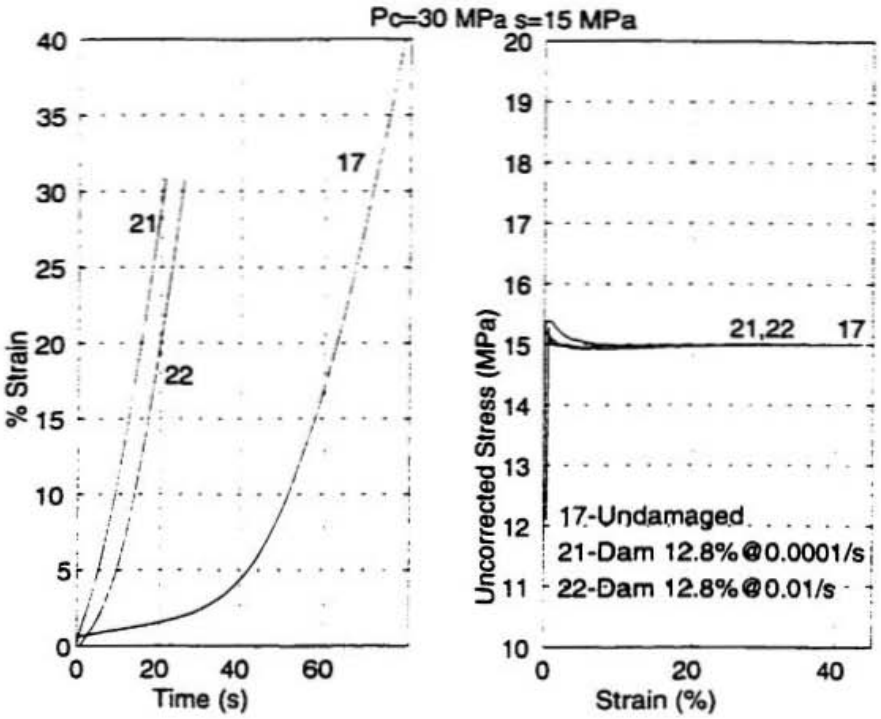

Figure 4.18 Strain plotted versus time for the creep step on damaged ice showing the response of undamaged ice and ice damaged at both 10^{-2} and 10^{-4} s^{-1}, and uncorrected stress plotted versus strain for p_c = 30 MPa during creep tests.

4.4.2 Grain Size, Distribution, and C-axis Orientation

Due to the large strains that were accommodated by the damaged ice samples, the grain size was expected to be small with respect to the virgin ice. This was observed in all six tests but was particularly apparent in the tests subjected to high pressure creep, where the grain size was 30 and 20% smaller for the high and low strain rate damage, respectively. The grain size for each test is shown graphically in Figure 4.20, as well as in Table 4.3, with respect to confining pressure.

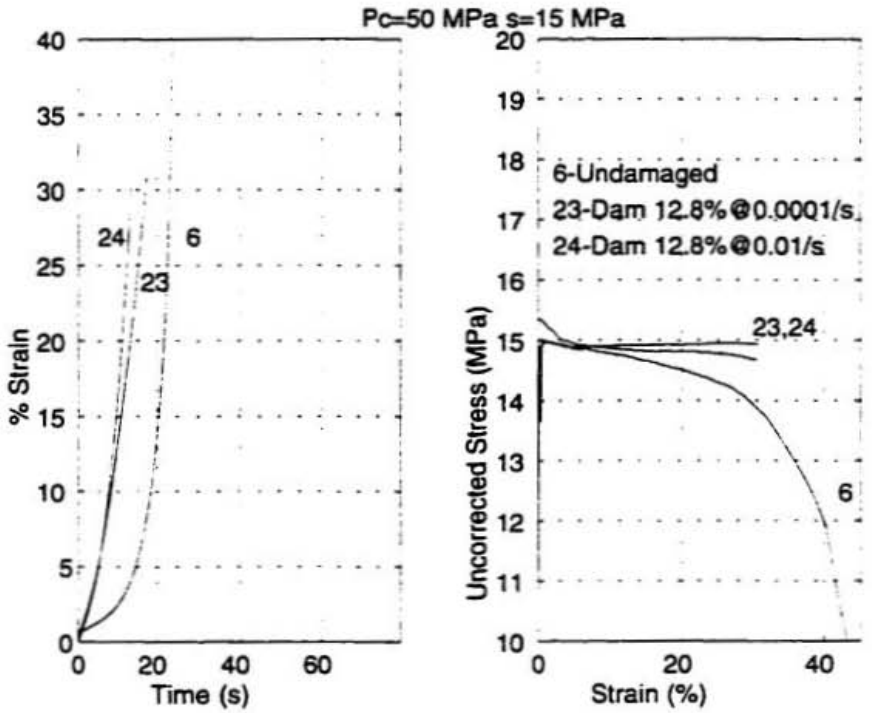

Figure 4.19 Strain plotted versus time for the creep step on damaged ice showing the response of undamaged ice and ice damaged at both 10^{-2} and 10^{-4} s^{-1}, and uncorrected stress plotted versus strain for p_c = 50 MPa during creep tests.

Table 4.3 Final grain size of damaged ice specimens following creep step.

Damage Step Deformation Rate	Creep Step (s = 15 MPa)		
	p_c = 15 MPa	p_c = 30 MPa	p_c = 50 MPa
10^{-2} s^{-1}	0.69 mm/gr.	0.71 mm/gr.	0.48 mm/gr.
10^{-4} s^{-1}	0.73 mm/gr.	0.78 mm/gr.	0.64 mm/gr.

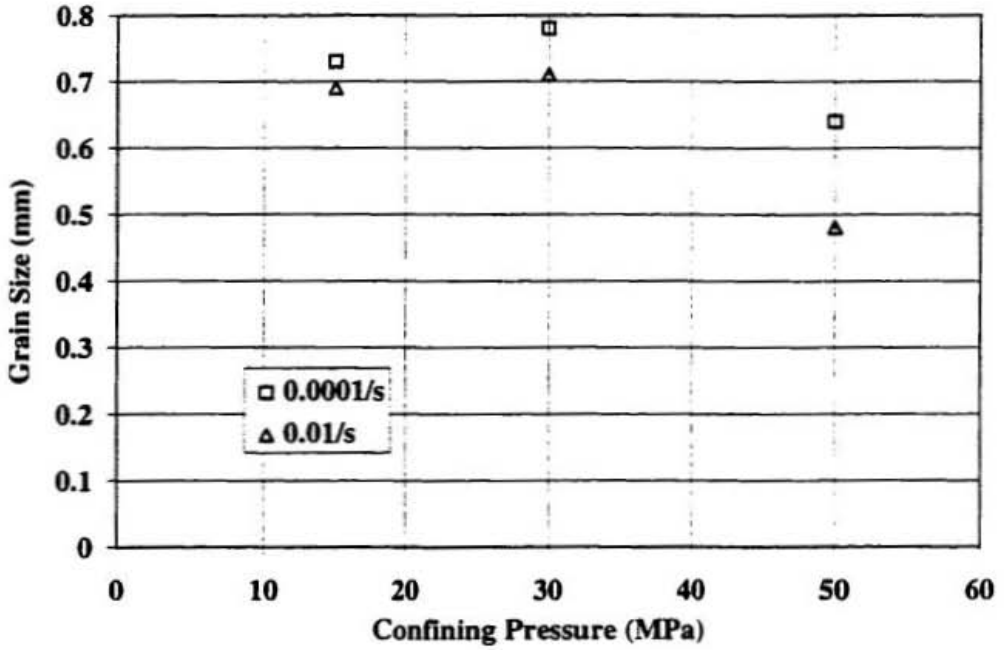

Figure 4.20 Grain size plotted versus total strain for all creep tests performed on damaged ice.

Remnant grains were apparent in both samples damaged at the high and low strain rates. The damage step strain rate may have been a factor in determining the relative size of the grains. The difference in pressure during the creep step did not seem to have an effect on the presence of the remnant grains in the deformed samples. Figures 4.21 and 4.22 show thin section photographs of tested samples viewed between crossed polarising filters and with the addition of side lighting for all three confining pressures and both damage rates. The samples damaged at the lower strain rate seemed to have smaller remnant grains than the samples damaged at the higher strain rate. More study is needed before conclusions into this observation can be drawn.

Figure 4.21 **(On following page)** Thin section photographs of damaged ice samples tested at a constant stress of 15 MPa viewed between crossed polarising filters and with side lighti..g. The damage deformation rate was 10^{-2} s^{-1}.

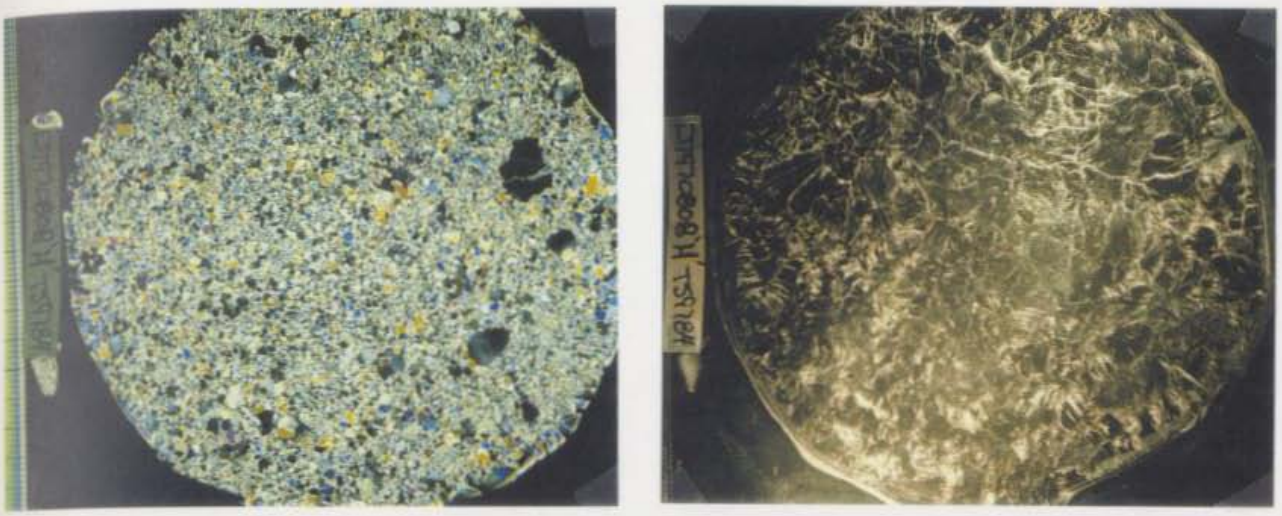

(a) 12.8% @ 10^{-2} s^{-1} and p_c = 20 MPa followed by s =15 MPa and p_c = 15 MPa

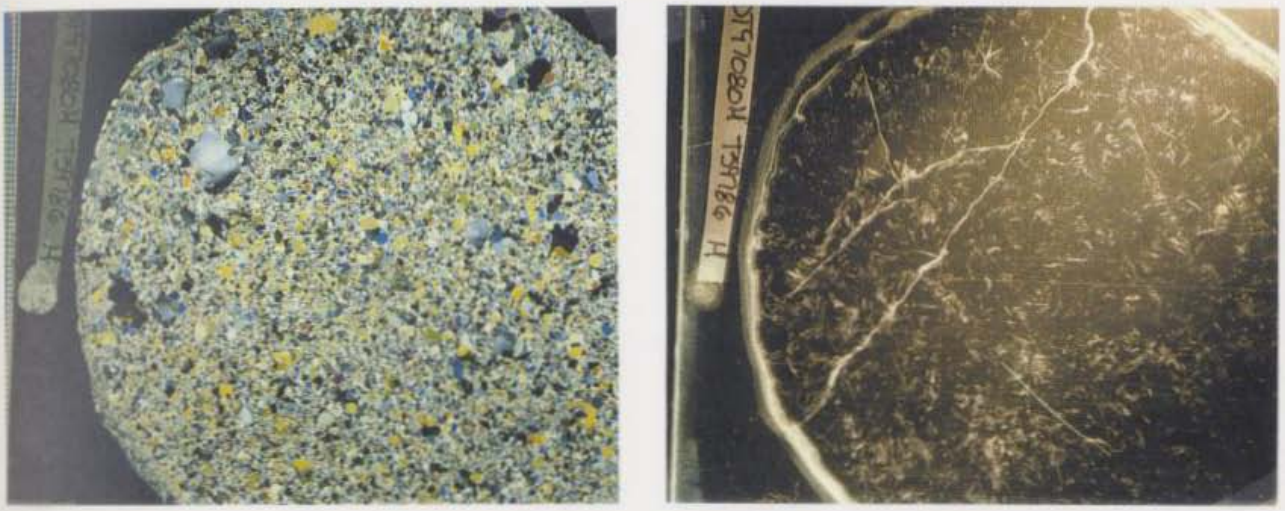

(b) 12.8% @ 10^{-2} s^{-1} and p_c = 20 MPa followed by s =15 MPa and p_c = 30 MPa

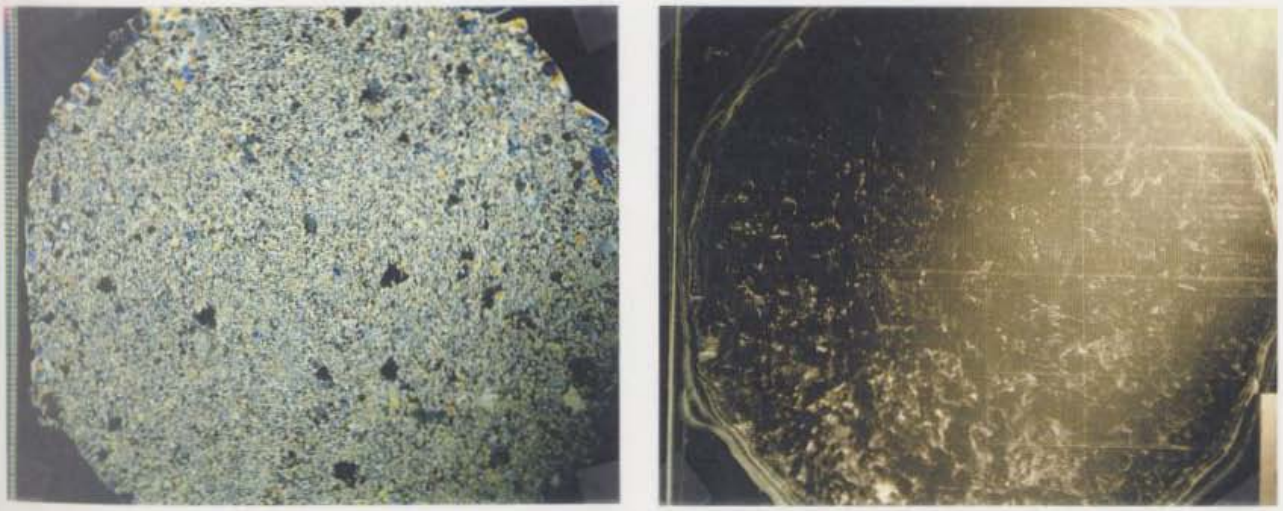

(c) 12.8% @ 10^{-2} s^{-1} and p_c = 20 MPa followed by s =15 MPa and p_c = 50 MPa

In many cases the c-axis orientation was hard to determine as the dimensions of the individual grains were on the same order (and less than) the thickness of the thin section. This resulted in grains being stacked two or more thick in the thin section and inhibiting the effects of the polarising filters in defining the grain boundaries. In these cases the polarised light from the bottom polarising filter was refracted twice or more by several grains before passing through the top filter. This altered the colour of grains and made it impossible to determine the orientation of the smaller grains in the sample. The result tended to appear as a white mass of grains or as grains with relatively thick grain boundaries. The effect of grain boundaries that were oriented at a relatively low angle with respect to the filters also made identifying grain boundaries difficult.

The c-axis orientation of the larger grains in the sample, and especially the remnant grains, was easier to determine. As in the constant strain rate testing, the remnant grain tended to have a c-axis orientation that was parallel or nearly parallel to the axis of deformation. This was observed by the optical extinction presented by the grains as the thin section was rotated between crossed polarising filters.

4.4.3 Microcracking and Recrystallisation

Microcracking in the samples observed at the end of each test was found to be dependent on the level of pressure in the constant load step. In the ice damaged at 10^{-2} s^{-1}, with p_c = 20 MPa, followed by a creep test (s =15 MPa) at p_c = 15 MPa, a large amount of microcracking was distributed throughout the sample as both inter- and intragranular microcracking. The same was also observed in thin sections of samples

Figure 4.22 **(On following page)** Thin section photographs of damaged ice samples tested at a constant stress of 15 MPa viewed between crossed polarising filters and with side lighting. The damage deformation rate was 10^{-4} s^{-1}.

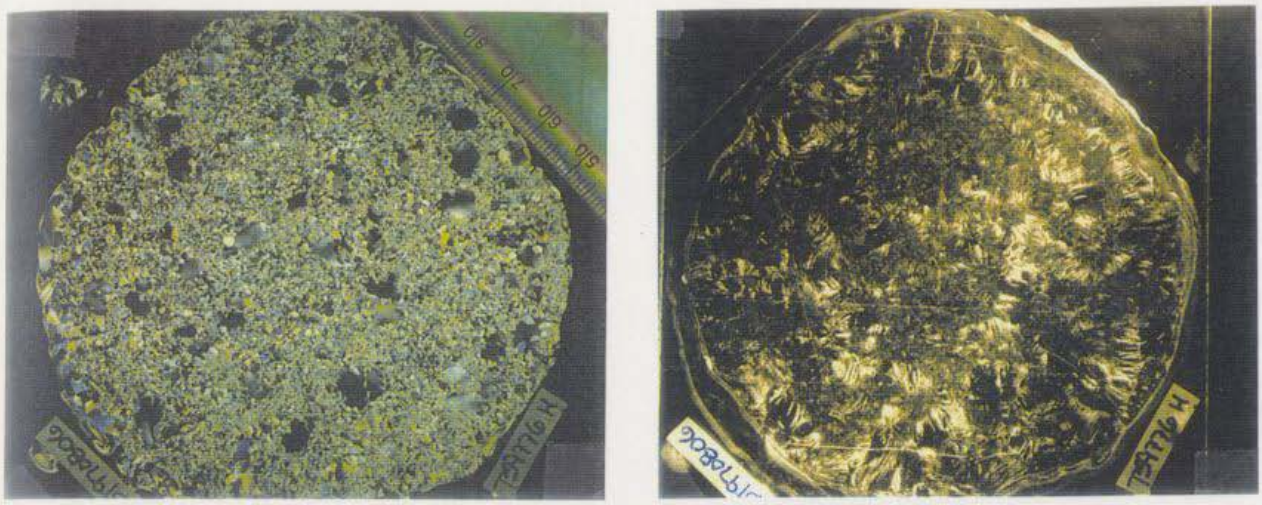

(a) 12.8% @ 10^{-4} s^{-1} and p_c = 20 MPa followed by s =15 MPa and p_c = 15 MPa

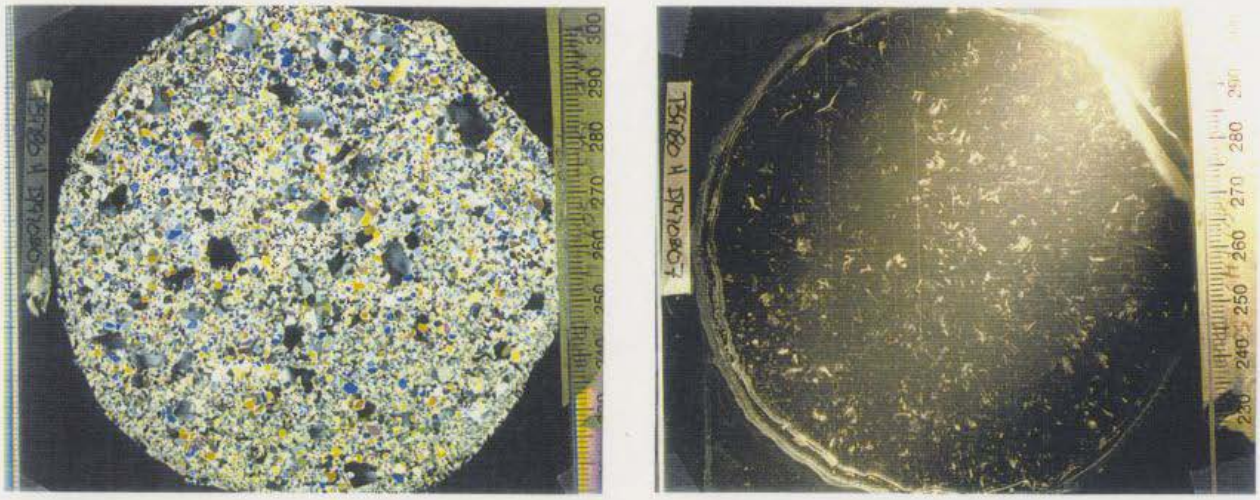

(b) 12.8% @ 10^{-4} s^{-1} and p_c = 20 MPa followed by s =15 MPa and p_c = 30 MPa

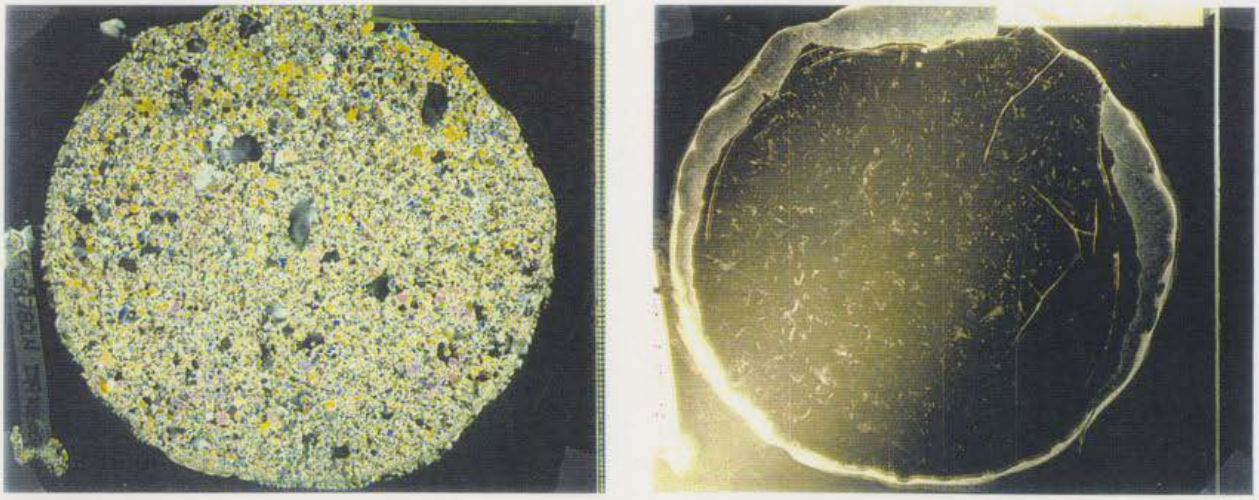

(c) 12.8% @ 10^{-4} s^{-1} and p_c = 20 MPa followed by s =15 MPa and p_c = 50 MPa

damaged at a strain rate of 10^{-4} s^{-1}. This is not unexpected as the reduction in pressure from the constant strain rate to the creep step (20 MPa ⇒ 15 MPa) would allow cracking to take place. The fact that the cracking is so widespread throughout the sample is interesting given that this sample was shortened to 44% strain and that thin sections of samples deformed under constant deformation rate as far as 28.8% showed almost no signs of cracking. In the constant deformation rate tests the microcracks were thought to be mostly consumed by recrystallisation, having been replaced by a matrix of smaller grains. Given the small grain size within the sample after the 12.8% constant deformation rate damage step, crack size was not expected to be this large.

The microcracking observed in the low pressure constant load tests was not apparent in the tests at higher pressures. The two samples that were subjected to the creep deformation at a pressure of 50 MPa following the damage steps did not show significant microcracking at the end of the test. This once again indicates the presence of different deformation mechanisms over varying confining pressure within the ice.

4.5 Testing Summary and Discussion

The results of the triaxial testing presented shows the effects of various stress and deformation histories on laboratory made granular freshwater ice. Testing at constant deformation rates (p_c constant at 20 MPa) showed differences between deformation at high (10^{-2} s^{-1}) and low (10^{-4} s^{-1}) strain rates. Microcracking was the major difference observed, with the high strain rate tests experiencing both intra- and intergranular cracking throughout. Lower strain rate testing showed significantly less cracking as well as the effects of recrystallisation on the ice, especially at large strains. The result in both cases, irrespective of the actual stress path, was a significant drop in the grain size from 2.38 mm/gr. to an average below 1.0 mm/gr.

The drop in grain size was also observed in other types of testing. Constant load tests performed at various confining pressures showed a decrease in grain size that seemed to be independent of the confining pressure. Cracking in these tests was dependent on pressure with large crack densities in tests at low pressures. Higher pressures tended to suppress microcracking but did not eliminate it, instead the mechanism was replaced with large scale dynamic recrystallisation and possible pressure melting. The pressure had the effect of isolating two deformation regimes in the ice, namely microcracking and recrystallisation, which occurred at low and high pressures respectively. The high and low pressure regimes also showed enhanced creep rates when compared to moderate confinement. The time to tertiary creep was observed to increase as the pressure moved away from the transition pressure (between p_c = 30 and 40 MPa).

Creep tests on damaged ice were limited to six tests with damage applied at two different strain rates. Thin sections of tested samples showed a reduction in grain size on the same order as those observed in both other modes of testing for equivalent levels of strain. Cracking was not observed at the high strains but is expected to have occurred earlier in the damage steps based on observations of the constant deformation rate tests examined in Section 4.2.

Figure 4.23 represents a plot of the grain size of all tested samples versus the total strain. No significant difference in final grain size was initially detectable with respect to the stress history (i.e., constant deformation rate, constant load, or damaged test) and the grain size seemed mainly to depend on the total strain. This may indicate that damage in the ice, which has been used to define the softness of the material using damage mechanics, is mostly dependent on the grain size and therefore the total strain. The scatter in tests to low strains ($e < 5\%$) may suggest that the dependence is affected by other mechanisms and factors at this level.

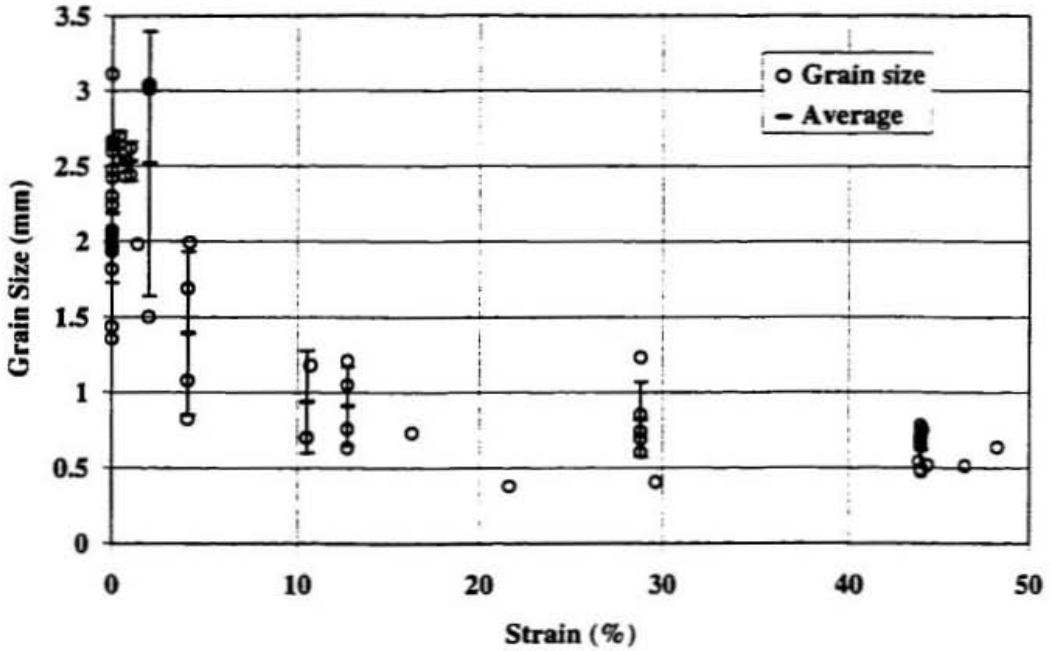

Figure 4.23 Grain size plotted versus total strain for all tests in test matrix.

Chapter 5

Applications to Modelling

The data collected during the triaxial tests presented in Section 4.3 was used during the course of this study and other studies (Xiao, in preparation) in the derivation and calibration of a pressure-dependent constitutive relation for ice. Still other studies have used parts of this data in the modelling of ice-structure interaction using the finite element program ABAQUS (Jordaan and others, 1997). In this chapter the basic framework for the development of the constitutive model and the steps required to determine the preliminary parameters will be presented. Corrections which were performed on the data are addressed as well as changes to this specific model and its parameters from previous studies.

5.1 The Pressure-dependent Constitutive Model

The strain and strain rate data from the previous chapter shows that damage in ice significantly enhances creep rates during subsequent constant load tests, particularly at high and low confining pressures. This can also be observed when strain rates obtained from several different sources are considered (Table 5.1). In this table strain rates from

Sinha's strain relation (Sinha, 1978) are represented for comparison; results from a model developed by Xiao and Jordaan (1996) and test data are also shown.

It can be observed from Table 5.1 that there are drastic changes in the strain rate as strain becomes increasingly large during constant load (or constant stress) tests. This is a function of the mechanical response of the ice moving from primary and secondary creep regimes into rapidly accelerating tertiary creep. The strain rates presented in the table show an increase in the strain rate by two to three orders of magnitude in collected data from initial creep rates to the end of tests. The two tests selected from the triaxial test data to be represented here were not the fastest in the test series. They were typical tests, but strain rates beyond the levels represented here are possible as the ice continues to be damaged and deformed.

A second point which becomes important, once the magnitude of the large strain rates are considered, is that the actual strains associated with these strain rates are also large.

Table 5.1 Strain rates for at various strains s = 15 MPa based on different relations and experimental results for polycrystalline ice.

Strain rate units (s^{-1})	t = 0 s	Minimum	ε = 5%	ε = 20%	ε = 40%
Sinha† (1978)	1.5×10^{-3}	6×10^{-4}	6×10^{-4}	6×10^{-4}	6×10^{-4}
Xiao and Jordaan (1996) p_c = 0 MPa	1.3×10^{-5}	1.2×10^{-5}	2.1×10^{-4}	9×10^{-4}	1.8×10^{-3}
Xiao and Jordaan (1996) p_c = 15 MPa	1.3×10^{-5}	9.2×10^{-5}	5.5×10^{-5}	2.3×10^{-4}	4.6×10^{-4}
Xiao and Jordaan (1996) p_c = 50 MPa	1.2×10^{-5}	6.8×10^{-6}	2.3×10^{-5}	9.2×10^{-5}	1.7×10^{-4}
Test Data p_c = 15 MPa	1×10^{-3}	4×10^{-4}	6×10^{-3}	2.5×10^{-2} ‡	5×10^{-2} ‡
Test Data p_c = 50 MPa	8×10^{-4}	4×10^{-4}	3×10^{-3} to 1.4×10^{-2}	8×10^{-3} to 1.4×10^{-1}	1.1×10^{-2} to 1.5×10^{-1} ‡

† Sinha's relation is only valid for uniaxial conditions is represented here only for comparison.
‡ Estimated from data.

In most case where large strains are involved (usually within high stress regimes) the contribution of elastic and delayed elastic strains becomes small with respect to the viscous deformations. In the creep tests presented in Section 4.3 and 4.4, elastic and delayed elastic strains represent less than 1% of the total deformation in some cases. These ratios go on to drop drastically as the duration of the test is increased and strains become even larger. For example, if a tests were allowed to proceed longer, for as little as 10 seconds at a strain rate on the order of 2×10^{-2} s^{-1}, the strain would increase by at least 20% and possibly as much as 40%. This is based on extrapolating data from creep curves and the continuously accelerating strain rate. This increase reduces the elastic and delayed elastic contribution to much less than 1% of the total strain.

The magnitude of this ratio between the elastic and viscous strains is one reason the development of the model presented in this work has turned away from modelling the whole mechanical behaviour of ice (including elastic, delayed elastic, and viscous deformations). Instead, modelling only the viscous component of the Burgers body is seen as the optimum direction to choose. To understand this strategy one need only consider studies of ice-structure interaction in the field where crushing is the primary failure mechanism (see Section 2.2). In these cases the deformation is typically well beyond the elastic and delayed elastic range as indicated by the large scale crushing and extrusion of ice. Deformations often occur in a quick and explosive nature. Modelling at the expected speed of interaction has still not been achieved, however, experimental work with ice tested to large strain levels and high strain rates are beginning to help understand the deformations and develop constitutive models for the material.

Returning to the model, the reduction (or simplification) of the Burgers body, in the context of neglecting the elastic and delayed elastic components, serves to reduce the complexity of the problem significantly. Figure 5.1 represents the steps in the break-up

of the Burgers body to the final form that has been used in this study. Beginning with a Kelvin and a Maxwell unit in series, the body is initially reduced by neglecting the spring representing the delayed elastic component in the Kelvin unit. This leads to the combination of the two dashpots in series. The removal of the spring can also be interpreted from a damage mechanics point of view. Initially for low damage levels (low stresses) and low strains the model remains intact and behaves normally. As strains increase damage is accumulated in the model, specifically in the springs. As the amount of damage continues to increase the integrity of the springs is diminished and the load

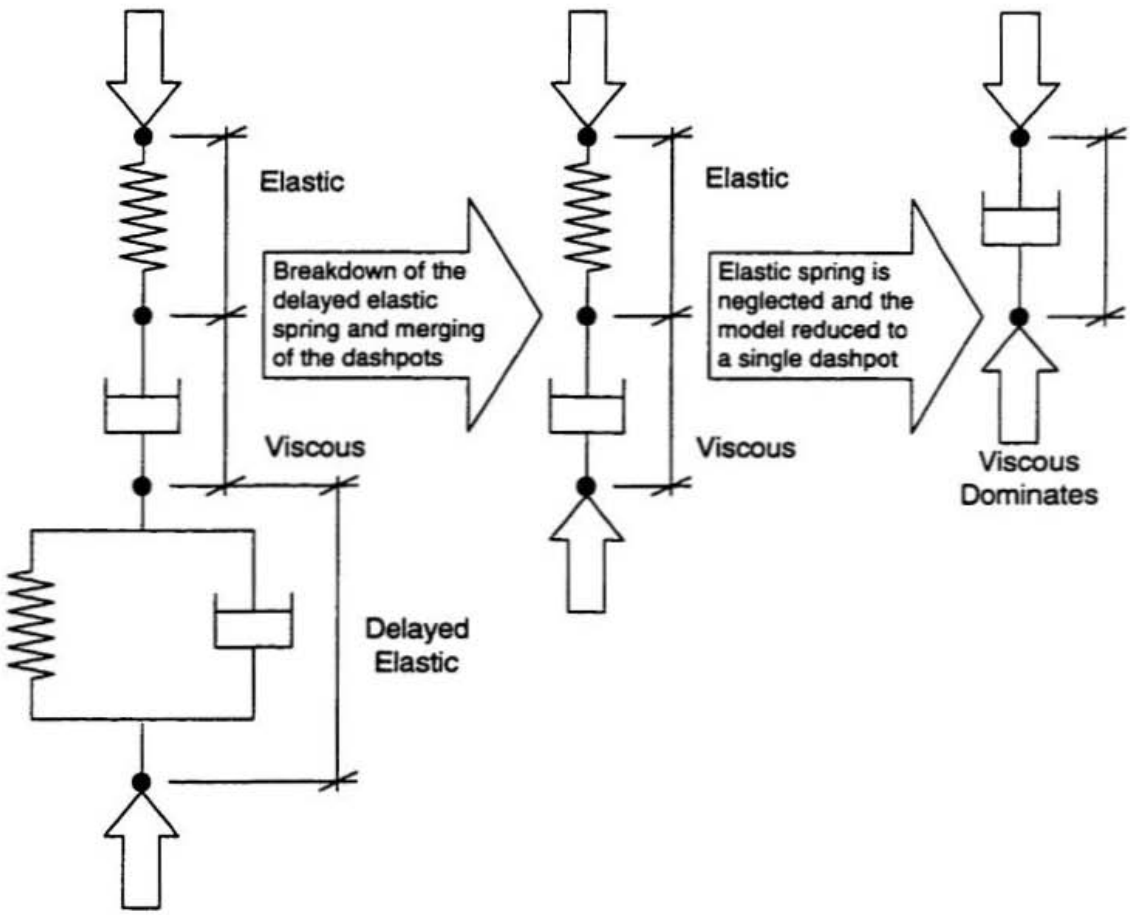

Figure 5.1 The reduction of the Burgers body to a single dashpot.

supported by these elements is reduced. Eventually they can be considered broken since their contribution to supporting stress in the overall system approaches zero. This essentially removes the spring elements from the system and forces the dashpots to support the load. Microstructurally the change in emphasis from springs to dashpots is credited to the creation of grain boundary volume (i.e., a decrease in grain size) and the reduction in the stress at triple points, all of which is a result of restructuring that is occurring in the ice both through recrystallisation and microcracking.

The Burgers body is reduced a second time by removing the spring which represents the elastic component of the ice from the Maxwell unit leaving a single combined non-linear dashpot. The argument for this spring is much the same as for the previous one; for large strains elastic contributions only represent a small fraction of the deformation. The result is a model that is only valid for large stresses acting over large strains, but avoids the complexity of dealing with the other components for situations where their contributions will become negligible. The system, composed of a single unit, then becomes relatively easy to calibrate with the collected data.

Although the two interpretations presented may be different in their approach, one based on relative magnitudes of strain components and the other on damage mechanics, they both lead to a similar solution. Both represent the effects of large strains and the subsequent high strain rates in the ice based on large stresses. The two were used in deriving the pressure dependent viscous model presented in the next section.

5.1.1 Derivation of the Pressure-dependent Constitutive Model

The derivation of the pressure-dependent constitutive model is based on the following relationship between the deviatoric component of strain rate and a stress-dependent viscosity (representing the reduced Burgers body from Figure 5.1):

$$\dot{e}_{ij} \propto \frac{s_{ij}}{\eta(s)} \tag{5.1}$$

where s_{ij} is the deviatoric component of stress ($s_{ij} = \sigma_{ij} - \frac{1}{3}\sigma_{ii}$), $\dot{e}_{ij}$ is the deviatoric strain rate, and $\eta(s)$ is the stress-dependent viscosity. The expression for $\eta(s)$ can be written as:

$$\eta(s) = g(S)s^{-(r-1)} \tag{5.2}$$

where $g(S)$ is the enhancement function due to a damage level, S, and s is the von Mises stress (equivalent to the deviatoric stress). In previous studies, $g(S)$ has been of the form $e^{\beta S}$ (Schapery, 1981; Jordaan and McKenna, 1988). Here a similar form is used for the enhancement of creep by damage. The non-linearity of creep is expressed by the exponent, r, assumed to be very near 3 based on the third-power dependence of strain rate on stress. The expression for the damage, S (Xiao and Jordaan, 1996; Singh and Jordaan, 1996b), is based on the derivation of Schapery (1981, 1984):

$$S = \int_0^t f(p)\left(\frac{s}{s_0}\right)^q d\tau \tag{5.3}$$

where $f(p)$ is a general function of hydrostatic pressure which can lead to either a reduction in the creep rate by suppression of tensile zones at microcracks, or to an increase in creep rate by pressure melting. Determining the form of $f(p)$ was the main objective of the constant stress testing presented in Chapter 4. The quantities s_0 and q in Equation 5.3 are constants. Equation 5.3 was based initially on the relation between the crack growth rate in viscoelastic materials, expressed as a power of the energy release rate (Schapery, 1981).

Since the series of tests used in the calibration was conducted under a nominal constant differential stress, the dependence of damage rate on differential stress has not been determined. It has been assumed that the damage rate is proportional to s^5 for the range of pressures tested. The value of the exponent was determined for earlier

constitutive models from the triaxial tests conducted under lower hydrostatic pressure and differential stresses (Xiao and Jordaan, 1996).

Continuing with the formulation, the viscosity, $\eta(s)$, is then given as:

$$\eta(s) = \frac{e^{-S} s^{-(r-1)}}{k} \tag{5.4}$$

where the damage function S is given in Equation 5.3, r is the expression of the non-linearity of creep, and k is a constant of proportionality from Equation 5.1.

For constant stress tests, as used in this calibration, the damage depends only on time, and Equation 5.3 then becomes:

$$S = f(p)\left(\frac{s}{s_0}\right)^q t \tag{5.5}$$

Equations 5.1 and 5.4 can then be combined to yield the following equation for strain rate:

$$\dot{e} = e^S s^r k \tag{5.6}$$

Substituting Equation 5.5 for the exponent S and taking the natural logarithm of both sides yields:

$$\ln(\dot{e}) = \frac{f(p)}{s_0^q} s^q t + r \ln(s) + \ln(k) \tag{5.7}$$

Equation 5.7 reveals that the natural logarithm of the strain rate should be linear with time for constant stress, which leads to a simple equation of the form:

$$\ln(\dot{e}) = \phi t + I \tag{5.8}$$

where the slope, ϕ, is equal to the damage rate ($\frac{dS}{dt}$) and the zero-intercept, I, is expressed as:

$$I = r \ln(s) + \ln(k) \tag{5.9}$$

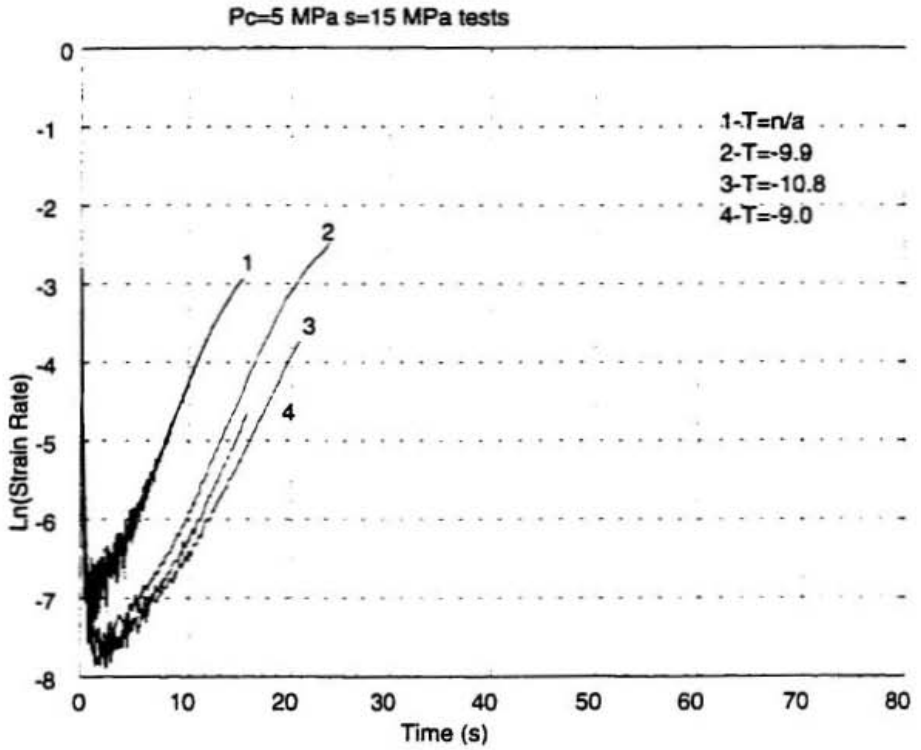

Figure 5.2 Plot of the logarithm of strain rate versus time for constant stress tests performed at p_c = 5 MPa.

Using Equation 5.8 to describe linear portions of the experimental data the parameters ϕ and I were obtained for the constitutive model.

5.2 Model Calibration

5.2.1 Data Analysis

The plots of the logarithm of strain rate versus time for each test are shown in Figures 5.2, 5.3, and 5.4. Figure 5.2 shows the results from tests performed at a confining pressure p_c = 5 MPa. Figure 5.3 shows the tests done at p_c = 50 MPa and Figure 5.4 shows all remaining tests performed at other values of p_c. In general the curves all show

a drop in initial strain rate associated with loading and elastic deformation in the first few seconds of loading. The plots also show a minimum strain rate for each curve, as well as a linear portion. This linear portion will be used in the calibration of the pressure dependent constitutive model as described in the previous section. The curves will be discussed in more detail with respect their general shape and trends once the data has been corrected.

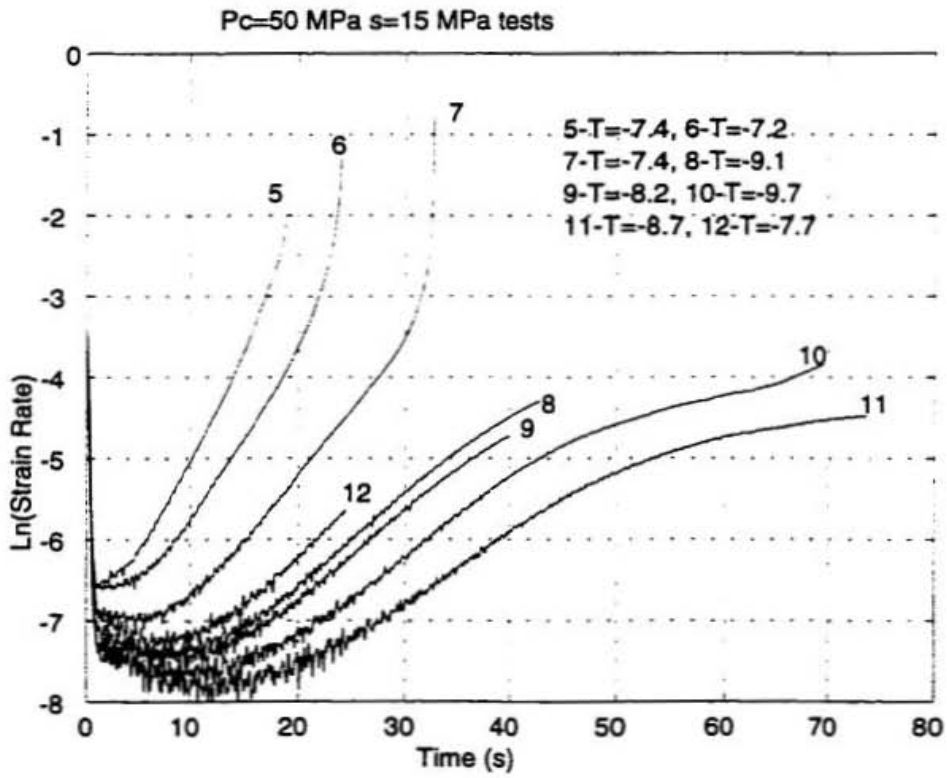

Figure 5.3 Plot of the logarithm of strain rate versus time for constant stress tests performed at p_c = 50 MPa.

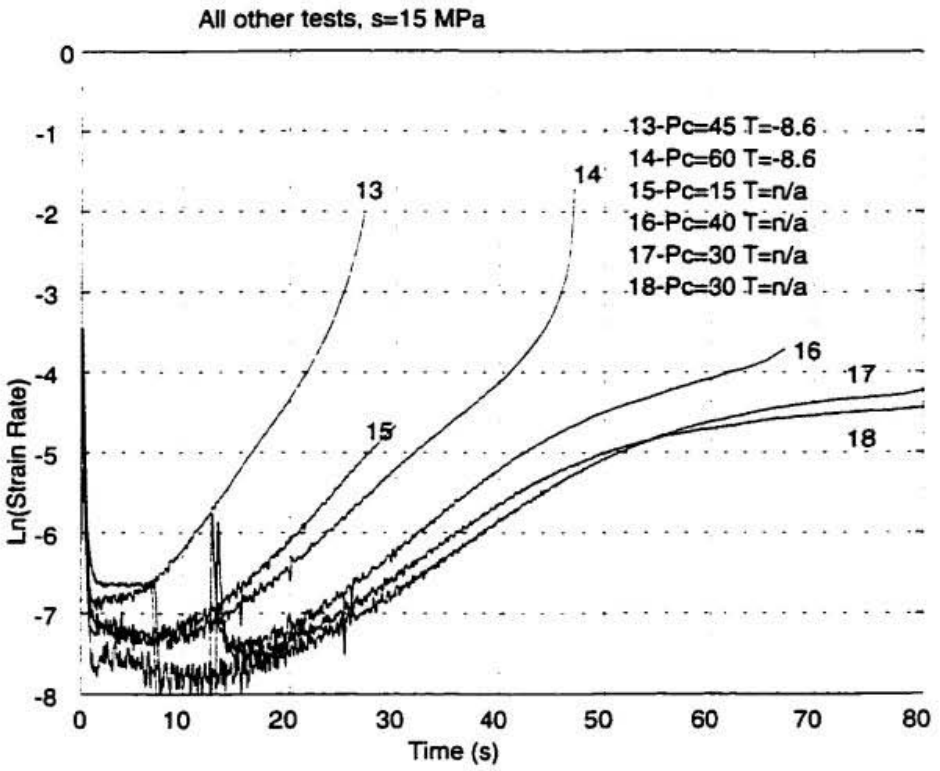

Figure 5.4 Plot of the logarithm of strain rate versus time for constant stress tests performed at all other confining pressures.

The logarithm of strain rate versus time curves were all corrected for lateral strain in the samples as described in the following section and in Section 3.4. The linear portion of the curves used in the calibration was determined by visual inspection of each plot. In general, the linear sections used were taken from the point where the logarithm of strain rate begins to accelerate after the initial minimum strain rate portion. A simple fit was performed on the linear sections of the curves to yield the slope, ϕ, and the intercept, I, following Equation 5.8.

5.2.2 Stress and Strain Rate Corrections

Lateral strain had a significant effect on the cross-sectional area of specimens deformed to high strain levels. Because the MTS testing apparatus maintained a constant axial load rather than a constant stress during testing, a correction was required to account for the decrease in stress with increasing area. The specimens were assumed to have strained uniformly over their entire length. The specimens were also assumed to have maintained a constant volume throughout the tests (i.e., no significant crack or void formation occurred). Both these assumptions are reasonable based on measurements and observations of the samples following testing. These issues are discussed previously in Section 3.4. In summary, the sample diameter was calculated from the displacement of the axial ram and the initial sample volume. This corrected diameter was then used to calculate the true instantaneous stress in the specimens at any point in time during the tests.

The correction to the stress resulted in a decrease in the actual stress within the specimens with increasing strain. As a result the calculated strain rate also required a correction in order to approximate the constant stress conditions required to calibrate the model. This was resolved by assuming a power dependence of creep rate on stress. Using Equation 5.6 for both the experimental and constant stress conditions (while neglecting damage as no damage function exists yet) yields:

$$\dot{e}_e = s_e^r k \tag{5.6a}$$

$$\dot{e}_{cs} = s_{cs}^r k \tag{5.6b}$$

Where the subscripts *e* and *cs* represent *experimental* data and data corrected for *constant stress*, respectively. Solving for *k* and combining gives:

$$\frac{\dot{e}_e}{s_e^r} = \frac{\dot{e}_{cs}}{s_{cs}^r} \tag{5.10}$$

which is based on the assumption that the value *k* from Equation 5.6 will remain constant

over varying stress levels. This step does not take into account the damage term e^S since the damage function $f(p)$ has yet to be resolved. This will be dealt with later and for now this simple correction will be used as a first iteration. Solving Equation 5.10 for the constant stress strain rate $\dot{e}_{cs}$ yields:

$$\dot{e}_{cs} = \dot{e}_e \left(\frac{s_{cs}}{s_e} \right)^r \tag{5.11}$$

The stress dependence r used in this first correction was $r = 4.2$. This power law dependence was obtained from a plot of the logarithm of true stress versus the logarithm of the strain, both being experimental values. The trend is outlined in Figure 5.5 for several strain levels. The data points represent the strain rate at each of 5, 10, 20, 30, 40, and 44% strain. Although the data seems scattered, best fit lines do show the stress dependence of the strain rate on stress for each level of strain. In this plot the value of r is

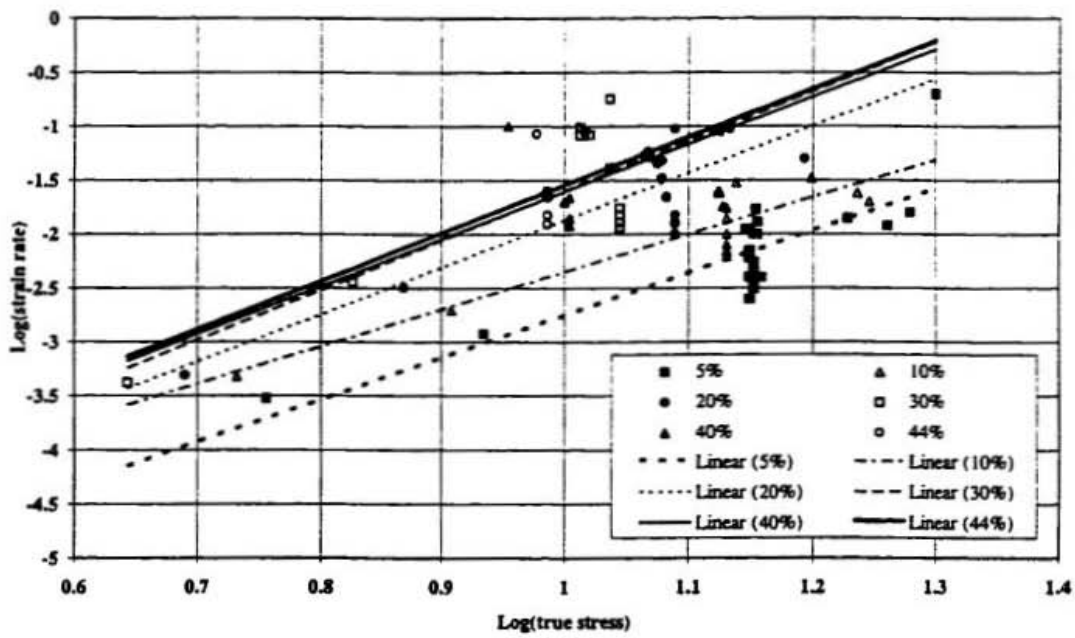

Figure 5.5 Plot of the logarithm of true strain rate versus the logarithm of true stress for all tests.

represented by the slope of the curve, as:

$$\dot{e} = k' s^{r} \tag{5.12}$$

where k' is a constant. Taking the logarithm (base 10) of both sides yields:

$$\log_{10}(\dot{e}) = \log_{10}(k') + r \log_{10}(s) \tag{5.13}$$

which corresponds to the log-log plot in Figure 5.5.

The result of the plot is that the exponent r seems to increase slightly with increasing strain levels. The average value of the slopes is 4.2 with a standard deviation of 0.4. A pressure dependence of the strain rate is also believed to be a factor. For the data presented in this study this plot suggests that the stress dependence (without considering damage) is actually greater than the typical value of $r = 3$ and nearer to $r = 4.2$ for large strains.

Since the damage function does not take part in the initial correction of the measured strain rate, the correction neglects a portion of the increase in the strain rate that can be attributed to the damage. This effect is small for small strains but becomes more significant as the strains become larger and the discrepancy between the experimental and constant stress increases. This is a direct result of damage measure being a function of the stress within the ice. In order to correct for this effect in the first iteration a second correction was performed on the data after the initial calibration of the damage model was performed.

The second iteration of the calibration was based on the following relation, similar to Equation 5.11:

$$\dot{e}_{cs} = \dot{e}_{e}\left(\frac{S_{cs}}{S_{e}}\right)^{r} \exp(S_{cs} - S_{e}) \tag{5.14}$$

where $r = 4.2$, and S_{cs} and S_{e} are the damage values based on Equation 5.3 for the constant stress and experimental data. The stresses used in Equation 5.3 were the

constant stress, s_{cs}, and experimental stress, s_e. These will also be used to determine the hydrostatic pressure p used in the pressure dependent relation $f(p)$ as: $p = p_c + \frac{s}{3}$.

The correction for the effect of the lateral strain on stress tended to linearise the curves of the logarithm of strain rate versus time. This can be seen in the corrected constant stress curves plotted for comparison in Figures 5.6, 5.7, and 5.8. These curves all have an initial sudden drop in the strain rate to between -6 and -8 on the logarithmic scale. The drop corresponds to the first moments after loading the samples where the ram has made initial

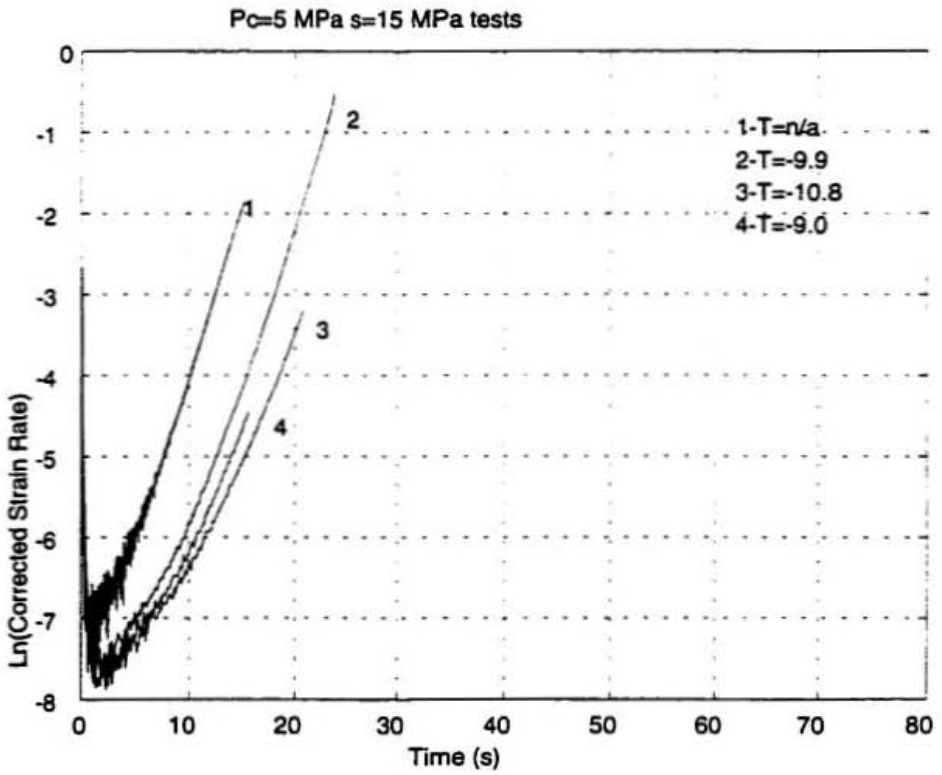

Figure 5.6 Plot of the logarithm of corrected strain rate versus time for constant stress tests performed at p_c = 5 MPa (corrected with r = 4.2).

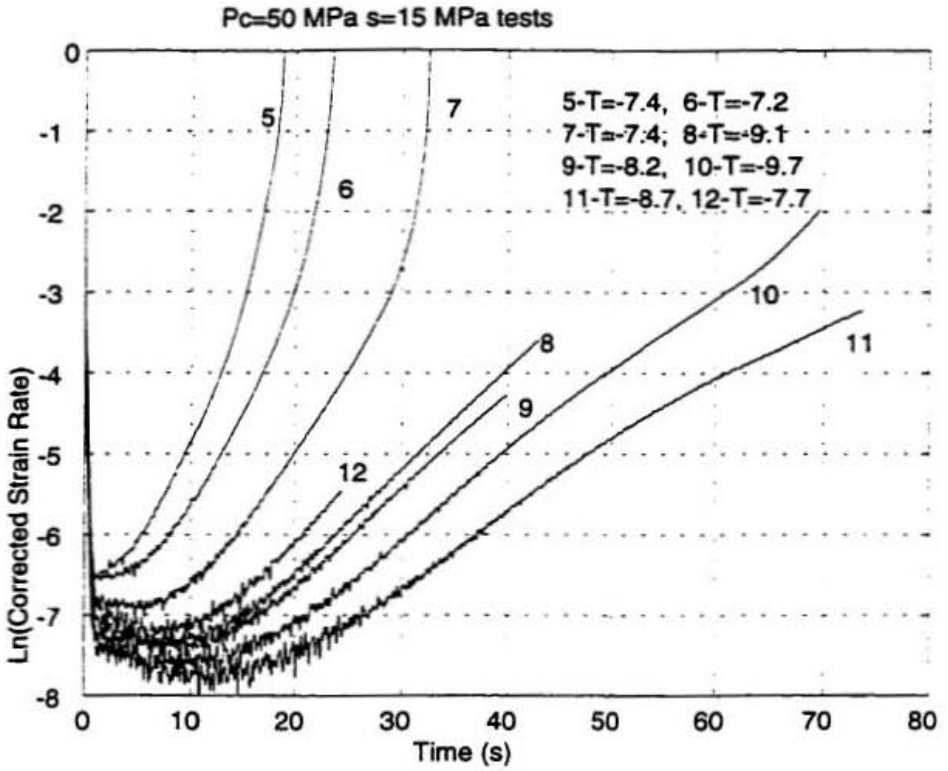

Figure 5.7 Plot of the logarithm of corrected strain rate versus time for constant stress tests performed at p_c = 50 MPa (corrected with r = 4.2).

contact. It is not unexpected to see a drop in the strain rate at this point as the ice deforms elastically and begins to creep. This loading step takes less than one second.

The curves then level off reaching a minimum creep rate within the first 15 seconds of loading. This period of near constant strain rate (encompassing the minimum strain rate) correlates to the reduction of the Burgers body and the accumulation of damage in the ice as described in Section 5.1. It is interesting that the time to minimum creep varies within constant pressure tests (Figure 5.6), some tests reaching tertiary creep almost instantly and others needing up to 15 seconds. This effect may be the result of

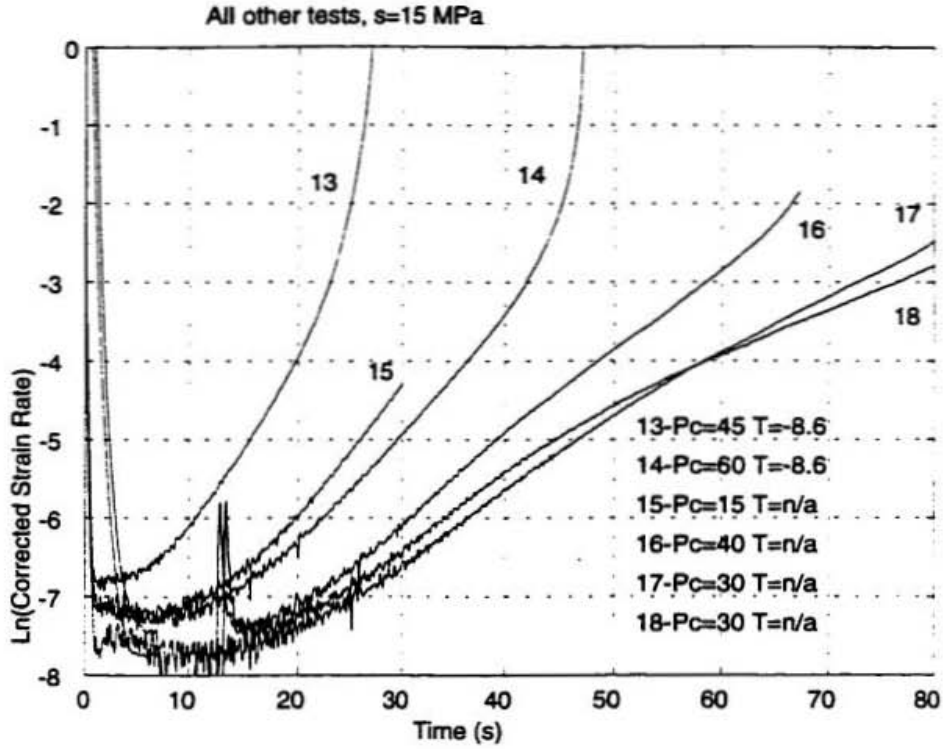

Figure 5.8 Plot of the logarithm of corrected strain rate versus time for constant stress tests performed at all other confining pressures. (corrected with $r = 4.2$).

temperature fluctuations and small difference in the virgin ice structure such as grain size, distribution, and c-axis orientation. The strains associated with these parts of the curves are minimal, a function of the low strain rates in this zone. These sections of the curves only seem to delay the inevitable onset of tertiary creep in the ice samples.

Following the minimum creep rate portion of the plots the curves begin to rise and enter the linear regime used in the calibration of the model. The sections of the curves which follow the linear portion were either less or more steep with no significant correlation to temperature or other parameters. This is not readily explainable except for a few samples which ruptured; the rupture being responsible for the runaway creep and

rapidly increasing strain rate (Section 4.3.3). The acceleration of these tests (tests #5, 6, and 7 in particular) could be explained by the failure of samples and the rapid advance of the ram. As far as the model is concerned these are considered to be on the edge of the useful range of the relation described here.

Having described the procedure and relations involved, a summary of the steps used to calibrate the model are outlined:

1. The stress data was corrected for the increasing cross sectional area caused by lateral strain.
2. The strain rate data was corrected based on the non-linear dependence of strain rate on stress ($r = 4.2$), obtained experimentally.
3. A set of initial damage model parameters was obtained for the corrected data.
4. The damage model parameters were then used along with the non-linear stress dependence ($r = 4.2$) to correct the raw data once again.
5. A final set of model parameters was obtained by calibrating with the final set of corrected curves.

5.2.3 First Calibration of the Model with Data Corrected for Stress

5.2.3.1 Calibrating for the Slope (ϕ)

Figure 5.9 shows the values of ϕ computed for all tests at various pressures and the relationship that will be calibrated into the model. The data points, although showing scatter or variability, generally define a trend. The points show a minimum slope value within the 30 to 40 MPa region with higher values for the high and low pressure zones. This minimum will serve as the point of inflection or transition point (p_{tr}), where two separate functions defining the relation on either side will meet and overlap. The

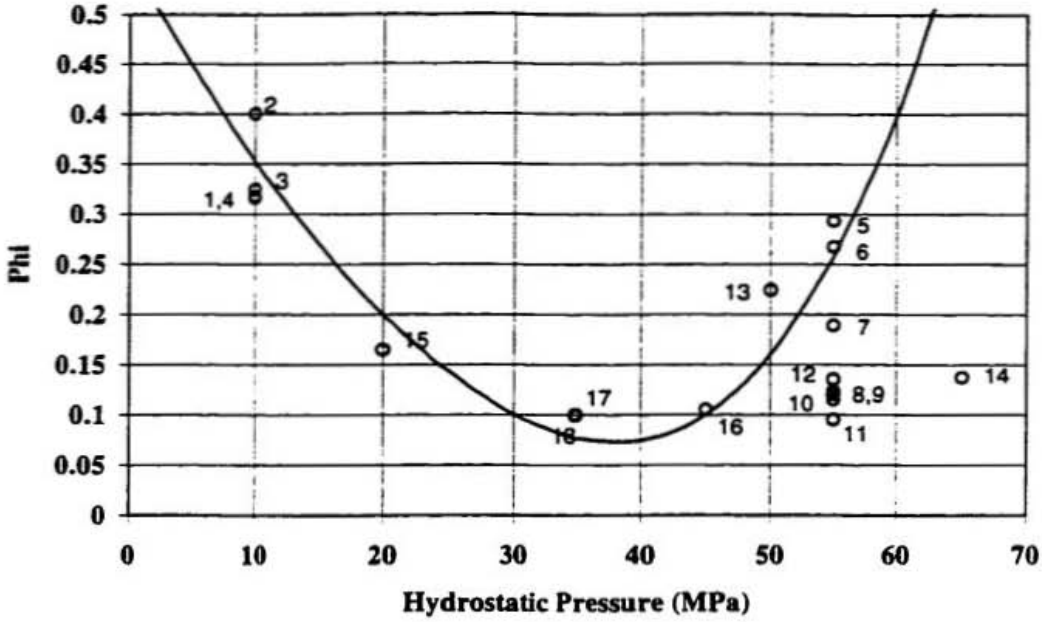

Figure 5.9 Phi (ϕ) plotted against hydrostatic pressure (p) for uncorrected data (using $r = 4.2$).

functions were developed into a state variable approach for quantifying damage and were incorporated into the damage function by the relations:

$$f_1(p) = a_1\left(1 - \frac{p}{p_1}\right)^m \text{ when } p \le p_{tr} \tag{5.15}$$

and:

$$f_2(p) = a_2\left(\frac{p}{p_2}\right)^n \tag{5.16}$$

where a_1, a_2, p_1 and p_2 are constants, p_{tr} is the transition pressure, and m and n are also constants.

Compression is taken as positive for both functions above. The combined effect of the two pressure-dependent processes is described by an integrated damage measure which replaces Equation 5.5, but is similar in form:

$$S = \int_0^t [f_1(p) + f_2(p)] \left(\frac{s}{s_0} \right)^q dt \tag{5.17}$$

where s_0 = 15 MPa and q = 5.

The use of separate functions for the two parts of the damage curve is a useful tool that may make analysis and changes to the model simpler in the future (Jordaan and others, 1997). For example, if further testing suggests separate stress dependencies for each zone of pressure, this could easily be incorporated into the damage formulation. The two zones of pressure are also believed to be operating under two very different microstructural regimes as discussed in Chapter 4. The first is within the low pressure zone which undergoes microfracturing and shear banding, followed by recrystallisation. The second appears at high pressures and is characterised by possible pressure melting, grain boundary migration, and more intense recrystallisation. In this range there is a marked change in the fabric of the ice as softening continues. Since there is no clear boundary between the two zones, the model parameters were developed to overlap the ranges eventually reaching zero as the functions pass the transition pressure. This is shown in Figure 5.10 as both functions are plotted separately.

The first part of the curve was approximated by using a parabolic function up to the transition pressure:

$$f_1(p) = \begin{cases} 0.55 \left(1 - \frac{p}{50} \right)^2 & \text{if } p \le 50 MPa \\ 0 & \text{if } p > 50 MPa \end{cases} \tag{5.18}$$

The second part of the curve was described by a power function:

$$f_2(p) = 0.16\left(\frac{p}{50}\right)^5 \tag{5.19}$$

The size of the exponent in Equation 5.19 ($m = 5$) is still under consideration, but is believed to be within the range of 3 to 7.

The curves in Figure 5.10 were calibrated using an intuitive method. This essentially allowed more weight to be allotted to specific data points based on their relevance to the data set. This was partially based on qualitative experimental issues which are not completely reflected in the data. Rapid acceleration into higher strain rate regimes by the samples must be considered in order to justify the acceleration of the slope versus pressure curve from Figure 5.9. For example Figure 5.7 shows that the high pressure

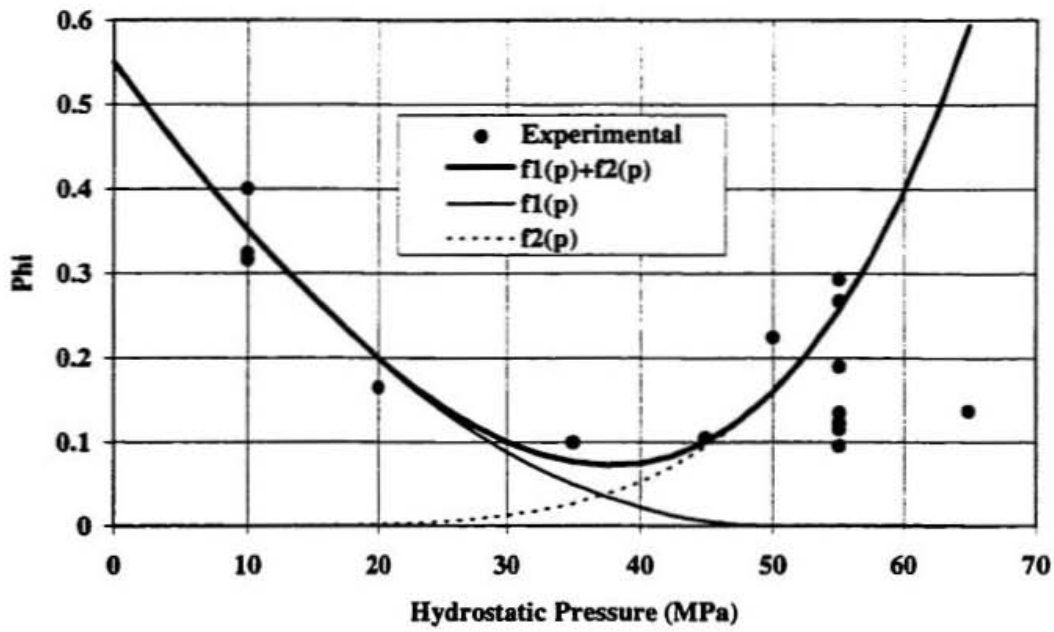

Figure 5.10 The two pressure dependent terms of the damage function, $f_1(p)$ and $f_2(p)$, plotted and summed to show the resultant function $f(p)$.

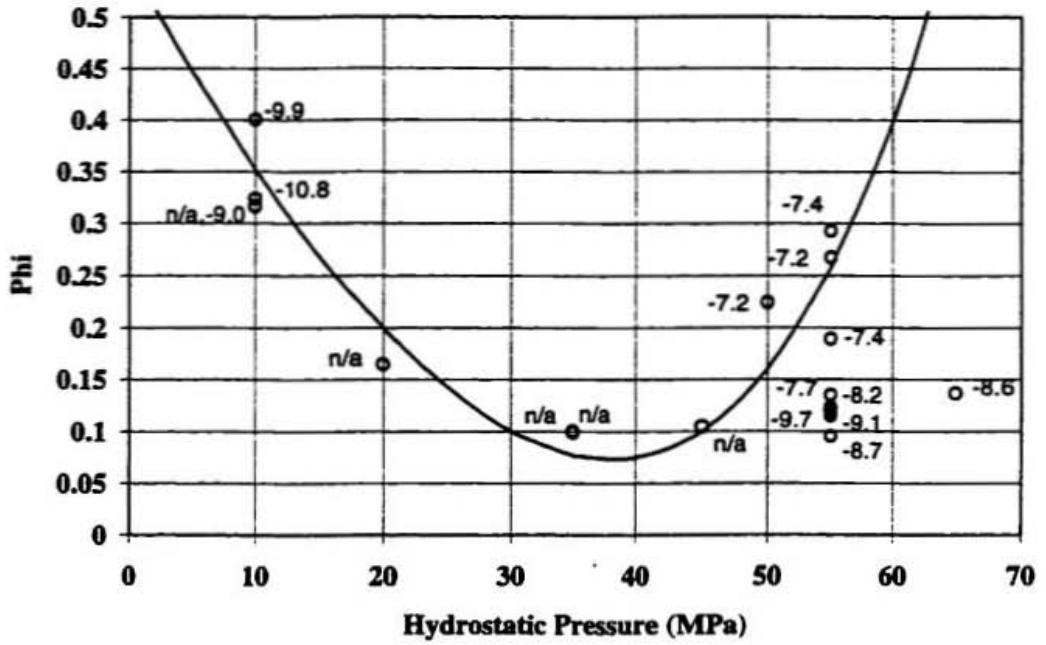

Figure 5.11 Phi (ϕ) plotted against hydrostatic pressure (p) with temperature data shown for reference (corrected with $r = 4.2$).

tests showed signs of dramatically increasing strain rates during testing. On the other hand the testing at the mid-range (Figure 5.8) shows how slope decreased slightly but consistently over the creep tests. Factors such as these and an intuitive knowledge of the expected reaction past the range of tests performed in this study leads the fifth order power function used in the calibration and the fact that some of the data points were treated with less influence than others.

5.2.3.2 Temperature Effects

As discussed previously in Chapter 4 the strain rate is also dependent on temperature. The values of ϕ are plotted once again in Figure 5.11, distinguished by the approximate temperature at the start of the load step. In some cases no temperature was available.

The scatter in the results represents some of the problems encountered in maintaining a consistent temperature throughout this test series. Further testing will certainly be required to calibrate the model with respect to temperature. The data does suggest that temperature effects are quite pronounced at high pressures; this observation is consistent with the interpretation that large scale recrystallization and possible pressure melting are the dominant creep mechanisms at high pressure. There is insufficient data at this point to evaluate the sensitivity of strain rate on temperature at low to moderate pressures. Temperature is thought to be a factor in the rupture of some of the samples tested as discussed in Section 4.3.

5.2.4 Second Calibration of the Model with Corrected Data

5.2.4.1 Recalibrating for the Slope (ϕ)

The procedure for the second calibration was the same as for the initial calibration presented in Section 5.2.3.1. The curves used in this section are shown in Figures 5.12, 5.13, and 5.14. These curves represent data corrected with Equation 5.14 and will be used to determine a more precise form of the pressure-dependent damage parameters used in the model. In general the curves have the same form as the uncorrected curves (Figures 5.6, 5.7, and 5.8) with an increase in the logarithm of strain rate at the tail. The resulting slopes obtained from these curves are shown in Figure 5.15 plotted against the hydrostatic pressure. The calibrated curve for the model is shown fit to the data. The calibration was performed in the same manner as the previous initial calibration where the slope of the linear portion of each curve was determined and plotted against the hydrostatic pressure. The resulting parameters were determined to be as follows:

$$f_1(p) = 0.68\left(1 - \frac{p}{47}\right)^2 \qquad \text{when } p \le 47 \text{ MPa} \tag{5.20}$$

and

$$f_2(p) = 0.18\left(\frac{p}{47}\right)^5 \tag{5.21}$$

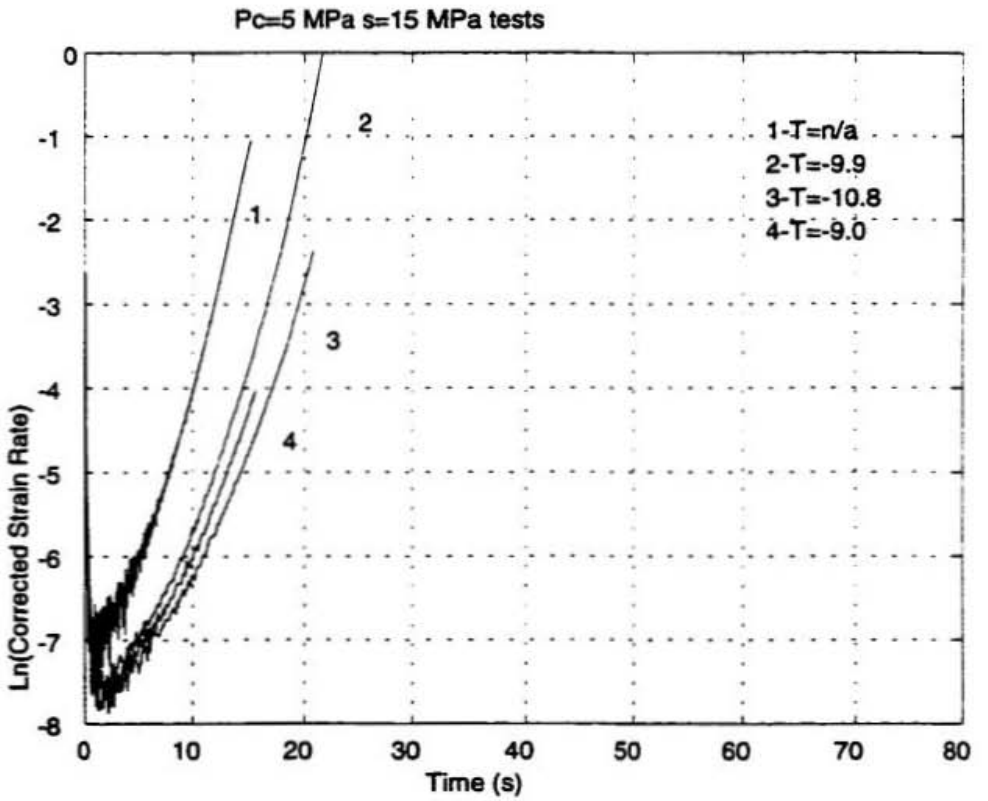

Figure 5.12 Plot of the logarithm of corrected strain rate versus time for constant stress tests performed at p_c = 5 MPa (corrected with damage function and r = 4.2).

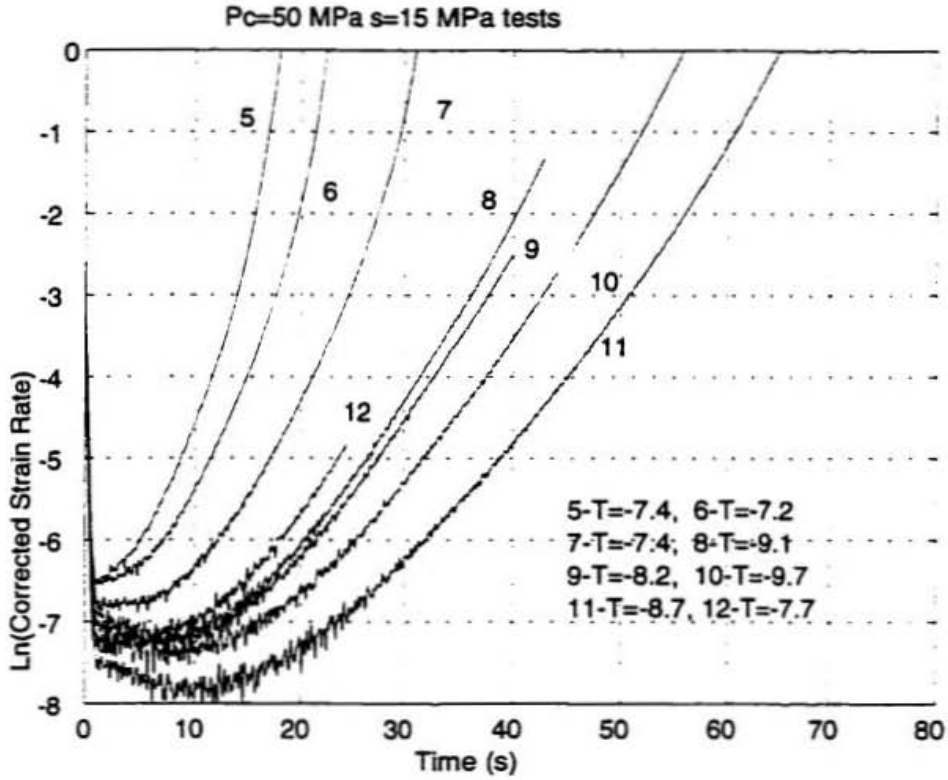

Figure 5.13 Plot of the logarithm of corrected strain rate versus time for constant stress tests performed at $p_c = 50$ MPa (corrected with damage function and $r = 4.2$).

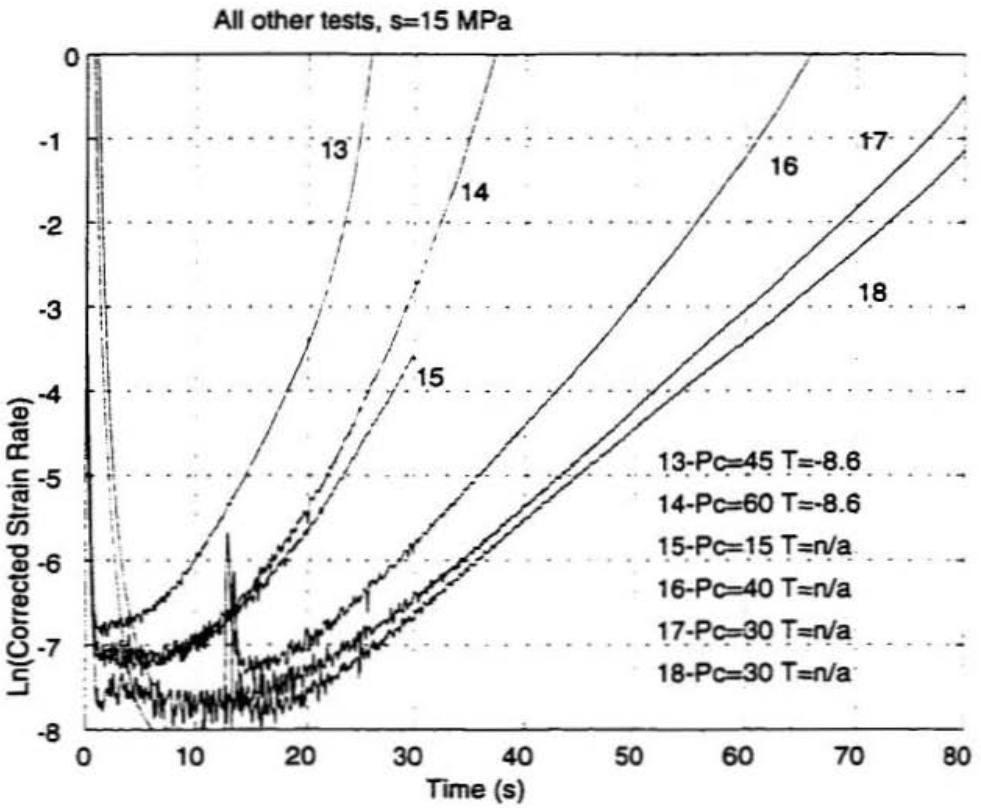

Figure 5.14 Plot of the logarithm of corrected strain rate versus time for constant stress tests performed at all other confining pressures (corrected with damage function and $r = 4.2$).

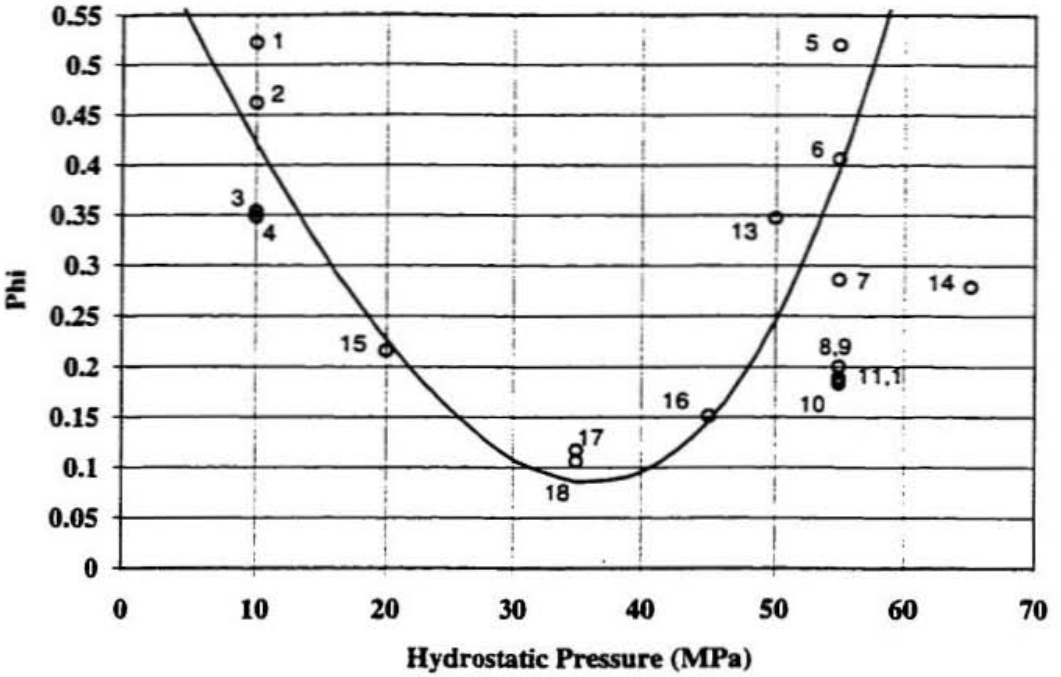

Figure 5.15 Slope (phi, ϕ) plotted versus hydrostatic pressure (p) for data corrected with the damage function and $r = 4.2$.

5.2.4.2 Calibrating the Intercept (I)

The pressure-dependent constitutive model was initially developed for use within a finite element program where a damaged layer was assumed to be already established and did not need to be developed (Jordaan and others, 1997). For this reason the initial model developed for this work relied only on the linear portion of the logarithm of strain rate curves and not the intercept which defines the initial strain rate within the model. In this analysis the intercept relation has to be determined for the model to be set up as a stand-alone formulation to be used to predict sample behaviour under laboratory conditions.

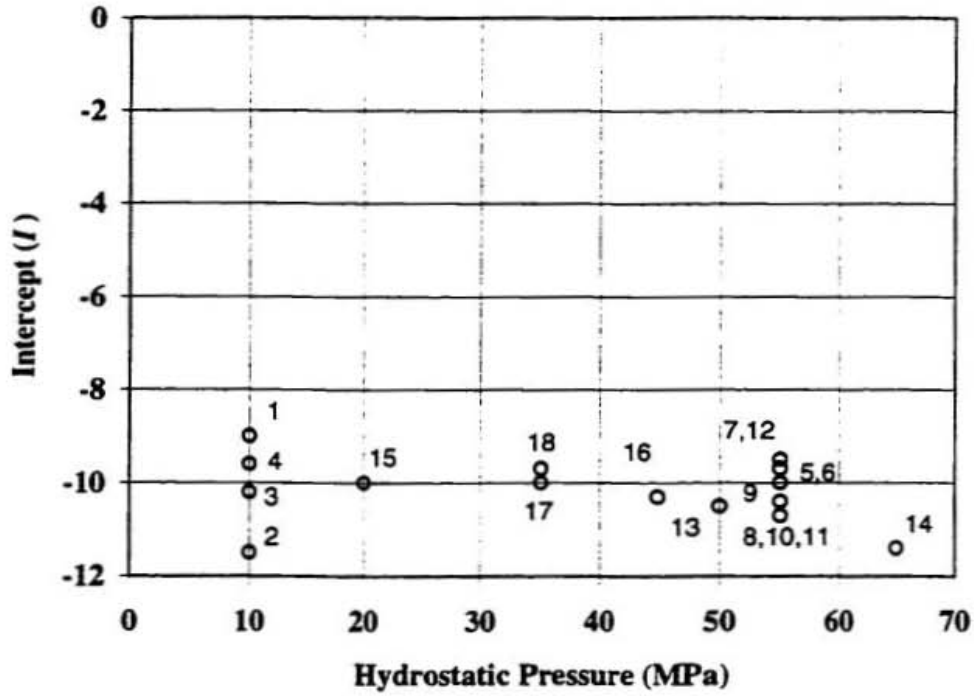

Figure 5.16 Intercept (I) plotted versus hydrostatic pressure (p) for data corrected with the damage function and $r = 4.2$.

For the intercept of the present model (where the data is shown plotted against pressure in Figure 5.16) the use of a relation like the one used for the slope of the logarithm of strain rate versus time was discarded and a simple average value was used. The intercept values had a standard deviation of 0.64 over the entire pressure range (0 to 65 MPa) and the average value was -10.22. Solving Equation 5.9 for k yields the following relation based on the intercept I, the stress s, and the non-linearity constant r:

$$k = e^{I} s^{-r} \tag{5.22}$$

The damage enhancement component is omitted in Equation 5.22 as time is taken at $t = 0$, where the damage term becomes unity ($S = 1$). Solving the equation with the average

value of I = -10.22 along with the other constants r = 4.2 and s = 15 MPa, the result is $k = 4.19\times10^{-10}$.

5.3 The Calibrated Model

The calibrated model is defined below by Equations 5.6, 5.12, 5.13 and 5.14. The parameters for the set of equations are outlined in Table 5.2.

$$\dot{e} = e^{S} s^{r} k \tag{5.6}$$

$$f_1(p) = a_1\left(1-\frac{p}{p_1}\right)^{m} \quad \text{when } p \le p_{cr} \tag{5.15}$$

$$f_2(p) = a_2\left(\frac{p}{p_2}\right)^{n} \tag{5.16}$$

$$S = \int_0^t \left[f_1(p)+f_2(p)\right]\left(\frac{s}{s_0}\right)^{q} dt \tag{5.17}$$

Table 5.2 Calibrated model parameters for the pressure-dependent constitutive model.

Parameter	Description	Value	Units
a_1	damage function constant	0.68	
p_1	reference pressure	47	MPa
m	low pressure exponent	2	
a_2	damage function constant	0.18	
p_2	reference pressure	47	MPa
n	high pressure exponent	5	
q	damage function exponent	5	
s_0	reference stress	15	MPa
r	stress non-linearity exponent	4.2	
k	reference strain rate	4.19×10^{-10}	s^{-1}

5.4 Results of Modelling

The calibrated model was compared with collected data from triaxial testing. Two sets of data were compared against the model predictions. The first was the creep test data used to calibrate the model, the second a comparison with experimental data from creep tests performed on damaged ice.

The model runs performed used the corrected stress from the data to quantify the damage using the two pressure dependent damage terms (Equations 5.15 and 5.16) that are summed in the damage integral (Equation 5.17). The damage was then used in Equation 5.6 to yield the strain rate expected at any given time t. The strain rate was then integrated numerically to yield the strain in the ice sample, also for any given time t. The constant load tests used in the calibration were then plotted along with the response predicted by the model for each of three confining pressures: p_c = 5, 30 and 50 MPa. These plots are shown in Figures 5.17, 5.18, and 5.19.

Figure 5.17 shows the actual strain response of the ice compared with the output of the model for a confining pressure of p_c = 5 MPa and a nominal differential stress of 15 MPa. In this case the model falls short of predicting the rapid acceleration observed in these test results. The difference can be associated with two different observations. The fact that the model calibration in this range is only based on a few data points, two of which were for tests of short duration where the strains reached were only small, will lead to inadequacies in modelling. The second point is that the intercept calibration for the model was relatively simple and may not represent the slight variations in the intercept at this pressure. The intercept represents the initial strain rate that is observed in the tests beyond the minimum strain rate. The curve does seem to have the same general shape as the collected data, specifically as time increases, implying that the initial strain rate may be too low at low pressure in this iteration of the calibration.

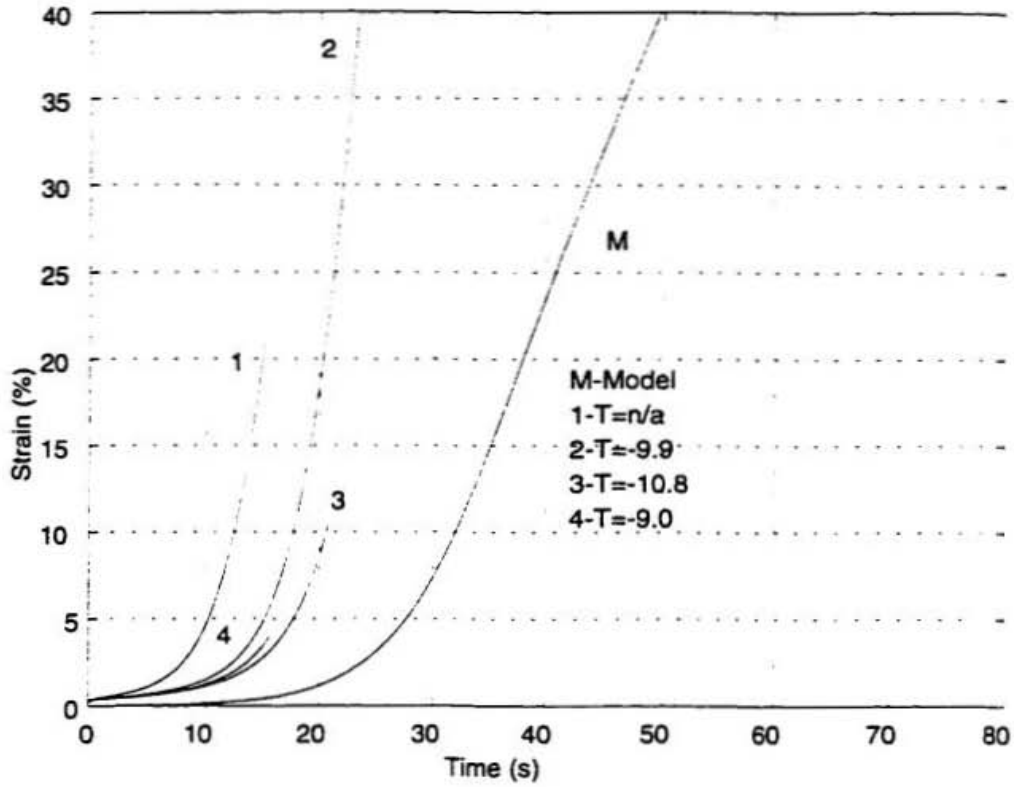

Figure 5.17 Model results compared to actual creep test data at $s = 15$ MPa and $p_c = 5$ MPa.

A better fit of the model to the constant stress data is seen in Figure 5.18 where the response of the ice at a confinement of 30 MPa and nominal differential stress of 15 MPa is shown. In this case the model still fell short of the prediction and also had a curve that was similar in shape to the experimental results. The discrepancy is expected in this case as the calibration of the data points at this confinement was low. This can be seen in Figure 5.15 as points 17 and 18 are higher than the calibrated curve.

In Figure 5.19 the confining pressure is 50 MPa and the differential stress is still 15 MPa. In this case the model prediction is in the mid-range of all the tests, representing a

type of average result of all tests. The scatter in this set is significant and does leave the validity of the model in question. Clearly the ice tested in the laboratory is behaving differently under what are considered to be similar conditions. Reiterating a point that has been expressed previously, the temperature, which has not been incorporated into this model, is probably a factor in this relationship.

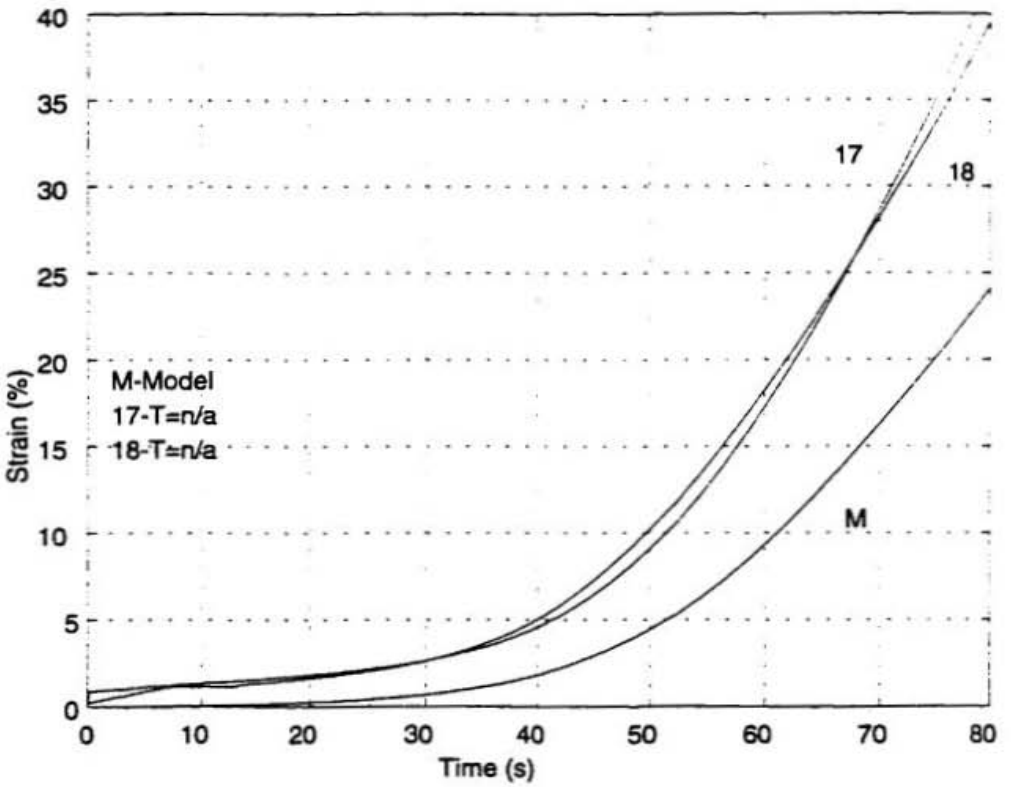

Figure 5.18 Model results compared to actual creep test data at s = 15 MPa and p_c = 30 MPa.

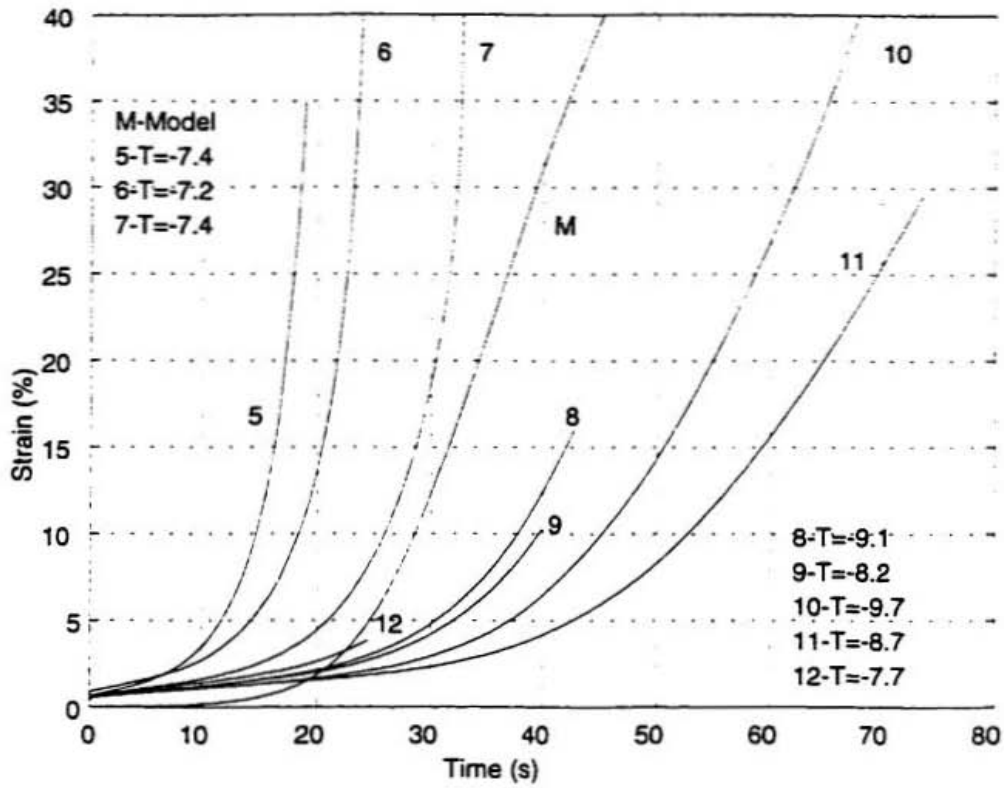

Figure 5.19 Model results compared to actual creep test data at s = 15 MPa and p_c = 50 MPa.

Moving on to modelling the creep response of damaged ice, Figure 5.20 represents the comparison of the model against data collected from tests damaged at two different nominal strain rates up to 12.8% strain and then loaded triaxially with 15, 30 or 50 MPa of confinement and a differential stress of 15 MPa. In these plots the initial damage value in the model was set at the calculated damage value for each individual test. This was obtained by running the model using the corrected stress from the constant strain rate damage step as an input. The result was a cumulative value of damage for the material

over the duration of the test. The damage was evaluated for the end of the 12.8% damage step and used in the model prediction as the initial damage during a constant stress test.

The curves in Figure 5.20 show a dramatic set of predictions from the model. In general it can be observed that the model does not predict very well the behaviour of previously damaged ice damaged at constant strain rate. Specifically the model tends to underpredict the response in every case.

Figure 5.20a represents constant stress tests at p_c = 15 MPa with a differential stress of 15 MPa. The result shows that the model for the ice damaged at 10^{-2} s^{-1} does follow the experimental results initially but quickly falls behind in predicting the response for higher strain levels beyond 10 s. The predicted curve for the ice damaged at 10^{-4} s^{-1} does not model the response adequately at any stage.

At the next confining pressure of 30 MPa, the results are also similar. The prediction based on ice damaged at 10^{-2} s^{-1} tends to vary from the experimental by the time the curve reaches 15 s, while the prediction for the ice damaged at 10^{-4} s^{-1} is very low. In Figure 5.20c a similar result is also observed. It is clear that the model is inadequate for quantifying damage in ice tested at 10^{-4} s^{-1} but does begin to model the constant stress response of ice damaged at 10^{-2} s^{-1}.

The result of the model predictions for damaged ice clearly displays the limitations of this model as calibrated to predict the response of ice under these conditions. The result is related to the way in which the model was calibrated, using constant stress data. Clearly a more rigorous calibration with constant strain rate data may yield a model particularly suited for this application. It remains to be seen at this point, however clearly more testing and refinement of the model is required.

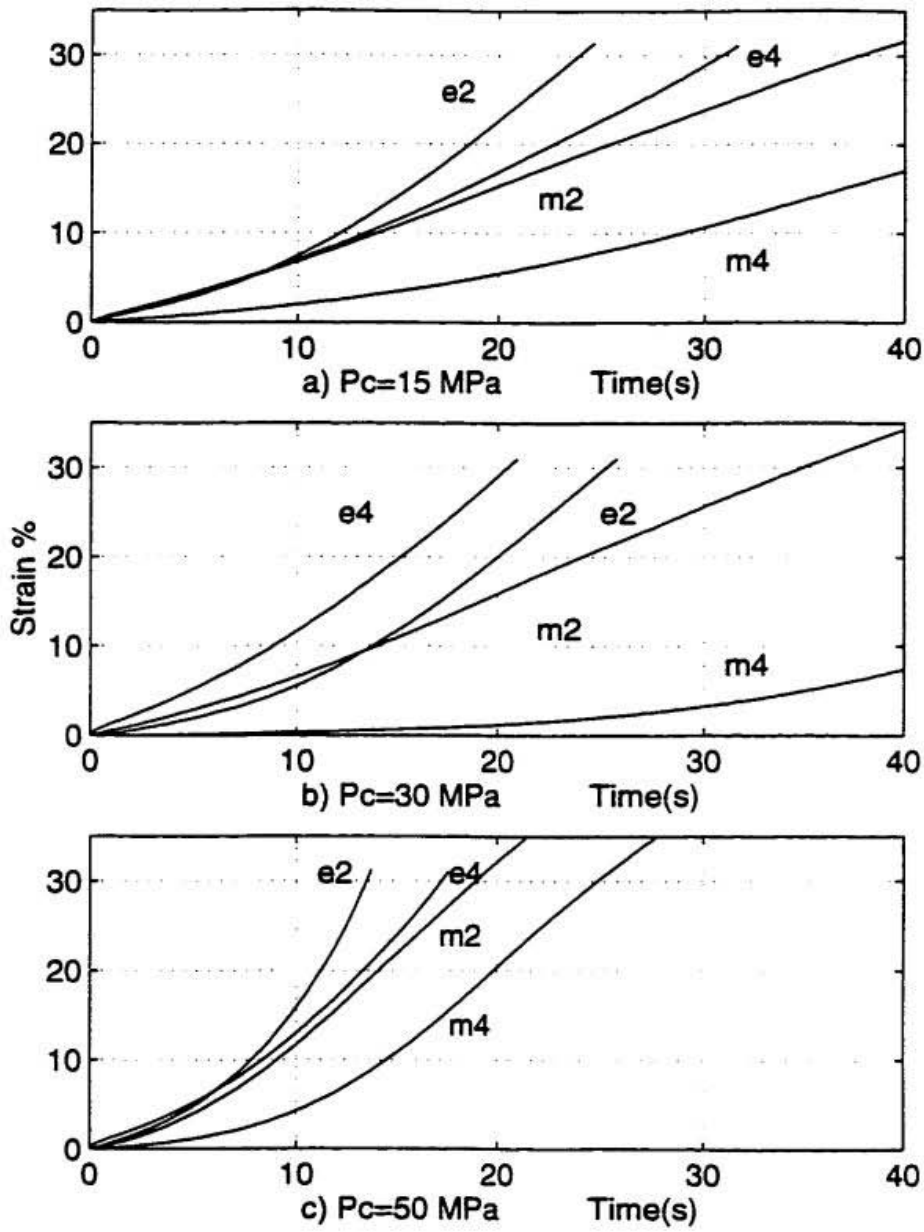

Figure 5.20 Model results compared to constant load tests on damaged ice with different pressures during the creep step The *e* represents experimental and the *m* model predictions, while the number in the labels indicates the damage rate (2 is 10^{-2} s^{-1} and 4 is 10^{-4} s^{-1}).

Chapter 6

Concluding Remarks and Recommendations

6.1 Concluding Remarks

Qualitative and quantitative results from the triaxial testing performed in this study show the existence of two different by interlaced regimes of deformation mechanisms. In all cases a general reduction in grain size was observed with increasing strain. Cracking and recrystallisation were observed as the primary forms of microstructural change at low pressure while recrystallisation and pressure melting were more apparent at higher confining pressures. This observation was the motivation for the pressure-dependent constitutive model which was defined by two separate pressure-dependent damage functions.

The pressure dependent constitutive model for granular ice developed by Jordaan and others (1997) and calibrated in this study with additional triaxial test data was not found to agree very well with data from tests where damaged ice was subjected to constant load tests. It is believed that more work along with a more thorough set of triaxial testing

could lead to a better calibration. Predictions based on both constant stress tests on undamaged and damaged ice show shortcomings of the present calibration. A more complex relation which would take into account more parameters may be part of the solution. The shortcomings of the model to predict damage levels in ice damaged at constant strain rates is apparent but not unexpected.

6.2 Recommendations

Recommendations for further study could be very broad when one considers the scope of work that could be done before a truly good understanding of the response of ice under all possible conditions is obtained. Parameters such as temperature, grain size, pressure, differential stress, and strain rate could all be the focus of significant studies into the deformation and mechanical behaviour of ice. In the field of constitutive modelling, specifically for the pressure-dependent model presented here, more testing is needed for calibration and verification of model parameters. Testing should be directed at repeating some of the tests presented here, especially at high and low confinement, as well as expanding the test matrix to include other differential stresses. Once some of these and the following recommendations have been addressed, the resulting model will be in a better position to be incorporated into a finite element analysis of ice structure interaction.

Specific recommendations for study into this topic in the future are presented below:

1. A set of triaxial tests on granular ice overlapping and repeating the present set where pressure is varied in order to isolate the pressure effects of the ice should be performed to give a greater data set from which to base calibrations.
2. Better temperature control or monitoring must be put into place and a set of tests performed (particularly tests of a triaxial nature where pressure melting is an issue). This is in order to either eliminate the possible irregularities encountered

in this study with respect to temperature or incorporate a means of studying the temperature effects properly.

3. The implementation of true constant stress control is needed. This would eliminate a large part of the uncertainty in this study by eliminating the difference between calculated and actual stress. In this situation the collected data would no longer require correction.
4. A study into the non-linear stress dependence of the strain rate would useful in helping to clarify parameters used in the corrections and calibrations.

References

Barrette, P., (1997) C-CORE, Personal communication (e-mail), December 3rd, 1997.

Biot, M.A., (1954) Theory of stress-strain relations in anisotropic viscoelasticity and relaxation phenomena. Journal of Applied Physics, Vol. 25, No. 11, pp. 1385-1391.

Budiansky, B., and O'Connell, R.J., (1976) Elastic moduli of a cracked solid. Int. J. Solids Struct., Vol. 12, pp. 81-97.

Cole, D.M., (1983) The relationship between creep and strength behavior of ice at failure, Cold Regions Science and Technology, Vol. 8, pp. 189-197.

Cole, D.M., (1986) Effect of grain size on the internal fracturing of polycrystalline ice. USA Cold Regions Research and Engineering Laboratory, CRREL Report 86-5.

Cole, D.M., (1987) Strain-rate and grain-size effects in ice. Journal of Glaciology, Vol. 33, No. 115, pp. 274-280.

Deiter, G.E., (1976) Mechanical Metallurgy, New York, McGraw-Hill.

Frederking, R.M.W., Jordaan, I.J., and McCallum, J.S., (1990) Field tests of ice indentation at medium scale: Hobson's choice ice island, 1989. Proceedings, 10th International Symposium on Ice, 2, IAHR, Espoo, Finland, pp. 931-944.

Frost, H.J., and Ashby, M.F., (1982) Chapter 2-Rate equations, deformation-mechanism maps, the Plasticity and Creep of Metals and Ceramics, Pergamon Press, Willowdale, Ontario.

Gagnon, R.E., and Gammon, P.H., (1995) Triaxial experiments on iceberg and glacier ice, Journal of Glaciology, Vol. 41, pp. 528-540.

Glen, I.F., and Blount, H., (1984) Measurement of ice impact pressures and loads on board the C.C.G.S. Louis S. St. Laurent. Proceedings of the OMAE, New Orleans, Vol. 3, pp. 246-252.

Glen, J.W., and Ives, D.J., (1988) Fish antifreeze proteins and the creep of polycrystalline ice. Journal of Glaciology, Vol. 34, No. 118, pp. 291-292.

Hobbs, P.V., (1974) Ice Physics, Clarendon Press, Oxford

Horii, H., and Nemat-Naser, S., (1983) Overall moduli of solids with microcracks: load-induced anisotropy. J. Mech. Phys. Solids., Vol. 31, No. 2, pp. 155-171.

Jacka, T.H., and Li, J., (1994) The steady-state crystal size of deforming ice. Annals of Glaciology, Vol. 20, pp. 13-18.

Jacka, T.H., and Maccagnan, M., (1984) Ice crystallographic and strain rate changes with strain in compression and extension. Cold Regions Science and Technology, Vol. 8, pp. 269-286.

Johnston, M., Croasdale, K. R., and Jordaan, I.J., (1995) Localized pressure during ice-structure interaction: relevance to design criteria. In Canadian Offshore Design for Ice Environments, Volume 3, Local and global ice loads, Memorial University of Newfoundland, St. John's. NF.

Jones, S.J., (1982) The confined compressive strength of polycrystalline ice. Journal of Glaciology, Vol. 28, No. 98, pp. 171-177.

Jordaan , I.J., Matskevitch, D.G., and Meglis, I.L., (1997) Disintegration of ice under fast compressive loading. Accepted for publication.

Jordaan, I.J., and McKenna, R.F., (1988) Modelling and progressive damage in ice. Proceedings IAHR Symposium on Ice, Sapporo, Japan, Vol. 2, pp. 585-624.

Jordaan, I.J., and McKenna, R.F., (1989) Process of deformation and fracture of ice in compression. Proceedings IUTAM/IAHR Symposium on Ice-structure Interaction, St. John's, NF, pp. 283-310.

Jordaan, I.J. and Xiao, J., (1992) Interplay between damage and fracture in ice-structure interaction. Proceedings of the 11th International Symposium on Ice, Alberta, Canada, pp. 1448-1467.

Jordaan, I.J., and Singh, S.K., (1994) Compressive ice failure: Critical zones of high pressure. IAHR Ice Symposium, Tronheim, Norway.

Jordaan, I.J., Kennedy, K.P., McKenna, R.F., and Maes, M.A., (1991) Loads and vibration induced by compressive failure of ice, in Sodhi, D.S., ed. Cold Regions Engineering, Proceedings of the 6th International Speciality Conference, February 26-28, 1991, West London, NH. New York, American Society of Civil Engineers, pp. 638-649.

Jordaan, I.J., Stone, B.M., McKenna, R.F., and Fuglem, M.K., (1992) Effect of microcracking on the deformation of ice. Canadian Geotechnical Journal, 29, pp. 143-150.

Kachanov, L.M., (1958) On creep rupture time. Izv. Acad. Nauk SSSR, Otd. Techn. Nauk, No. 8, pp. 26-31.

Kachanov, M., (1993) Elastic solids with many cracks and related problems. Advances in Applied Mechanics, Vol. 30, Academic Press.

Kalifa, P., Ouillon, G., and Duval, P., (1992) Microcracking and the failure of polycrystalline ice under triaxial compression. Journal of Glaciology, Vol. 38, No. 128, pp. 65-76.

Karr, D.G., and Choi, K., (1989) A three-dimensional constitutive damage model for polycrystalline ice. Mech. Mater., Vol. 8, pp. 55-66.

McKenna, R.F., Meyssonnier, J., and Jordaan, I.J., (1989) Peak pressures from a damage model for ice in compression. Proceedings of the Eighth International Conference on Offshore Mechanics and Arctic Engineering, the Hague, Netherlands, Vol. IV, pp. 67-73.

Meaney, R., Kenny, S., and Sinha, N.K., (1991) Medium-scale ice-structure interaction: Failure zone characterization. 11th Conference on Port and Ocean Engineering under Arctic Conditions, 1991, St. John's, NF, Vol. 1, pp. 126-140.

Meglis, I.L., Melanson, P.M., and Jordaan, I.J., (1998). Microstructural change in ice 1h: II. Constant-load creep behaviour under triaxial stress conditions (submitted for publication).

Melanson, P.M., Meglis, I.L., and Jordaan, I.J., (1998). Microstructural change in ice Ih: I. Constant deformation rate tests under triaxial stress conditions (submitted for publication).

Mellor, M., and Cole, D.M., (1982) Deformation and failure of ice under constant stress or constant strain-rate. Cold Regions Science and Technology, Vol. 5, pp. 201-219.

Mellor, M., and Cole, D.M., (1983) Stress/strain/time relations for ice under uniaxial compression, Cold Regions Science and Technology, Vol. 6, pp. 207-230.

Michel, B., and Ramseier, R.O., (1971) Classification of river and lake ice. Canadian Geotechnical Journal, Vol. 8, No. 36, pp. 36-45.

Nadreau, J.-P., and Michel, B., (1984) Ice properties in relation to ice forces. 2nd State-of-the-art IAHR Working Group on Ice Forces, Vol. 4, Hamburg

Nordell, B., (1990) Measurement of P-T coexistence curve for ice-water mixture. Cold regions Science and Technology, Vol. 19, pp. 83-88.

NEB, (1997) The failure of ice under impact conditions. report prepared for the National Energy Board, by OERC, MUN, St. John's, NF, March 28th, 1997.

Poirier, J.-P., (1985) Creep of crystals, high temperature deformation processes in metals, ceramics and minerals. Cambridge earth science series, Cambridge University Press.

Rist, M.A., and Murrell, S.A.F., (1994) Ice triaxial deformation and fracture. Journal of Glaciology, Vol. 40, No. 135, pp. 305-318.

Rist, M.A., Jones, S.J. and Slade, T.D., (1994) Microcracking and shear fracture in ice. Annals of Glaciology, Vol. 19, pp. 131-137.

Schapery, R.A., (1981) On viscoelasvtic deformation and failure behaviour of composite materials with distributed flaws. Advances in Aerospace Structures and Materials, The American Society of Mechanical Engineers.

Schapery, R.A., (1984) Correspondence principles and generalized J integral for large deformation and fracture analysis of viscoelastic media. International Journal of Fracture, Vol. 25, pp. 195-223.

Schapery, R.A., (1988) A theory of mechanical behaviour of elastic media with growing damage and other changes in structure. Mechanics and Materials Centre, Texas A and M University, College Station, Texas, Report No. MM. 5762-88-1.

Schapery, R.A., (1989) Models for the deformation viscoelastic media with distributed damage and their applicability to ice. Proceedings IUTAM/IAHR Symposium on Ice-Structure Interaction, St. John's, NF, pp. 191-230.

Schulson, E.M., and Cannon, N.P., (1984) The effect of grain size on the compressive strength of ice. IAHR Ice Symposium, Hamburg, pp. 29-38.

Singh, S.K., and Jordaan, I.J., (1996a) Triaxial tests on crushed ice. Cold Regions Science and Technology, Vol. 24, pp. 153-165.

Singh, S.K., and Jordaan, I.J., (1996b) Constitutive behaviour of crushed ice. Symposium on Inelasticity and Damage of Solids subject to Microstructural Change.

Singh, S.K., Jordaan, I.J., Xiao, J., and Spencer, P.A., (1993) The flow properties of crushed ice. Proceedings of the International Conference on Offshore Mechanics and Arctic Engineering Glasgow, UK, Vol. 4, pp. 11-19.

Sinha, N.K., (1978) Rheology of columnar-grained ice. Journal of Experimental Mechanics, Vol. 18, No. 12, pp. 464-470.

Sinha, N.K., (1979) Grain boundary sliding in polycrystalline materials, Phil. Mag. A, Vol. 40, pp. 825-842.

Sinha, N.K., (1983) Creep model of ice for monotonically increasing stress. Cold Regions Science and Technology, Vol. 8, pp. 25-33.

Smith, T.R., and Schulson, E.M., (1993) The brittle compressive failure of fresh-water columnar ice under biaxial loading, Acta Metall. Mater., Vol. 41, pp. 153-163.

Spencer, P.A., Masterson, D.M., Lucas, J., and Jordaan, I.J., (1992) The flow properties of crushed ice I: Experimental observations and apparatus. Proceedings 11th International IAHR Symposium on Ice, Banff, Vol. 1, pp. 158-168.

Stone, B.M., Jordaan, I.J., Jones, S.J. and McKenna, R.F., (1989) Damage of isotropic polycrystalline ice under moderate confining pressures. Proceedings of the 10th International Conference on Port and Ocean Engineering Under Arctic Conditions, Lulea, Sweden 1, pp. 408-419.

Stone, B.M., Jordaan, I.J., Xiao, J., and Jones, S.J., (1997) Experiments on the damage process in ice under compressive states of stress. Journal of Glaciology, Vol. 43, No. 143, pp. 11-25.

Xiao, J., and Jordaan, I.J., (1996) Application of damage mechanics to ice failure in compression. Cold Regions Science and Technology, Vol. 24, pp. 305-322.

Xiao, J., (1991) Finite element modeling of damage processes in ice-structure interaction. M. Eng. Thesis, Memorial University of Newfoundland, St. John's, NF.

Xiao, J., (in preparation) Ph.D. Thesis, Memorial University of Newfoundland, St. John's, NF.

Appendix A

Internal Research Report IRR-IM-9702

The Effects of Confinement on Temperature During Triaxial Testing of Granular Ice

By: Paul M. Melanson

June 15th, 1997

Project Team:
Melanson, P.M.
Meglis, I.L.

Introduction

In the winter of 1996 the experimental ice mechanics group began performing triaxial testing at high pressures above the usual 20 MPa confinement used for the last few years. At these higher pressures the temperature of the confining fluid in the cell increased, probably due to the work being applied to it by the pressure intensifier ram. The problem of increasing oil temperature became a concern for the group as temperatures in the confining cell approached the melting point of ice during testing. In order to understand

and recommend a solution to the problem a set of tests were performed on dummy samples of granular ice to track the temperature change within the ice samples subjected to high pressure.

Background

Triaxial tests by the ice group here at MUN ice typically tested at -10°C. Under simple hydrostatic pressure, the melting temperature of ice will increase approximately 0.7°C for each 10 MPa of confinement. This can lead to problems where pressures become very high. If an ice sample is subjected to high confinement reducing its melting point as well as being heated by the warmer oil, pressure melting may occur on the surface.

Ideally the ice should be tested at both a known and consistent temperature, without influences from the testing equipment. If pressure melting was actually occurring, on a local level due to stresses in the sample then it would be masked by any induced pressure melting.

A study of this phenomena to a pressure of about 20 MPa was performed by Barry Stone in 1991. He reported that there was not a significant increase in temperature within samples to warrant any concern at that point. A copy of his notes and part of a report are included as Appendices A-1 and A-2.

Procedure

In order to study this problem resistance temperature detectors (RTD's) were mounted inside granular ice samples and data recorded as a hydrostatic pressure was applied and held for 12 minutes. Three different rates were used to apply pressure to the sample, 0.1 MPa/s, 0.5 MPa/s (the standard used in most testing by the group), and 2.0 MPa/s.

As only one RTD could be used to collect data during each test, three sets of tests were performed. In the first set an RTD was mounted in the ice sample in the radial

centre of the cylindrical specimen. The second set of tests used an RTD located in the ice just below the surface of the latex jacket. A third set of tests was performed with a dummy specimen in the cell and an RTD left in the confining oil. A list of the tests performed as well as the corresponding data files is listed in Table A-1.

Table A-1 Test matrix

	Test Number	RTD location	Pressure rate (MPa/s)	Hold Time (min)
1	TT970605	side	0.5	12
2	T2970605	⇓	0.1	12
3	T3970605	⇓	2.0	12
4	TT970606	centre	0.5	12
5	T2970606	⇓	0.1	12
6	T3970606	⇓	2.0	12
7	TT970609	oil	0.5	12
8	TT970611	⇓	0.1	12
9	T2970611	⇓	2.0	12

Results

Results of testing show that the temperature of the oil changes significantly during tests to high pressure while the sample temperature generally only changes by a few degrees. Also the sample surface temperature (the critical temperature to be considered) changes by under 4°C in all the tests.

In each test the hold time once pressurisation was complete was 12 minutes (or 720 s). In all cases the oil began to cool as soon as the confining pressure of 60 MPa was reached and the hold step began. The temperature inside the sample increased during the hold step.

The table (Table A-2) below lists the some temperature differences during each test at the two locations in the sample and in the oil.

Plots of Change in Temperature vs. Time and Pressure are shown in Appendix A-3. These plots show that there is no correlation between pressurisation rate and core temperature after the 12 minute hold step. However, at the end of the pressurisation step the core temperature within the sample is significantly different for each pressure rate; 1.9, 1.1, and 1.3°C for 0.1, 0.5, and 2.0 MPa/s respectively.

Table A-2 Temperature change in each test

Location of RTD	Pressure-up rate (MPa/s)	ΔT at pressure up (°C)	ΔT at 6 min (°C)	ΔT at 12 min (°C)
Surface	0.5	2.9	3.6	3.8
⇓	0.1	3.0	3.3	3.4
⇓	2.0	2.2	3.3	3.6
Centre	0.5	1.1	2.5	3.0
⇓	0.1	1.9	2.9	3.2
⇓	2.0	1.3	2.5	3.2
Oil	0.5	6.8	6.0	4.5
⇓	0.1	6.4	4.5	3.3
⇓	2.0	7.1	7.1	5.4

Summary and Conclusions

The effect of confining pressure on the temperature of ice samples is relatively small. Temperature changes within the sample as a whole are typically 3.5°C or less. The temperature change at the surface of the sample is slightly larger, as was expected. The effect on the temperature inside the sample is not depended on the pressurisation rate above 0.5 MPa/s. Samples tested at various pressurisation rates all showed an increase in temperature in the sample core of about 3.2°C. after the 12 minute hold step. A difference in temperature was noted for sample at the end of the pressurisation step and is believed to be due to limitations in the heat transfer capacity of the ice to drop its temperature during very fast pressurisation.

Recommendations

The problem of significant temperature increase in ice samples on pressurisation may be solved in any of several ways.

- By decreasing the cold room temperature by 3°C or more (depending on the pressure), and therefore reducing the initial confining oil and sample temperatures, the temperature within the sample will still change on pressurisation but only by about -3°C for 60 MPa of pressure. This means the two changes cancel each other out leaving the sample at -10°C. The only drawback to this method is that the sample will tend to cool along with the confining oil, possibly overshooting the desired -10°C if the test being performed is very long in duration.
- Another solution that would require more work on the part of the operator, and would avoid the temperature overshoot mentioned in the previous solution, would be to cool the oil separately while still maintaining the cold room at -10°C. This would eliminate the danger of overshooting the temperature set point but may require some experimenting in order to obtain the right oil temperature. The test would need to be set-up and performed without delay as the sample would cool as soon as it is in contact with the oil.
- A more complex solution of manipulating both the cold room temperature and the oil temperature would satisfy the temperature requirements of both the surface and the core of the sample. However this would probably prove to be too much work for the operator. A simpler solution where the cold room temperature is adjusted so that the sample's surface would be slightly above the required temperature while the core would be slightly below the required temperature may be the optimal solution. In this case the temperature change for both parts of the sample would be minimised to within acceptable levels. This would require a minimum of work and preparation on the part of the operator, only requiring a change in the cold room setting the day prior to testing.

No matter which solution is preferred, it should be checked using a dummy specimen mounted with internal RTD's to monitor its core temperature.

Appendix A-1

Copy of Barry Stone's notes on the increase in temperature within ice samples at pressures up to 20 MPa, October, 1991.

Don

Re Temperature measurements under triaxial confining pressure

Sensor = RTD 100 pt calibrated against a reference thermocouple

① Sensor frozen into the center of an ice sample (60 mm x 60 mm x 120 mm)

Oct 2/91

Confining pressure: to 21.5 Mpa (6.9 V = 3115 psi) quickly

Temp: a corresponding increase in temp from -10.1°C to -9.7°C, a warming of 0.4°C at the ice center instantly upon pressure being applied. A further warming to -8.5°C over a time period of 15 min i.e. within 15 min of pressure being applied the center of the ice sample has warmed a total of 1.6°C, 0.4°C instantly from compression of the ice & 1.2°C from heat transfer from fluid

The cell, under pressure, was allowed [illegible] time (-10.1°C)

Sound Lower. Confining pressure was then released.

Center of ice cooled instantly to -10.4°C (a drop of 0.3°C) and over a period of 15 min. to -11.3°C for a total cooling of 1.2°C upon release of pressure. The reverse process of what happened upon applying pressure.

Oct 3/91

Confining pressure: to 22.2 Mpa (9.2V = 3220 psi.) applied over a period of 10 sec

Temp.: a corresponding increase in Temp from -10.1°C to -9.7°C, a warming of 0.4°C over the 10 sec period. Speed applying pressure. A further warming to -8.5°C over the next 15 min. Exactly duplicating the results of Oct. 2

The cell under pressure, was allowed to return to room temp. (-10.1°C) over a number of hours. Confining pressure was then released.

Center of ice cooled to -10.4°C over

to -11.3°C for a total cooling of 1.2°C upon release of pressure.

The tests of Oct 2 to 3 were exact duplicates in terms of procedure & results

(2) Sensor immersed in confining fluid

Oct 7

Confining pressure: to 21.7 MPa (9V = 3150 psi) applied over a period of 20 sec.

Temp.: a corresponding increase in temperature from -10.1°C to -6.7°C, a warming of the fluid of 3.4°C, over the 20 sec period of pressure application. The temperature did not increase further

The cell, under pressure, was allowed to return to room temp (-10.1°C) over a period of 2 hours.

Upon release of pressure temp dropped to -12.4°C over the first 4.5 sec. and did not fall further. A cooling of -2.3°C

Two additional tests, the same as the above Oct. 7 test, were conducted with one change. The confining pressure applied was released within 65 sec. to 55 sec of being applied.

START	PRESSURE APPLIED	PRESSURE RELEASED
-10.2°C	-6.9°C	-10.5°C
-10.2°C	-6.9°C	-10.3°C

We can discuss & review plots.

Barry

Appendix A-2

Copy of section of Ocean Engineering Research Centre draft report to the National Energy Board, regarding temperature effects in triaxial testing and ice load models.

DRAFT

FINAL REPORT

FURTHER DEVELOPMENT OF ICE LOAD MODELS

Submitted to

National Energy Board
Engineering Branch
Calgary, Alberta

by

Ocean Engineering Research Centre
Memorial University of Newfoundland
St. John's, Newfoundland

PROJECT TEAM

Barry Stone
Jing Xiao
Bin Zou
Ian Jordaan, Project Manager

March 22, 1994

it has been estimated that total strain for a 7 MPa pulse load at 10 MPa confinement would be 1.1% (ϵ). The pressure drop and resulting stress difference increase has resulted in a total strain of 7.3% (or $\Delta\epsilon$ = 6.2%).

2.4.4 Thermodynamic Aspects

The triaxial cell confining fluid temperature at the start of each test was -10° C ± 0.9° C. Pressurization of the cell resulted in a warming of the fluid by: 0.7° C for 5 MPa, 1.4° C for 10 MPa, and 2.6 ° C for 20 MPa. To establish the effect of pressurization on sample temperature fast response RTD elements were placed in the confining fluid, on the sample wall and in the sample center. As in all tests the specimen was sealed in a latex membrane with the center RTD element output being passed through a specially designed platen and high pressure electrical feed through. Output was recorded on a stripchart.

All three RDT elements showed an immediate increase in temperature upon pressurization to a confining pressure of 40 MPa. (Figure 2.17, Table 2.4). The 40 MPa pressurization at a rate of 4 MPa/sec. warmed the solid ice by 0.6° C and the liquid confining fluid by 5.7° C.

After peaks had been reached cooling from the -10° C cold room began immediately with sample center temperature reaching -9.0° C at 5400 sec. just prior to depressurization.

A second temperature test to a confining pressure of 20 MPa with a 4% total strain damage step showed similar results (Table 2.5). The RTD element at the sample centre failed at the completion of the damage step.

2.5 Discussion

As mentioned earlier, the elastic strain is not strongly influenced by the damage state, whereas the delayed elastic and secondary creep strain are significantly enhanced by several orders of magnitude, especially when the predamage is introduced under a triaxial stress state. The creep strain response of uniaxially predamaged ice is much smaller than that of triaxially predamaged ice.

Figure 2.18 shows two strain history curves for creep tests on predamaged samples. Sample I was tested under 10 MPa confinement with triaxial predamaging, i.e., the 10 MPa confining pressure was applied at the beginning of the test and kept constant throughout the test. The strain history from O to A is the predamage period. From A to B is the creep test period. Sample II was also tested under 10 MPa confinement, but with uniaxial predamaging, i.e., the initial predamaging was done under uniaxial condition. The 10 MPa confinement was applied after the predamaging, i.e., at point A. Due to the uniaxial predamaging, microcracks were developed along the direction of loading stress, therefore introducing anisotropy to the material properties. Upon the application of confinement, sample II was compressed close to the original

volume, which indicates most of the cracks were closed, or nearly closed, the creep response would also be smaller due to the closure of cracks. In fact, the ice with most of its cracks closed (due to confinement) can behave similarly to intact ice. The friction between the crack surfaces plays an important role in this type of ice. The effect of friction between closed crack surfaces may also explain why under 5 MPa confinement, the creep strain of predamaged ice was almost the same as the intact ice. When the confinement was increased to 10 or 20 MPa, due to possible pressure melting between grains or crack surfaces, the effect of friction is reduced and creep response of uniaxially predamaged ice is increased.

Sample I was tested after triaxial predamaging, thin sections of the sample after the test show less evidence of preferred crack orientation. Since the confinement was applied at the beginning of the test and kept constant thereafter, once the crack is opened, it will stay open so there is no frictional tractions cross the crack surfaces during deformation process, and the creep will be larger than that of uniaxially predamaged ice, as well as intact ice under same confinement.

As mentioned earlier, temperature at the center of ice sample was measured for two triaxial situations. During the 40 MPa pressurization in 10 sec., the ice was warmed by 0.8°C at the center, and 0.4 °C for the 20 MPa pressurization. Since the temperature was measured at the center of ice, and the sample was covered with a latex membrane, the pressurization period can be assumed as adiabatic process, and a thermodynamic formula can be derived to calculate the increase of temperature in the form of:

$$\Delta T = \frac{T}{C_p} K_T \Delta P$$

where T is ice temperature; C_p is specific heat; K_T is the thermal expansion and ΔP is the applied pressure. Calculated temperature increases are 0.86°C for 40 MPa and 0.43 °C for 20 MPa. The calculated temperature increases are higher than that of measured ones. This may be explained by possible pressure melting which will absorb heat during melting process.

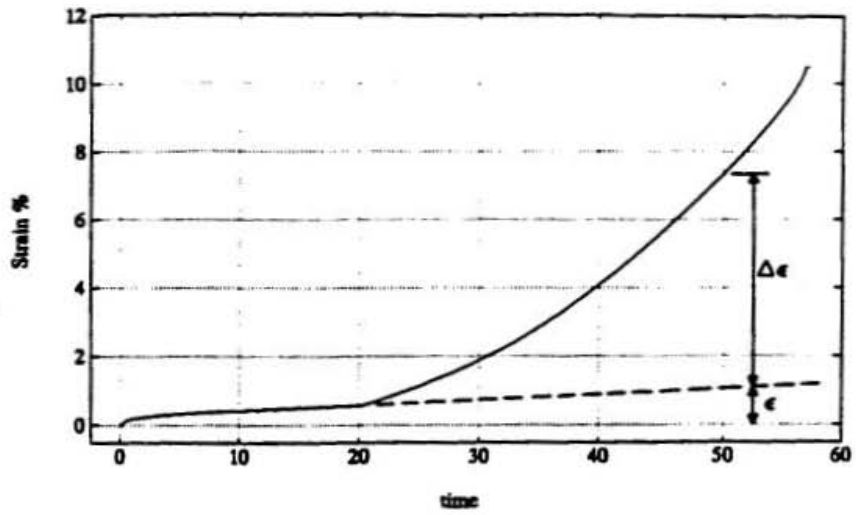

Figure 2.16 Strain-time, 2% triaxial predamage (2%10), 7 MPa load pulse, triaxial confining pressure 10 MPa 0 to 20 sec. 5 MPa 20 sec. to 100 sec.

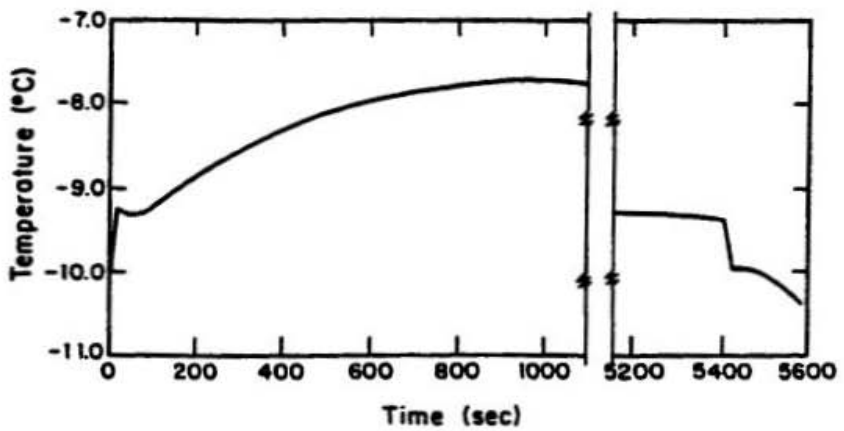

Figure 2.17 Temperature at sample centre upon pressurization to a triaxial confining pressure of 40 MPa.

Parameters Used in the Damage Model

Description	Parameter	Value
Elastic Modulus	E	9500 MPa
Elastic Stiffness in Kelvin Unit	E_k	3800 MPa
Poisson's Ratio	υ	0.3
Primary Creep Reference Rate	$\dot{\epsilon}_0^c$	$1.0 \times 10^{-5} s^{-1}$ 1 at -10°C
Creep Exponent for Kelvin unit	n	1.5
Secondary Creep Ref. Rate	$\dot{\epsilon}_0^c$	$1.76 \times 10^{-7} s^{-1}$ at -10°C
Creep Exponent for Maxwell unit	m	2.7
Damage Constant	f_1	30
Volumetric Constant	f_2	0.11
Reference Stress	σ_0	1 MPa
Damage Exponent	q	6
Creep Enhancement Parameter	β_a	2
Creep Enhancement Parameter	β_c	4

Appendix A-3

Plots of Change in Temperature versus Time and Pressure for all tests.

Plot #1 Change in Temperature vs. Time for 0.1 MPa/s

Plot #2 Change in Temperature vs. Pressure for 0.1 MPa/s

Plot #3 Change in Temperature vs. Time for 0.5 MPa/s

Plot #4 Change in Temperature vs. Pressure for 0.5 MPa/s

Plot #5 Change in Temperature vs. Time for 2.0 MPa/s

Plot #6 Change in Temperature vs. Pressure for 2.0 MPa/s

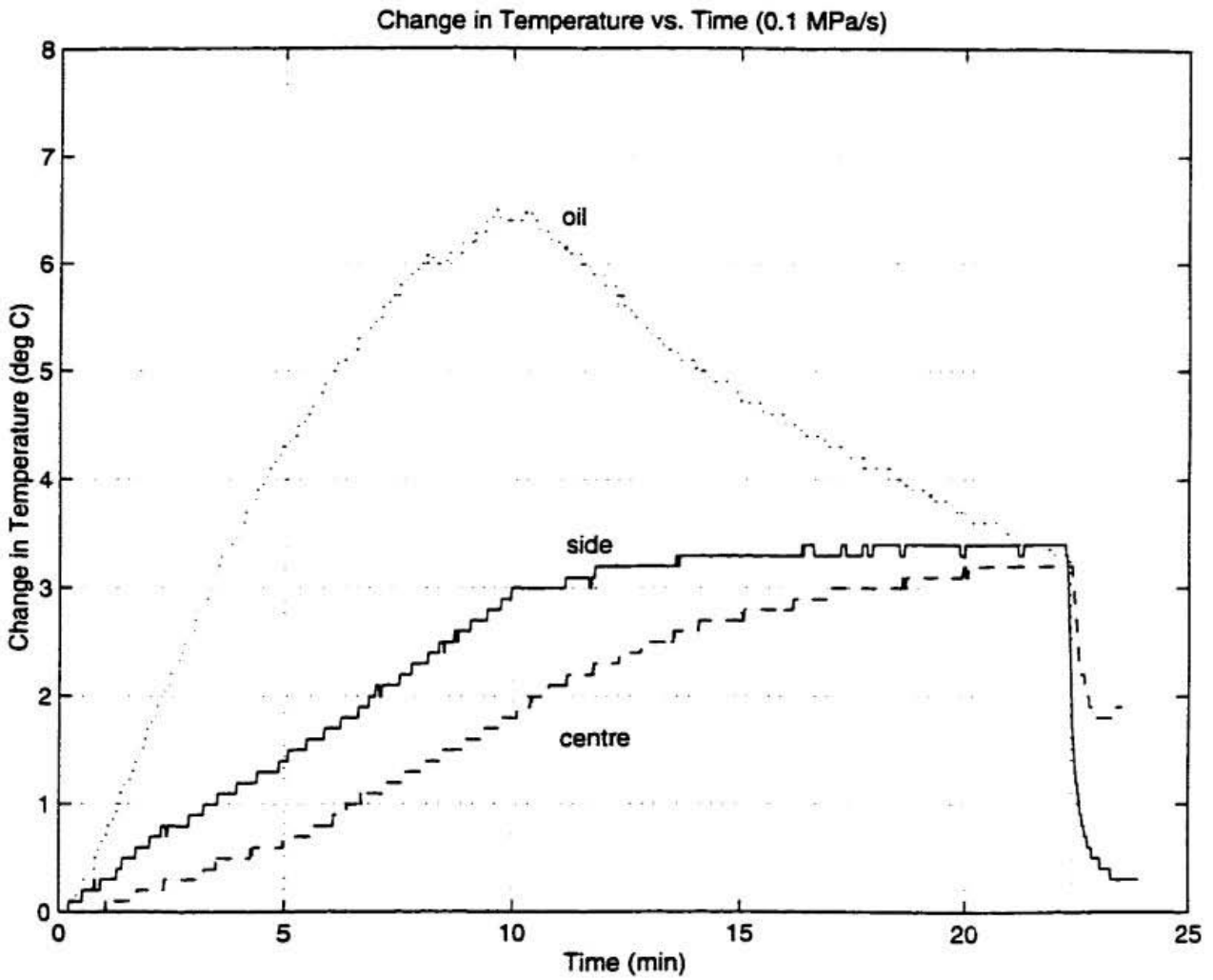
Change in Temperature vs. Time (0.1 MPa/s)
Change in Temperature (deg C)
Time (min)
oil
side
centre
0
1
2
3
4
5
6
7
8
0
5
10
15
20
25

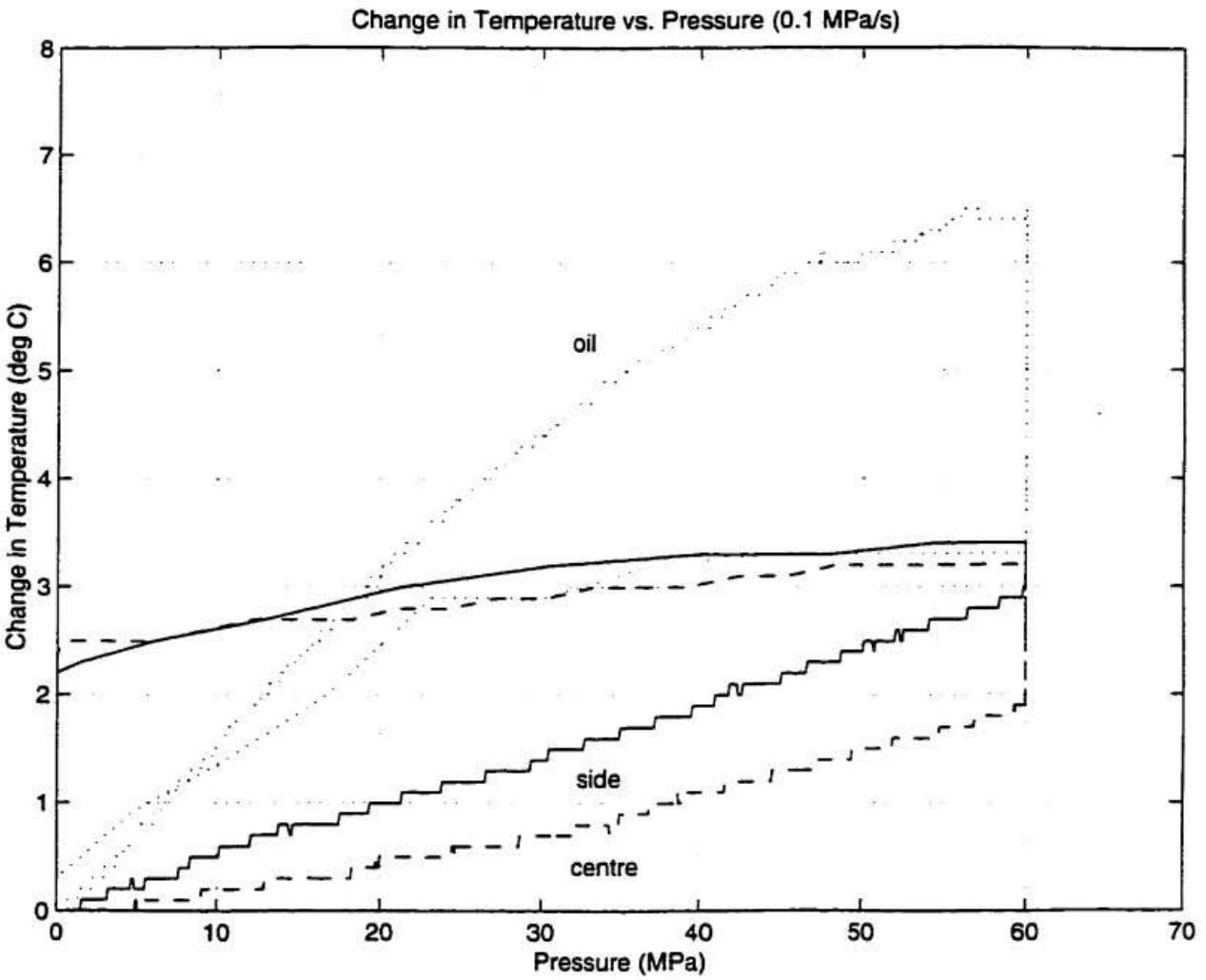
Change in Temperature vs. Pressure (0.1 MPa/s)
Change in Temperature (deg C)
Pressure (MPa)
oil
side
centre
0
1
2
3
4
5
6
7
8
0
10
20
30
40
50
60
70

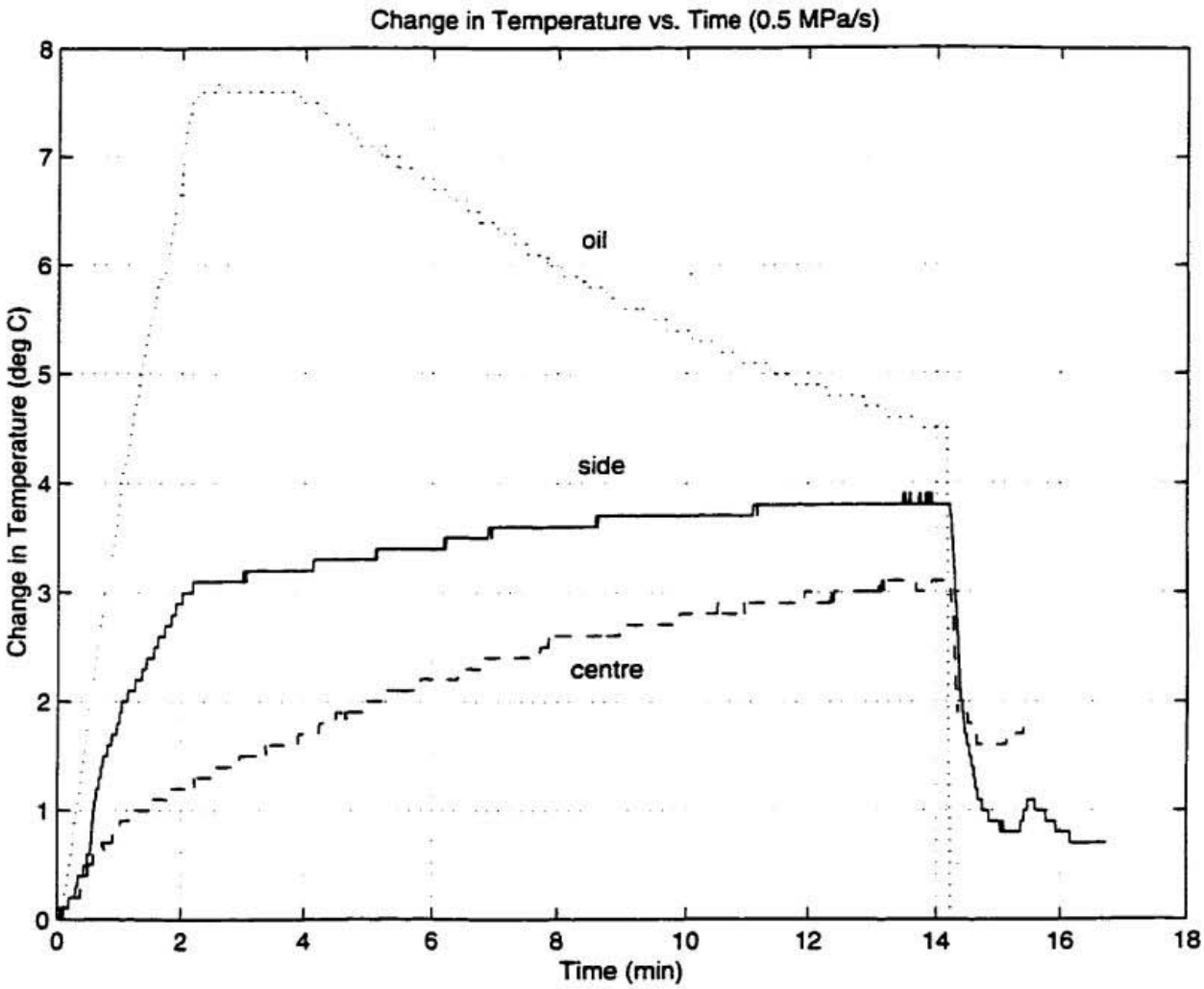
Change in Temperature vs. Time (0.5 MPa/s)
Change in Temperature (deg C)
Time (min)
oil
side
centre
0
1
2
3
4
5
6
7
8
0
2
4
6
8
10
12
14
16
18

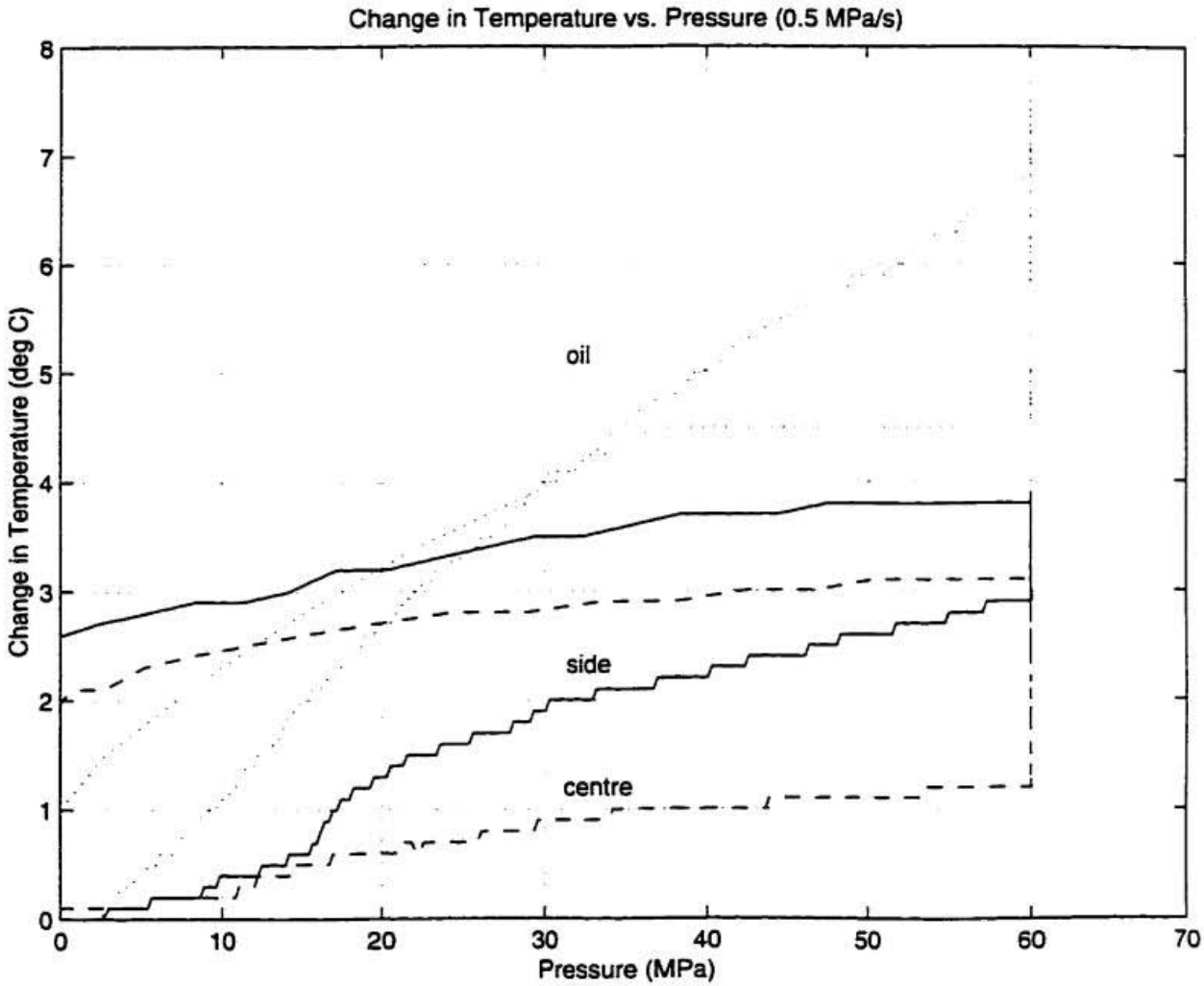
Change in Temperature vs. Pressure (0.5 MPa/s)
Change in Temperature (deg C)
Pressure (MPa)
oil
side
centre
0
1
2
3
4
5
6
7
8
0
10
20
30
40
50
60
70

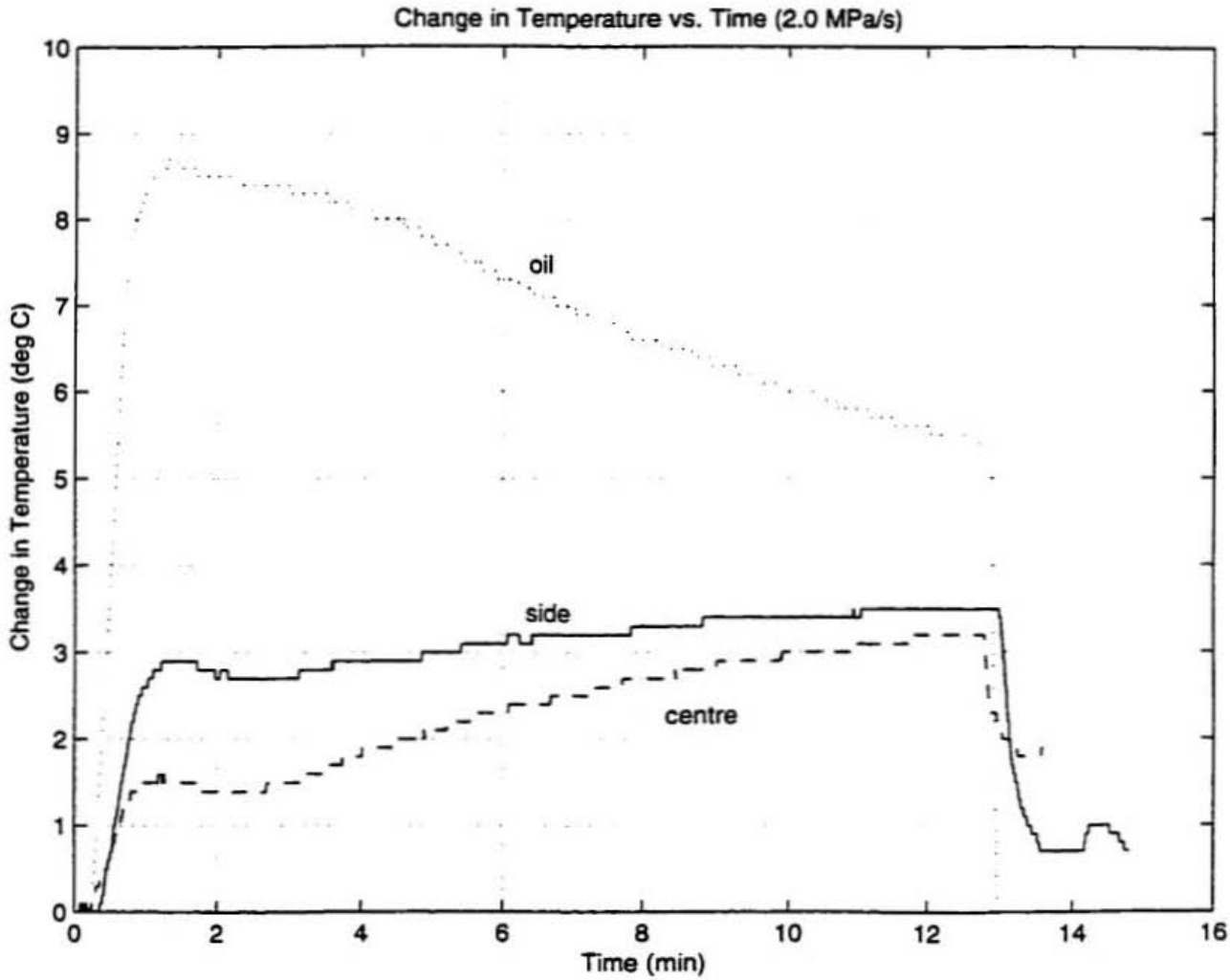
Change in Temperature vs. Time (2.0 MPa/s)
Change in Temperature (deg C)
Time (min)
oil
side
centre
0
1
2
3
4
5
6
7
8
9
10
0
2
4
6
8
10
12
14
16

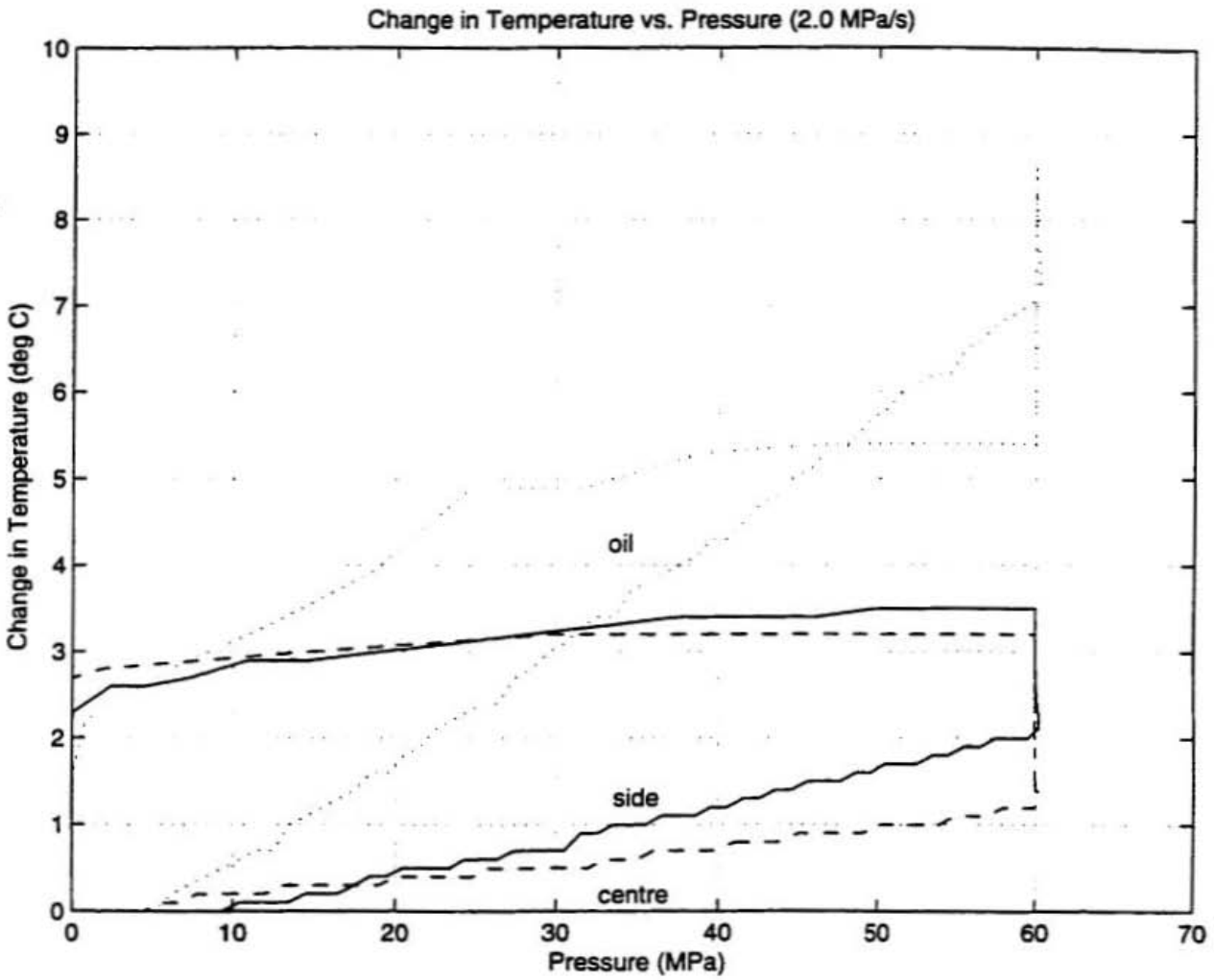
Change in Temperature vs. Pressure (2.0 MPa/s)
Change in Temperature (deg C)
Pressure (MPa)
oil
side
centre
0
1
2
3
4
5
6
7
8
9
10
0
10
20
30
40
50
60
70

Attachment to Report No. IRR-IM-9702

By: Paul M. Melanson

June 17th, 1997

After consideration and discussion of the internal report referenced above with Irene Meglis, the last recommendation was accepted and trial of the method outlined set up in the lab. The recommendation outlined simply reducing the initial temperature of the entire set up to compensate for the increase in temperature from the oil, accepting that obtaining the an acceptable temperature over the entire specimen is not worth the effort required. The result of the trial indicates that the temperature problem can easily be overcome with some planning prior to testing at high pressures.

A granular ice sample was set up with an RTD mounted on the surface. It was left in the cold room to equilibrate to the cold room temperature of -12.5°C, 2.5°C below the expect test temperature. The results of the temperature record after the test (TT970616, pressurising at 0.5 MPa/s and holding for 360 s) show that the temperature behaves essentially as was projected, increasing the surface temperature of the sample to about -10°C. The plots attached show Change in temperature versus Time and Pressure.

The temperature inside the sample was not monitored in these tests. Results from previous tests outlined in the report suggest that the internal temperature will change only slightly, resulting in an expected temperature change to about -11.3°C from -12.5°C.

This seems to have eliminated the temperature problem for pressures up to at least 60 MPa. Other temperature effects at lower pressures should be able to be eliminated by the same method.

Appendix B

Observations on the variation of the elastic response of ice subjected to triaxial stress conditions.

During the course of this study the work of other researchers has been used for comparison. Parameters such as the magnitude of the elastic and delayed elastic contribution and effective viscosity were compared. One point that became increasingly obvious during these comparisons as the testing progressed is what appears to be an increase in the elastic component of the deformation in granular ice subjected to confinement when compared to uniaxial tests.

Initially Sinha's relation (1983) was used for comparison. The model from Sinha is typically only valid for small stresses and uniaxial stress conditions but served as a benchmark for comparing initial strain rate values from the test data. It was observed specifically is that tests at high confinement seemed to have an increase in elastic strain two to three times greater than that predicted by Sinha's elastic modulus.

This is apparent in the plots shown in Figure B.1. The elastic component of Sinha's relation is shown separately along with the delayed elastic component. The viscous

component is not shown but is added to the previous two to yield the total response. The y-axis is normalised by dividing by the stress in each case essentially giving an indication of the elastic modulus in each case. The result is indicative of many of the tests performed during this study. The elastic component of the low pressure test is about twice that of Sinha's predicted value while the other two test are three times as large.

There has been some question as to the contribution of the delayed elastic component of the deformation in these tests. It may be that the delayed elastic component is faster in these tests and results in what appears to be a larger elastic component. The normalising of the strain with stress does tend to isolate this and still shows that the elastic is larger.

Other factors that may be at work within the ice include microstructural changes such as crack suppression and grain boundary effects, however these would seem to increase the elastic modulus of the ice and not reduce it, as is observed in the graphs. No further analysis was performed but the observation of this phenomena was thought to be noteworthy and is presented here as such.

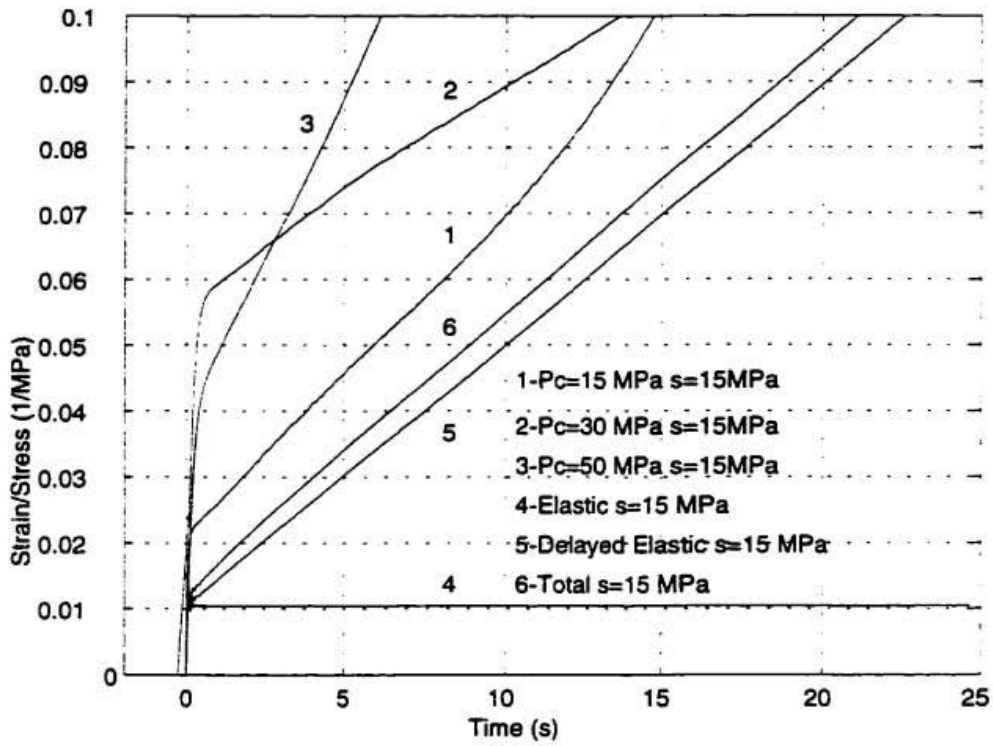

Figure B.1 Plots of strain versus time for curves based on Sinha's relation (1983) and constant stress test data for s = 15 MPa and p_c = 15, 30 and 50 MPa.

Appendix C

Details of the use of the constitutive model for polycrystalline ice developed by Xiao (1991) and Xiao and Jordaan (1996).

The use of the constitutive model outlined in Xiao and Jordaan (1996) is explained briefly below and includes the MATLAB m-files used in this study. The purpose of using the model was for both the formulation of Table 5.1 and for comparison with the pressure-dependent constitutive model calibrated in the report. An outline of the model is presented along with equations followed by an example run. For a more detailed look at the model the reader is referred to Xiao and Jordaan (1996) and Xiao (1991).

The constitutive model is based on damage mechanics similar to the theory outlined in above in the text. Only the axial components of stress were used in the analysis, volumetric strain was neglected.

The model was based on two separate damage parameters S_c (creep) and S_d (delayed elastic) for the Maxwell and Kelvin components of the Burgers unit, as shown in Figure 2.6. The damage parameters were developed based on Shapery's damage measure (Schapery, 1981):

$$S_c = \int_0^t F_m(p)\left(\frac{\sigma}{\sigma_0}\right)^{q_m} d\tau \tag{C.1}$$

$$S_d = \int_0^t F_k(p)\left(\frac{\sigma}{\sigma_0}\right)^{q_k} d\tau \tag{C.2}$$

where the functions $F_k(p)$ and $F_m(p)$ are pressure dependent and address the grain size within the ice. The stress σ is the axial stress and σ_0 is a reference stress, and q_m and q_k, the damage function exponents, are constants. The pressure dependent functions are:

$$F_m(p) = \frac{f_m}{p}\left(\frac{d}{2}\right)^3 \tag{C.3}$$

$$F_k(p) = \frac{f_k}{p}\left(\frac{d}{2}\right)^3 \tag{C.4}$$

where p is the hydrostatic pressure, d is the grain size in meters, and f_k and f_m are constants.

The strain rate of the creep and delayed elastic components are expressed as:

$$\dot{e}^c = \left(\frac{3}{2}\right)\dot{\varepsilon}_0^c\left(\frac{s}{\sigma_0}\right)^m \tag{C.5}$$

$$\dot{e}^d = \left(\frac{3}{2}\right)\dot{\varepsilon}_0^d\left(\frac{s - E_k e^d}{\sigma_0}\right)^n \tag{C.6}$$

where E_k is the elasticity of the Kelvin spring, m and n are constants, and $\dot{\varepsilon}_0^c$ and $\dot{\varepsilon}_0^d$ are reference strain rates.

The enhancement of the creep terms due to damage is expressed as an exponent where a creep enhancement factor β is introduced for each component, and the S terms are the damage values from above (Equations C.1 and C.2):

$$e'^c = \dot{e}^c \exp(\beta_c S_c) \tag{C.7}$$

$$e'^d = \dot{e}^d \exp(\beta_d S_d) \tag{C.8}$$

The elastic component of the deformation is taken simply as:

$$e^e = \frac{\sigma}{E} \tag{C.9}$$

where E is the elastic modulus of the ice. The whole is then added to form the total response of the ice as:

$$\dot{e} = \dot{e}^e + \dot{e}'^c + \dot{e}'^d \tag{C.10}$$

Now the whole can be integrated to determine the total strain.

In applying these equations to a MATLAB m-file a time stepping approach was used. The model was run in three parts. Initially a file containing the input variables was run to set the initial conditions and parameters for the model. The model was then run with a second m-file. A post analysis executable m-file plotted and stored results. The output is several MATLAB figures which show the stress, strain, strain rate, and damage of each component plotted against time. These are easily modified to plot the different combinations of variables over specific ranges.

The input file, *input.m*, is shown below and the variables outlined.

```
%  input.m
%  sinp = s dt tmax p_c
sinp=[15, 0.025, 100, 50];
%
%  p1 = fm fk Soc Sod d
p1=[30, 5000, 0, 0, 0.00238];
%
%  p2 = eocrate eodrate so
p2=[1.76e-7, 1.0e-5, 1];
%
%  p3 = qk qm n m
p3=[3, 6, 1.5, 2.7];
%
%  p4 = Ek E Bd Bc
p4=[3800, 9500, 2, 4];
```

The following table represents the initial parameters and their values.

Table A.1 Parameters used in the damage model of Xiao and Jordaan (1996).

Parameter	Description	Value	Unit
s	axial stress	variable	MPa
dt	time increment	variable	s
tmax	maximum time	variable	s
p_c	confining pressure	variable	MPa
fm	Maxwell unit damage constant	30	
fk	Kelvin unit damage constant	5000	
Soc	initial damage value Maxwell unit	0	
Sod	initial damage value Kelvin unit	0	
d	grain size	0.0238	m
eocrate	Maxwell unit creep reference rate	1.76×10^{-7}	s^{-1}
eodrate	Kelvin unit creep reference rate	1.0×10^{-7}	s^{-1}
so	reference stress	1.0	MPa
qk	Kelvin unit damage exponent	3	
qm	Maxwell unit damage exponent	6	
m	Maxwell unit creep exponent	2.7	
n	Kelvin unit creep exponent	1.5	
Ek	elastic stiffness of Kelvin unit	3800	MPa
E	elastic modulus	9500	MPa
Bc	Maxwell unit creep enhancement parameter	4	
Bd	Kelvin unit creep enhancement parameter	2	

The m-file which performed the time stepping routine, *consts.m*, is shown below.

```
%  consts.m
%  Jing Xiao's model, Dec. 1997 by: Paul Melanson
%
%%%
```

```
        dSc=0;
%
        R(1,1)=t;
        R(1,2)=e;
        R(1,3)=ee;
        R(1,4)=ed;
        R(1,5)=ec;
        R(1,6)=s;
        R(1,7)=d;
        R(1,8)=0;
        R(1,9)=0;
%
%%%
```

A plot of the result of running the model at s = 5, 10, and 15 MPa and p_c = 15 MPa is shown below over the range 0 < t < 30 s with a time increment of 0.05 s.

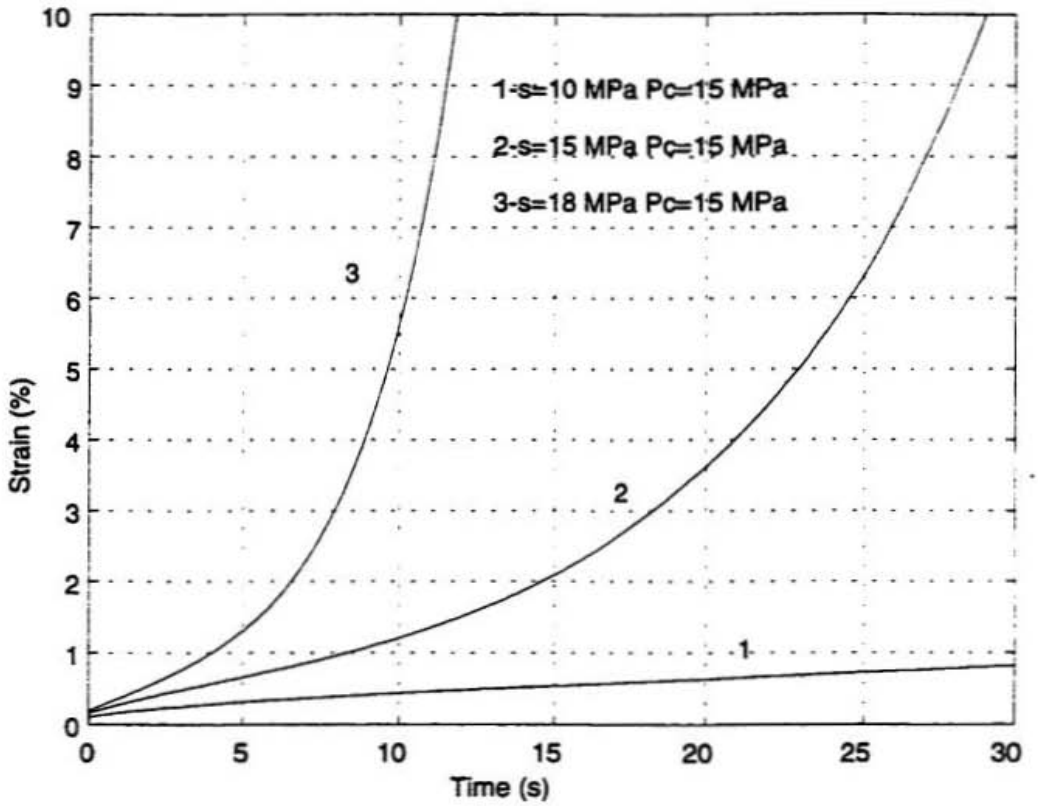

Figure C.1 Result of sample run of damage model from Xiao and Jordaan (1996) for s = 5, 10, and 15 MPa and p_c = 15 MPa.